

## Analysis of boundary layer flow over a broad rotating cone in still fluid with non-stationary modes

Matthew Fildes,<sup>1, a)</sup> Zahir Hussain,<sup>b)</sup> Jay Unadkat,<sup>c)</sup> and Stephen Garrett<sup>d)</sup>

*School of Engineering, University of Leicester, Leicester, LE1 7RH,*

*UK*

(Dated: 27 November 2020)

This study focuses on analyzing the effects of traveling modes on the boundary layer flow over a rotating cone in still fluid system. Non-stationary modes are known to manifest in the boundary layer of rotating cones with highly polished very smooth surfaces. For this paper, only the broad rotating cone (defined as a cone with the half angle  $\psi \geq 40^\circ$ ) system is considered. An asymptotic analytical method is used to solve the governing equations and output the wave angle and wave number of the system. This is then compared to a numerical formulation which uses a Chebyshev spectral method. The resulting solutions show that increasing the wave frequency destabilizes the system, with a much stronger destabilization for the viscous wall type II modes than the inviscid cross-flow type I mode, where the type I mode is the dominant mode seen in experiments. This result suggests that a slower frequency wave should be selected in order to maximize the stability of the system. It also was observed that the negative frequency values have a minima of the critical Reynolds number values for each cone half angle. It also shows that there is a comparison limit for high frequency positive values. After this an energy balance analysis is conducted to see the effect on the total mechanical energy transferred between the basic flow and the perturbation quantities. This showed that as the frequency of the traveling modes increases, the energy transferred decreases.

**Keywords:** Boundary layer flow, Spectral methods, Fluid systems, Asymptotic analysis, Mechanical energy, Energy analysis

---

<sup>a)</sup>mf317@leicester.ac.uk

<sup>b)</sup>zahir.hussain@leicester.ac.uk

<sup>c)</sup>jay.unadkat@leicester.ac.uk

<sup>d)</sup>stephen.garrett@leicester.ac.uk

## I. INTRODUCTION

There has recently been great interest in the mechanics governing the flow around a rotating cone. The broad rotating cone considered in this paper can be used to model the behavior of air flowing over the central nose cone of an aero-engine fan. The large half angles used in these nose cones are chosen to deflect the ensuing turbulent flow from entering the turbofan core, whilst also ensuring that sufficient amount of airflow is flowing into the fan blades. It is important due to environmental and noise concerns to understand the system that governs the intake of this airflow, with the aim to improve the efficiency of the system. This paper extends the work done by<sup>1-3</sup> to study the effect of considering non-stationary modes on the broad rotating cone model, using both an asymptotic and numerical method. Physically, non-stationary modes will appear in the system for a highly polished smooth cone (where the roughness in both the radial and azimuthal direction being close if not equal to 0), as surface roughness tends to select stationary modes. In the literature covering the eigenmodes on the rotating disk/cone model, there are three distinct families of eigenmodes. The first of which are the type I modes. These modes are the upper branch inviscid modes, where the boundary layer becomes unstable away from the wall of the disk/cone. Second is the type II modes. These are short-wavelength viscous wall modes, these modes have instability which stems from the effects of being near the wall of the disk/cone. Finally, there is the type III eigenmodes, which have been observed by Mack<sup>4</sup>, Lingwood<sup>5</sup> and Federov<sup>6</sup>. These modes have only been observed in experimental studies which covered the rotating disk geometry. They occurred in these experimental studies at the turbulent region of the disk, in the form of several fine tracks on the surface on the disk, and are known to coalesce with the type I modes to form an absolute instability.

For traveling mode analysis of the rotating disk, the first main resource was a report by Turkyilmazoglu<sup>7</sup>. This report investigated the linear absolute/convective instability of the flow due to a rotating disk and expanded the work done by both<sup>8,9</sup>, covering the numerical and asymptotic study of the boundary layer on a rotating disk with stationary modes respectively. It also expanded the work done on in the study by Balakumar and Malik<sup>10</sup> who studied traveling disturbances on the rotating disk flow. Balakumar and Malik covered the derivation of the traveling mode perturbation equations and solved them numerically using a spectral method and covers an asymptotic investigation where the wavenumber quantities are able to be solved separately. Then they solved the values of the Reynolds numbers and eigenvalues for the scaled traveling mode frequencies

$\omega = -5, 4, 7.9, 10$ , which are the values used in further traveling mode literature for comparative purposes. This was expanded by Turkyilmazoglu<sup>11</sup> who used a non-linear method to solve for the type II modes on a rotating disk. This paper showed a second branch being present for positive frequency values, which the author described as the representation of the type III eddies found in the experimental study done by Federov<sup>6</sup>. This paper gives a good analysis of the non-linear type II modes, but doesn't cover the asymptotic derivation of the type I modes. The work done in this paper was expanded by Hussain, Garrett and Stephen<sup>3</sup> who covered both type I and type II modes using the scaling method similar to the method presented in Hussain's thesis<sup>12</sup>. They found that the traveling modes had a larger effect on the type II modes and had very little effect on the type I modes for the rotating disk. This paper also compared the asymptotic results to numerical analysis by using the same selection of frequency terms Turkyilmazoglu<sup>7</sup>. These terms are used due to the great care required to compare the numerical and asymptotic results due to the different scalings used for each case, as well as the fact that type II modes only have a solution up until the frequency value of  $\omega = 4$  for the asymptotic method. One of the main experimental studies on the rotating cone was done by Kobayashi and Izumi<sup>13</sup>. This experiment used cones with half angles  $15^\circ, 30^\circ, 45^\circ, 60^\circ$  and  $75^\circ$  and used a hot wire anemometer technique to measure the waves formed on the boundary layer. The main results that they found was that the cones with half angles  $15^\circ, 30^\circ$  formed counter-rotating vortices meanwhile for the other half angles above  $30^\circ$  unidirectional waves were formed instead. As well as this experimental study, more recently, experiments has been performed using a hot wire anemometer for a rotating cone with additional roughness elements added to the surface in the paper<sup>14</sup>. As well as this, experiments have been performed on the rotating cone by the Delft university of technology in the papers<sup>15,16</sup>. In these experiments they used a non-invasive infra-red thermography technique to capture the boundary layer disturbances on a rotating cone. In these studies, it was found that traveling waves which moved slower than the surface of the cone were detected. The theory of the boundary layer of the rotating cone was then expanded by Garrett and Peake<sup>17</sup> who studied the absolute stability of the rotating cone, and found the values of the critical Reynolds numbers for absolute instability, using a local stability analysis. This absolute instability analysis was recently updated by Thomas and Davis<sup>18</sup> who used a global stability analysis to calculate the absolute instability of the rotating cone, and found that the global method produced results which compared well with the local absolute stability analysis. They found that for large azimuthal wave numbers, a faster than exponential growth occurred which had a greater azimuthal wavenumber requirement than the critical Reynolds number for absolute

instability. Using the results from Garrett and Peake<sup>17</sup>, the study by the Garrett group<sup>2</sup> uses both numerical and asymptotic analysis to predict the waveangle and wavenumber of the instability waves formed on the boundary layer of a broad cone. The asymptotic method followed a similar method to the method presented by Hall<sup>9</sup> except with the inclusion of scaling with the cones half angle. They found that increasing the half angle of the cone stabilized the flow for the inviscid type I and viscous-Coriolis force balance type II modes. Whilst finding that for slender cones (i.e cones with less than  $40^\circ$ ) that a centrifugal instability was dominant. The thesis by Hussain<sup>12</sup> also covers an asymptotic analysis of the rotating cone in still fluid, as well as covering the case with added external oncoming (axial) flow and deriving the expressions for the centrifugal instability modes for slender cones. Garrett also published a paper which analyzed the growth rates of the type I and type II modes in the rotating cone boundary layer<sup>19</sup>. This paper covered both stationary and traveling mode growth rates and showed that the stationary type I mode becomes less amplified with decreasing half angle. It also found that for traveling mode growth rates, the change in frequency had a more significant effect for type II modes compared to type I modes (similar to the results found for the rotating disk). It also found that the type I modes traveling at 75% the speed of the cone were the most desired for vortex speed selection. For studies which covered an energy balance analysis, the first was the work done by Cooper and Carpenter<sup>20</sup>. Who conducted an energy balance analysis on the rotating disk for both stationary and traveling modes. They used the maximum growth rate at the position  $R = 600$  (where  $R$  represents the Reynolds number) and found that only the energy production due to Reynolds stresses and energy dissipation due to viscosity had meaningful effects on the total mechanical energy for the rotating disk. Cooper et al<sup>21</sup> expanded the energy balance analysis to cover a rotating disk with the effects of anisotropic and isotropic roughness taken into consideration. This was then recently expanded further by Miller et al<sup>22</sup>, who extended this energy analysis for the rotating disk to include the effects of temperature dependent viscosity. In this paper Miller et al used the position of  $R = R_c + 200$ , where  $R_c$  is the critical Reynolds number for the rotating disk, and found the same observation for the temperature independent case, with the effects of temperature dependent viscosity included in the formulation of energy dissipation due to viscosity.

The discovery by Tambe et al<sup>15,16</sup> that detected traveling mode waves forming on the surface of the rotating cone has motivated this study to provide an expansion to existing formulations for the broad cone to include the effect of traveling modes frequencies. To achieve this, we use both asymptotic and numerical methods. This is to cover the effects of traveling modes at high

Reynolds numbers using the asymptotic method, and low Reynolds numbers (including the effect of the frequency on the critical Reynolds numbers for various broad cone half angles) using the numerical methods. As although traveling modes for the rotating cone have been covered briefly before, there has been a gap in how these modes effect the critical Reynolds numbers as the half angle changes, as well as detail on the changes to the formulation when including the traveling mode frequency. This is of great interest to engineering and experimental study design, as well as others who wish to expand the basic still fluid model to include the effects of other physical parameters such as axial flow or surface roughness. Also the recent interest for the energy balance analysis work done by<sup>20–22</sup> indicated an opportunity to study the effects of the change in half angle, and separately the change in frequency, on the energy budget for a rotating cone. As previous studies have only been conducted for the rotating disk case (i.e the special case where the cone half angle is  $90^\circ$ ).

This paper first introduces the formulation of the problem in Section II. Then we introduce the asymptotic linear analysis in Section III, leading to the integral expansions for both the type I (Section III A) and type II (Section III B) modes before moving on to the traveling modes analysis in Section IV (again for both the type I (Section IV A) and type II (Section IV B) modes). After this, the numerical formulation for the Chebyshev spectral method is shown in Section V A. Then the results of this numerical analysis are shown in Section V. The asymptotic and numerical results are then compared in Section VI. After this a critical Reynolds number study is then conducted in Section VII. After which, an energy balance analysis is conducted for the numerical regime in Section VIII. Finally the conclusions of the study are shown in Section IX.

## II. PROBLEM FORMULATION

Consider a smooth rigid cone (with roughness in both the radial and azimuthal direction being 0), which is rotating about in the  $z^*$  axis which is its axis of symmetry, where an asterisk indicates a dimensional quantity. The radial and azimuthal coordinates which rotate with the cone are given by  $x^*$  and  $\theta$  respectively. We use  $l^*$  as the dimensional length scale along the cone.  $\Omega^*$  represents the angular velocity of the cone.  $\psi$  represents the cones half angle, which is the angle between the cones slanting surface and the cones symmetry. Finally  $\nu^*$  represents the kinematic viscosity. This cone is then placed in an incompressible still fluid (with no axial flow). This causes the dimensional surface velocity distribution along the boundary layer of the cone to be

given by  $U_0^*(x^*) = 0$ . A diagram of this formulation can be seen in Figure 1. If we transform

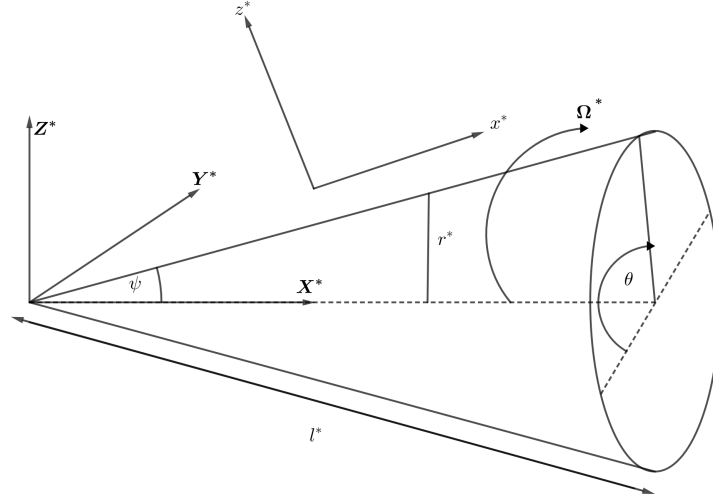


FIG. 1. Figure showing the geometry for the broad rotating cone problem. Where  $(X^*, Y^*, Z^*)$  are the Cartesian coordinates. The transformed curvilinear coordinates are  $(x^*, \theta, z^*)$ . The angular velocity is represented by  $\Omega^*$ . The length of the cone is given by  $l^*$ . The cone half angle is given by  $\psi$ . Finally the radius of the cone  $r^*$  is given by  $r^* = x^* \sin \psi$ . Used with permission from Z. Hussain, Ph.D. thesis, University of Birmingham (2010).

the Navier-Stokes equations to a curvilinear coordinate system, we then get the following well-known governing Navier-Stokes equations for the broad rotating cone (an interested reader is recommended to see<sup>12</sup> for a more detailed derivation of this transformation):

$$\frac{\partial u^*}{\partial x^*} + \frac{u^* \sin \psi}{h^*} + \frac{1}{h^*} \frac{\partial v^*}{\partial \theta} + \frac{\partial w^*}{\partial z^*} + \frac{w^* \cos \psi}{h^*} = 0, \quad (1)$$

$$\begin{aligned} \frac{\partial u^*}{\partial t^*} + u^* \frac{\partial u^*}{\partial x^*} + \frac{v^*}{h^*} \frac{\partial u^*}{\partial \theta} + w^* \frac{\partial u^*}{\partial z^*} - \frac{v^{*2} \sin \psi}{h^*} - 2\Omega^* v^* \sin \psi - \Omega^{*2} h^* \sin \psi \\ = -\frac{1}{\rho^*} \frac{\partial p^*}{\partial x^*} + \nu^* \left( \nabla^{*2} u^* - \frac{(u^* \sin \psi + w^* \cos \psi) \sin \psi}{h^{*2}} - \frac{2 \sin \psi}{h^{*2}} \frac{\partial v^*}{\partial \theta} \right), \end{aligned} \quad (2)$$

$$\frac{\partial v^*}{\partial t^*} + u^* \frac{\partial v^*}{\partial x^*} + \frac{v^*}{h^*} \frac{\partial v^*}{\partial \theta} + w^* \frac{\partial v^*}{\partial z^*} + \frac{(u^* \sin \psi + w^* \cos \psi) v^*}{h^*} + 2\Omega^* (u^* \sin \psi + w^* \cos \psi)$$

$$= -\frac{1}{\rho^* h^*} \frac{\partial p^*}{\partial \theta} + \mathbf{v}^* \left( \nabla^{*2} \mathbf{v}^* + \frac{2 \sin \psi}{h^{*2}} \frac{\partial u^*}{\partial \theta} + \frac{2 \cos \psi}{h^{*2}} \frac{\partial w^*}{\partial \theta} - \frac{v^*}{h^{*2}} \right), \quad (3)$$

$$\begin{aligned} & \frac{\partial w^*}{\partial t^*} + u^* \frac{\partial w^*}{\partial x^*} + \frac{v^*}{h^*} \frac{\partial w^*}{\partial \theta} + w^* \frac{\partial w^*}{\partial z^*} - \frac{v^{*2} \cos \psi}{h^*} - 2\Omega^* v^* \cos \psi - \Omega^{*2} h^* \cos \psi \\ & = -\frac{1}{\rho^*} \frac{\partial p^*}{\partial x^*} + \mathbf{v}^* \left( \nabla^{*2} w^* - \frac{(u^* \sin \psi + w^* \cos \psi) \cos \psi}{h^{*2}} - \frac{2 \cos \psi}{h^{*2}} \frac{\partial v^*}{\partial \theta} \right). \end{aligned} \quad (4)$$

Where the dimensional Laplacian operator for the curvilinear coordinate system  $(x^*, \theta, z^*)$  present in the Navier-Stokes equations is given by:

$$\nabla^{*2} = \frac{\partial^2}{\partial x^{*2}} + \frac{1}{h^{*2}} \frac{\partial^2}{\partial \theta^2} + \frac{\partial^2}{\partial z^{*2}} + \frac{\sin \psi}{h^*} \frac{\partial}{\partial x^*} + \frac{\cos \psi}{h^*} \frac{\partial}{\partial z^*}. \quad (5)$$

The appropriate boundary conditions for this system are:

$$u^* = 0, \quad v^* = 0, \quad w^* = 0, \quad \text{on } z^* = 0, \quad (6)$$

$$u^* \rightarrow U_0^*(x^*) = 0, \quad v^* \rightarrow -x^* \Omega^* \sin \psi, \quad \text{as } z^* \rightarrow \infty. \quad (7)$$

We begin the asymptotic study by the non-dimensionalisation of Equations (1-4) in a similar way to Hussain<sup>12</sup>. This leads to the expression for the Reynolds number as:

$$R = \frac{\Omega^* l^{*2} \sin \psi}{\nu^*}, \quad (8)$$

The distances in the  $z^*$  direction are scaled on the boundary layer thickness  $\delta^* = (\nu^*/\Omega^*)^{1/2}$ , which leads to the non dimensional rescaled wall normal coordinate  $\eta = z^*/\delta^*$ . The boundary layer thickness is given by  $R^{1/2}$ . The velocity scales for the basic steady flow are given by:

$$\mathbf{u} = \mathbf{u}_b = \Omega^* l^* \sin \psi \left( xU(\eta), xV(\eta), R^{-1/2}W(\eta) \right), \quad (9)$$

which is in the radial, azimuthal and normal directions respectively. These scales are determined by the non dimensional Navier-Stokes (N-S) equations and are reduced to the Von Kármán equations:

$$2U + W' = 0, \quad (10)$$

$$U^2 + WU' - (V + 1)^2 = U'', \quad (11)$$

$$WV' + 2U(V + 1) = V'', \quad (12)$$

$$(V + 1)^2 \cot \psi = P'. \quad (13)$$

With the boundary conditions given as

$$\begin{aligned} U = 0, \quad V = 0, \quad W = 0, \quad \text{on } \eta = 0, \\ U \rightarrow 0, \quad V \rightarrow -1, \quad \text{as } \eta \rightarrow \infty. \end{aligned} \quad (14)$$

Where the prime denotes differentiation with respect to  $\eta$ . Equations (10-13) are solved using a fourth order Runge-Kutta integration method. The result of which are the well known results for the velocity profile of a broad rotating cone in still fluid as shown in Figure 2.

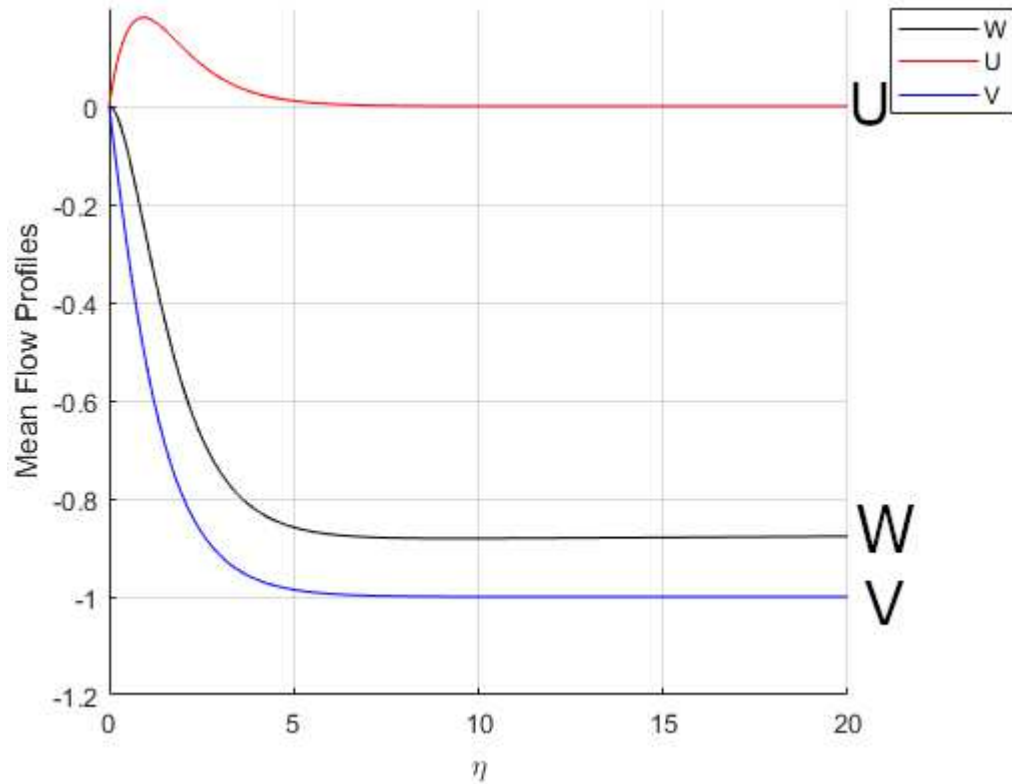


FIG. 2. Plot of the well known Von Kármán velocity profiles  $U, V, W$  for the rotating cone as seen in<sup>2,12</sup> in the range  $\eta = 0 - 20$

### III. ASYMPTOTIC LINEAR STABILITY ANALYSIS

To begin the linear stability analysis we must derive the estimates for the wavenumber  $\gamma_\delta^*$  and the wave angle  $\phi$  of the resulting disturbances formed on the boundary layer of the cone in the large Reynolds number limit. This is achieved by considering the type I and type II modes present in the system. To obtain the equations for linear disturbances, one must linearize Equations (1-4)

about the mean flow profile ( $u_b$ ) and the fluid pressure ( $p_b$ ). This is done in a similar way to<sup>2,12</sup> by introducing small perturbation quantities to both the mean flow profile and basic fluid pressure ( $\tilde{\mathbf{u}}$  and  $\tilde{p}^*$  respectively) as shown below:

$$\mathbf{u} = \mathbf{u}_b + \tilde{\mathbf{u}}, \quad (15)$$

$$p^* = p_b^* + \tilde{p}^*. \quad (16)$$

Where the perturbation quantities are given by:

$$\tilde{\mathbf{u}} = \Omega^* l^* \sin \psi (\tilde{u}, \tilde{v}, \tilde{w}), \quad (17)$$

$$\tilde{p}^* = (\rho^* \Omega^{*2} l^{*2} \sin^2 \psi) \tilde{p}. \quad (18)$$

Then non-dimensionalizing and removing non-linear terms from Equations (1-4) leads to:

$$\frac{\partial \tilde{u}}{\partial x} + \frac{\tilde{u} \sin \psi + \tilde{w} \cos \psi}{h} + \frac{1}{h} \frac{\partial \tilde{v}}{\partial \theta} + \frac{\partial \tilde{w}}{\partial z} = 0, \quad (19)$$

$$\begin{aligned} & \left( \frac{\partial}{\partial t} + xU \frac{\partial}{\partial x} + \frac{xV}{h} \frac{\partial}{\partial \theta} + R^{-1/2} W \frac{\partial}{\partial z} \right) \tilde{u} + U \tilde{u} + x \tilde{w} \frac{\partial U}{\partial z} - 2 \left( \frac{xV \sin \psi}{h} + 1 \right) \tilde{v} \\ & = -\frac{\partial \tilde{p}}{\partial x} + \frac{1}{R} \left( \nabla^2 \tilde{u} - \frac{(\tilde{u} \sin \psi + \tilde{w} \cos \psi) \sin \psi}{h^2} - \frac{2 \sin \psi}{h^2} \frac{\partial \tilde{v}}{\partial \theta} \right), \end{aligned} \quad (20)$$

$$\begin{aligned} & \left( \frac{\partial}{\partial t} + xU \frac{\partial}{\partial x} + \frac{xV}{h} \frac{\partial}{\partial \theta} + R^{-1/2} W \frac{\partial}{\partial z} \right) \tilde{v} + V \tilde{v} + x \tilde{w} \frac{\partial V}{\partial z} + \left( \frac{xV \sin \psi}{h} + 2 \right) (\tilde{u} + \tilde{w} \cot \psi) \\ & + \frac{(xU \sin \psi + R^{-1/2} W \cos \psi) \tilde{v}}{h} = -\frac{1}{h} \frac{\partial \tilde{p}}{\partial \theta} + \frac{1}{R} \left( \nabla^2 \tilde{v} + \frac{2 \sin \psi}{h^2} \frac{\partial \tilde{u}}{\partial \theta} + \frac{2 \cos \psi}{h^2} \frac{\partial \tilde{w}}{\partial \theta} - \frac{\tilde{v}}{h^2} \right), \end{aligned} \quad (21)$$

$$\begin{aligned} & \left( \frac{\partial}{\partial t} + xU \frac{\partial}{\partial x} + \frac{xV}{h} \frac{\partial}{\partial \theta} + R^{-1/2} W \frac{\partial}{\partial z} \right) \tilde{w} + R^{-1/2} \tilde{w} \frac{\partial W}{\partial z} - 2 \left( \frac{xV \sin \psi}{h} + 1 \right) \tilde{v} \cot \psi \\ & = -\frac{\partial \tilde{p}}{\partial z} + \frac{1}{R} \left( \nabla^2 \tilde{w} - \frac{(\tilde{u} \sin \psi + \tilde{w} \cos \psi) \cos \psi}{h^2} - \frac{2 \cos \psi}{h^2} \frac{\partial \tilde{v}}{\partial \theta} \right). \end{aligned} \quad (22)$$

These equations are the linearized perturbation equations. Where the quantity  $h = h^*/l^*$  and the quantity  $\nabla^2 = l^{*2} \nabla^{*2}$  represents the non-dimensional Laplacian operator for the perturbed equations. The main difference with these equations to the linearized equations featured in<sup>2,12</sup> is the inclusion of the time derivative term, which is required to obtain the relevant traveling mode terms in the asymptotic analysis.

### A. Inviscid type I modes

The type I modes analysis follows an almost identical process to the analysis shown in<sup>3</sup> except with an added scale factor of  $\sin \psi$ . The inviscid mode wavelength is scaled on boundary layer

thickness, which has the order of  $R^{-1/2}$  in the stream-wise and azimuthal directions. Then a small parameter is introduced,  $\varepsilon$ , which is given by  $\varepsilon = R^{-1/6}$  and we define the perturbation velocities and pressure as functions of the wall-normal coordinate  $z = \eta\varepsilon^3$ :

$$(\tilde{u}, \tilde{v}, \tilde{w}, \tilde{p}) = (u(z), v(z), w(z), p(z)) \exp \left\{ \frac{i}{\varepsilon^3} \left[ \int^x \alpha^I(x, \varepsilon) dx + \beta^I(\varepsilon)\theta - \varepsilon\omega_A^I t \right] \right\}. \quad (23)$$

The disturbance quantities  $\alpha^I$  and  $\beta^I$  are considered as real quantities as the disturbances associated with these perturbations are neutrally stable. The traveling mode frequency is given by  $\omega_A^I = \omega/R$ . We expand these quantities as well as the traveling mode frequency term  $\omega_A^I$  to get:

$$\alpha^I = \alpha_0^I + \varepsilon\alpha_1^I + \dots, \quad (24)$$

$$\beta^I = \beta_0^I + \varepsilon\beta_1^I + \dots, \quad (25)$$

$$\omega_A^I = \omega_0^I + \varepsilon\omega_1^I + \dots. \quad (26)$$

Where the perturbation of the radial velocity is given by:

$$u = u_0(\eta) + \varepsilon u_1(\eta) + \dots, \quad (27)$$

with similar expansions for  $v, w$  and  $p$ . These expressions are then used to solve the resulting perturbation equations at each order. For the leading order eigenmodes, it is found that the frequency terms are removed at this order, so the results of the leading order are the same as found in<sup>12</sup>. For the first order eigenmodes, we follow a similar method as the Garret group<sup>2</sup> and observe the existence of two layers, an inviscid layer with thickness  $O(\varepsilon^3)$  and a viscous layer with thickness  $O(\varepsilon^4)$ . We then use the wall normal coordinate  $\xi = \varepsilon^4 z$  to match the leading order solution to the first order solution which results in:

$$\frac{w'_0(0)Ai'(\tau_0)}{\gamma \int_{\tau_0}^{\infty} Ai(s)ds} = 2 \left( \alpha_0^I \alpha_1^I + \frac{\beta_0^I \beta_1^I}{x^2 \sin^2 \psi} \right) I_1 + \left( \frac{\alpha_1^I}{\beta_0^I} - \frac{\beta_1^I \alpha_0^I}{\beta_0^{I2}} \right) x \sin \psi I_2 + x \omega_0^I I_3. \quad (28)$$

The function  $w$  represents the leading order Rayleigh normalized eigenfunction, which has the gradient  $w'(0) = 1$  (the plot of which is shown in Figure (3.2) in Hussain's Thesis<sup>12</sup>). The value of  $\gamma$  is defined as:  $\gamma = \left[ i(\alpha_0^I \bar{u}_0 x + \beta_0^I \bar{v}_0 / \sin \psi) \right]^{1/3}$ . The wall normal coordinate has been rescaled in the same way as Hussain<sup>3</sup> so that  $\tau = \gamma \xi - \tau_0$ , where  $\tau_0 = -i\omega_0^I / \gamma^2$ . Notice that Equation (28) and the expression for  $\gamma$  is very similar to the expression obtained by Hussain<sup>3</sup> apart from the introduction of a  $\sin \psi$  term due to the changing half angle for the rotating cone case. The integrals  $I_1, I_2$  are the same as Equations 3.44 and 3.45 in Hussain's Thesis<sup>12</sup>. These integrals and

$I_3$  are calculated using the Simpsons numerical integration method, where the integral for  $I_3$  is represented as:

$$I_3 = \int_0^\infty w_0^2(\theta) \frac{\overline{\overline{U}}''}{\overline{\overline{U}}} d\theta. \quad (29)$$

Where  $\overline{\overline{U}} = \alpha_0 x U + \beta_0 V / \sin \psi$  is the effective velocity profile which is defined in<sup>2</sup>. For the integrals  $I_2$  and  $I_3$ , we must use residue theorem to integrate around a singularity that is caused when  $\overline{\overline{U}} = \overline{\overline{U}}' = 0$ . The results of these integrals are given as:

$$I_1 = 0.096561, \quad (30)$$

$$I_2 = 0.058240 + 0.031535i, \quad (31)$$

$$I_3 = -4.443651 - 1.002451i. \quad (32)$$

## B. Viscous type II modes

To analyse the viscous type II modes, we build a triple deck structure similar to<sup>3,9</sup> using the small parameter  $\varepsilon = R^{-1/16}$ . The lower, main and upper deck are built with thickness  $O(\varepsilon^9)$ ,  $O(\varepsilon^8)$  and  $O(\varepsilon^4)$  respectively. We define the inner variables which have  $O(1)$  at the respective layers as  $\xi$ ,  $\zeta$  and  $Z$ . Using this setup, the streamwise and azimuthal wave numbers  $\alpha, \beta$  are scaled upon a viscous length scale so the velocity and pressure perturbations become the values:

$$(\tilde{u}, \tilde{v}, \tilde{w}, \tilde{p}) = (u(z), v(z), w(z), p(z)) \exp\left(\frac{i}{\varepsilon^4} \left[ \int^x \alpha^{II}(x, \varepsilon) dx + \beta^{II}(\varepsilon) \theta - \varepsilon^2 \omega_A^{II} t \right]\right). \quad (33)$$

And we expand the streamwise and azimuthal wavenumbers as well as the frequency term to get:

$$\alpha^{II} = \alpha_0^{II} + \varepsilon^2 \alpha_1^{II} + \varepsilon^3 \alpha_2^{II} + \dots, \quad (34)$$

$$\beta^{II} = \beta_0^{II} + \varepsilon^2 \beta_1^{II} + \varepsilon^3 \beta_2^{II} + \dots, \quad (35)$$

$$\omega_A^{II} = \varepsilon \omega_0^{II} + \varepsilon^2 \omega_1^{II} + \varepsilon^3 \omega_2^{II} + \dots. \quad (36)$$

Note that the order  $\varepsilon$  terms for  $\alpha^{II}$  and  $\beta^{II}$  are zero, and  $\alpha_j^{II}$  and  $\beta_j^{II}$  are real quantities. As with the case for Section (III A) the analysis follows the method shown in<sup>3</sup> apart from the introduction of a factor of  $\sin \psi$ . The result of this triple deck analysis leads to the eigenrelation for type II as:

$$\gamma_0^2 I_4 + \frac{i \gamma_0 U_0 \sin \psi}{\beta_0^{II}} \left(1 + \frac{V_0^2}{U_0^2}\right) I_5 + \frac{\Delta^{\frac{3}{4}} i \omega_0^{II} \gamma_0 (\sin \psi)^2}{\beta_0^{II^2}} I_6 = \frac{i \Delta^{\frac{1}{2}} \gamma_0 (\sin \psi)^2}{\beta_0^{II^2}} \left( \alpha_1^{II} x U_0 + \frac{\beta_1^{II} V_0}{\sin \psi} \right). \quad (37)$$

Where  $\gamma_0 = (\alpha_0^{II^2} + \beta_0^{II^2}/x^2 \sin^2 \psi)^{1/2}$  and  $\Delta = i \left( \alpha_0^{II} x U_1 + \frac{\beta_0^{II} V_1}{\sin \psi} \right)$ . The integrals  $I_4, I_5$  are the same expressions as  $I_3, I_4$  in Equations (4.68) and (4.69) in<sup>12</sup>. The Integral  $I_6$  is represented by:

$$I_6 = \frac{\int_0^\infty \theta^2 U_c(0, \theta) d\theta}{\sqrt{2} U_c(0, 0)}. \quad (38)$$

Where  $U_c(0, \theta)$  is the parabolic cylinder function as defined in<sup>23</sup>. Similar to the type I integrals,  $I_4, I_5$  and  $I_6$  are solved using the Simpsons rule integration method. The solutions are given as:

$$I_4 = 0.598393, \quad (39)$$

$$I_5 = 0.456945, \quad (40)$$

$$I_6 = 1.346820. \quad (41)$$

In order to solve Equation (37), we use the methods to investigate the boundary layer structure discussed in<sup>3,12</sup>. In the upper deck, the disturbances decay exponentially. Whilst in the main deck, we use the no slip condition (an interested reader can refer to Hussain's thesis<sup>12</sup> for more detail) which argues that the effective wall shear tends to zero. This motivates us to choose the leading order radial and azimuthal wavenumbers so that they satisfy the expression:

$$\alpha_0^{II} U'(0) + \frac{\beta_0^{II} V'(0)}{x \sin \psi} = 0. \quad (42)$$

For the lower deck, the decay of the leading order solution is represented in terms of the parabolic cylinder function  $U_c(0, \sqrt{2}\Delta^{1/4}\xi)$  (which is defined in<sup>23</sup>) through the balance of the Coriolis and viscous forces:

$$\Delta = i \left( \alpha_0^{II} x U''(0) + \frac{\beta_0^{II} V''(0)}{\sin \psi} \right). \quad (43)$$

#### IV. ASYMPTOTIC TRAVELING MODES ANALYSIS

For the analysis on traveling modes in this section, the non-dimensional frequency values that were used were  $\omega = -5, 0, 4, 7.9, 10$ . Where negative values of  $\omega$  are interpreted as modes traveling slower than the cones surface, and positive values of  $\omega$  are interpreted as traveling faster than the cone surface. These were chosen to allow for comparison with the asymptotic cases for the the rotating disk case in<sup>3</sup> as well as the frequency of zero corresponds to stationary modes to test the validity when compared to previous asymptotic analysis on rotating cones<sup>2,12</sup>.

### A. Inviscid type I modes

For the analysis of the type I modes, it was discovered that like the rotating disk case, there are no time dependent terms for the leading order equations, meaning that the solutions at leading order are the same as the solutions for stationary modes. The time dependent terms manifest, however, in the first order terms. We solve the eigenvalue equation (Equation (28)) for our various frequency values which results in the following expressions for the wavenumber and the wave angle respectively:

$$\gamma_{\delta^*}^1 = 1.162 - B_t^1 R_{\delta^*}^{-1/3} (\sin \psi)^{1/6} + \dots, \quad (44)$$

$$\tan\left(\frac{\pi}{2} - \phi\right) = \frac{4.256}{\sin \psi} + D_t^1 R_{\delta^*}^{-1/3} (\sin \psi)^{-5/6} + \dots, \quad (45)$$

where  $R_{\delta^*} = R^{1/2} x (\sin \psi)^{1/2}$  is the Reynolds number that has been scaled based on boundary layer thickness. We use this scaled Reynolds number to convert the numerical frequency into the asymptotic frequency which allows us to calculate the frequency without explicitly calculating the value of  $x$ . This is done using the relation:

$$\omega_0^I x^{-2/3} = \omega R_{\delta^*}^{-2/3} (\sin \psi)^{1/3}. \quad (46)$$

Where  $\omega_0^I x^{-2/3}$  is the asymptotic frequency for type I mode. The values for  $B_t^1$  and  $D_t^1$  are given in Table (I) for the fixed Reynolds number of  $R_{\delta^*} = 10^7$ , and  $\psi = 70^\circ$ . Using these values of  $B_t^1$

$\omega$	$\omega_0^I x^{-2/3}$	$B_t^1$	$D_t^1$
-5	-0.000106	8.312592	16.522721
0	0.000000	8.311373	16.526076
4	0.000084	8.310398	16.528759
7.9	0.000167	8.309447	16.531375
10	0.000211	8.308935	16.532784

TABLE I. Table of  $B_t^1$  and  $D_t^1$  values for each frequency values at  $R_{\delta^*} = 10^7$ ,  $\psi = 70^\circ$

and  $D_t^1$ , as well as the rest of the Reynolds number values between  $10^4$  and  $10^7$ , we can now plot the solution of the wavenumber and wave angle against the re-scaled Reynolds number for each of these frequency values. We plot the change in frequency for a fixed half angle (chosen as  $70^\circ$ ) in Figures (3) and (4) to have a better view of the effects of the change of frequency on the wavenumber and waveangle respectively.

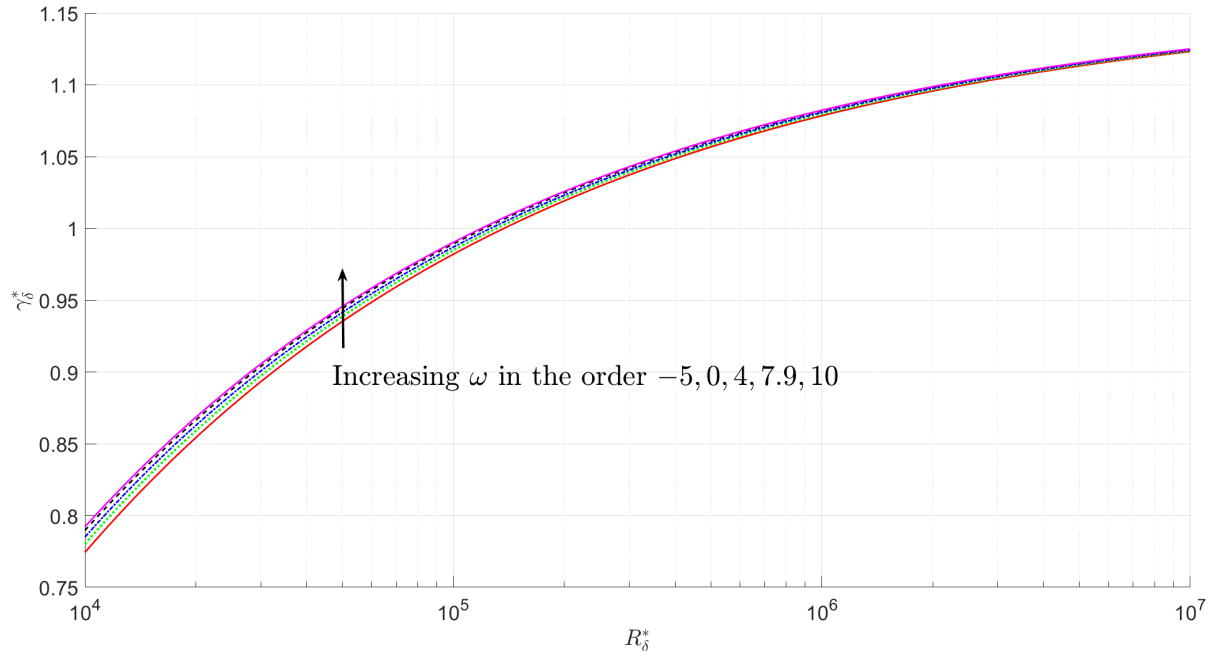


FIG. 3. Plot of the type I wavenumber ( $\gamma_\delta$ ) for  $\psi = 70^\circ$  for  $\omega = -5, 0, 4, 7.9, 10$  against the rescaled Reynolds number  $R_\delta^*$ . Where  $\omega = -5$  (top solid line),  $\omega = 0$  (dotted line),  $\omega = 4$  (dot-dashed line),  $\omega = 7.9$  (dashed line) and  $\omega = 10$  (bottom solid line)

## B. Viscous type II modes

Solving the viscous type II modes leads to the observation that the upper and main deck solutions leads to Equation (42). We also find that the time dependent terms do not appear until the first order problem in the lower deck. Using this, we solve Equation (37) to obtain the estimates for the leading order wavenumber and the first order wave angle. By equating and comparing real and imaginary parts we obtain the following eigenrelation:

$$a\bar{\omega}_0 + b\bar{\gamma}_0^{1/4} - \bar{\gamma}_0^{9/4} = 0. \quad (47)$$

Where  $\bar{\omega}_0 = \omega_0^I x^{-1/8}$  and  $\bar{\gamma}_0 = \gamma_0 x^{1/2}$  are the re-scaled frequency and wavenumber terms respectively. The value of  $\omega_0^I x^{-1/8}$  is given as:

$$\omega_0^I x^{-1/8} = \omega R_\delta^{*-1/8} (\sin \psi)^{1/16}, \quad (48)$$

and the quantities  $a$  and  $b$  are represented as:

$$a = \frac{[\cos \frac{3\pi}{8} - \sin \frac{3\pi}{8}] \left(\frac{V_0}{U_0}\right)^{3/4} \left(\frac{1}{2}\right)^{3/4} I_6}{I_4} \left(1 + \frac{V_0^2}{U_0^2}\right)^{5/8}, \quad (49)$$

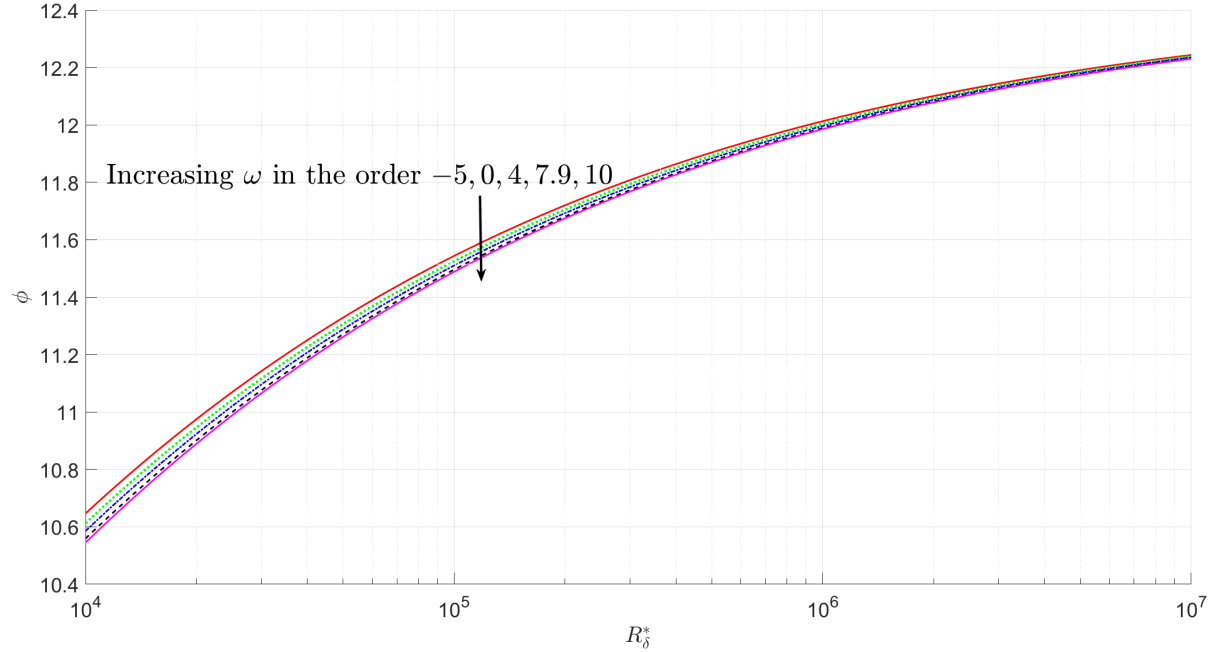


FIG. 4. Plot of the type I waveangle ( $\phi$ ) for  $\psi = 70^\circ$  for  $\omega = -5, 0, 4, 7.9, 10$  against the re-scaled Reynolds number  $R_\delta^*$ . Where  $\omega = -5$  (top solid line),  $\omega = 0$  (dotted line),  $\omega = 4$  (dot-dashed line),  $\omega = 7.9$  (dashed line) and  $\omega = 10$  (bottom solid line)

$$b = \frac{U_0 \left(1 + \frac{V_0^2}{U_0^2}\right)^{3/2} I_5}{I_4}. \quad (50)$$

Then substituting the solution of Equation (47) back into Equation (37) gives the following eigenrelation for the first order wave angle:

$$\bar{\Phi}_1 = d \left( \bar{\gamma}_0^{3/2} + c \bar{\omega}_0 \bar{\gamma}_0^{-3/4} \right) = \sin \psi \left( \frac{\alpha_1}{\beta_0} - \frac{\beta_1 \alpha_0}{\beta_0^2} \right) x^{-5/4}. \quad (51)$$

Where the constants  $c$  and  $d$  are given by:

$$c = \frac{\sin \frac{3\pi}{8} I_6 \left(1 + \frac{V_0^2}{U_0^2}\right)^{5/8} \left(\frac{V_0}{U_0}\right)^{3/4} \left(\frac{1}{2}\right)^{3/4}}{I_4 \left(1 + \frac{V_0}{U_0}\right)^2}, \quad (52)$$

$$d = \frac{2I_4 \left(1 + \frac{V_0}{U_0}\right)^2}{\left(1 + \frac{V_0^2}{U_0^2}\right)^{1/4} |U_0 V_0|^{1/2}}. \quad (53)$$

Where  $\bar{\Phi}_1 = \bar{\Phi}_1 x^{-5/4} = \sin \psi \left( \alpha_1^{II} / \beta_0^{II} - \beta_1^{II} \alpha_0^{II} / \beta_0^{II^2} \right) x^{-5/4}$  is the re-scaled wave angle term and  $U_0 = U'(0), V_0 = V'(0)$ . The plots of the eigenrelation equations (47 and 51) are shown in Figures (5) and (6) respectively.

This is the author's peer reviewed, accepted manuscript. However, the online version of record will be different from this version once it has been copyedited and typeset.  
PLEASE CITE THIS ARTICLE AS DOI:10.1063/1.50033202

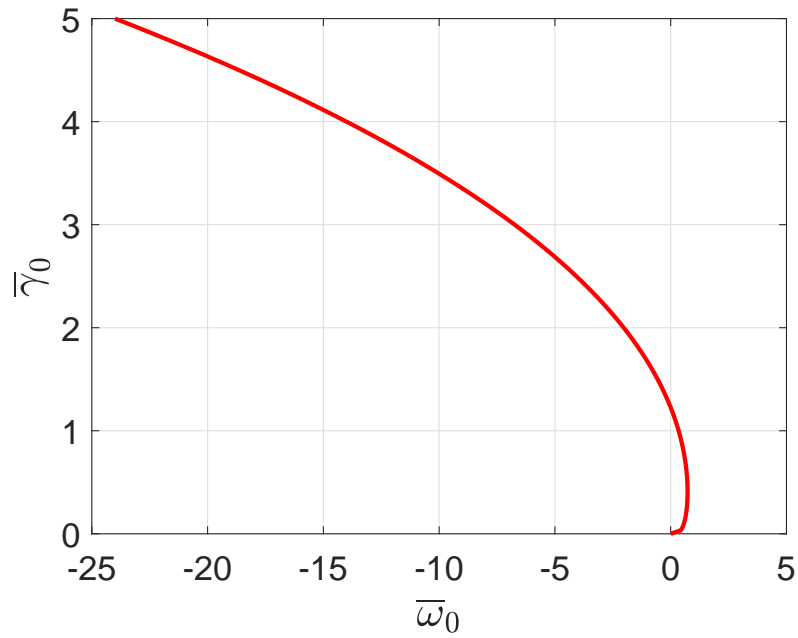


FIG. 5. Plot of the type II rescaled asymptotic frequency  $\bar{\omega}_0$  against the re-scaled asymptotic wavenumber  $\bar{\gamma}_0$

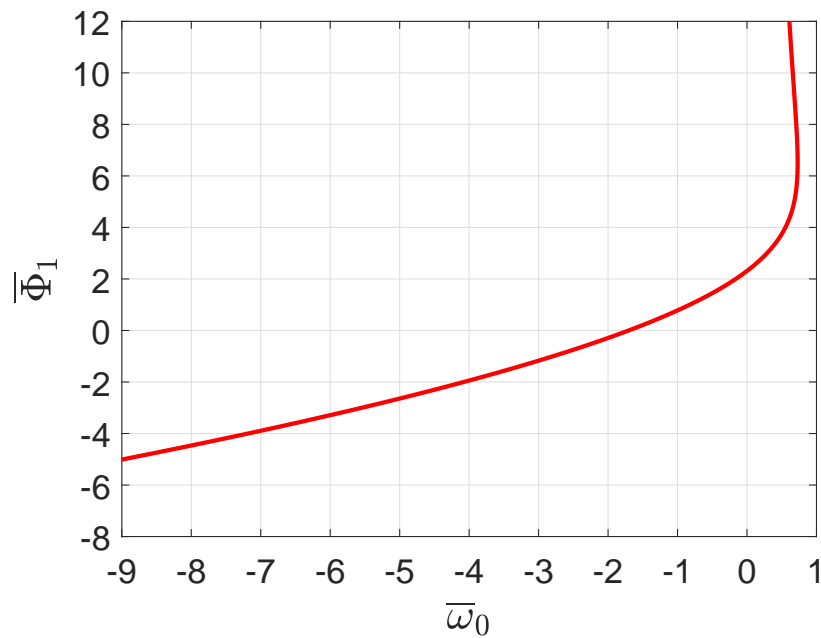


FIG. 6. Plot of the the type II rescaled asymptotic frequency  $\bar{\omega}_0$  against the rescaled asymptotic waveangle  $\bar{\Phi}_1$

We then get expressions for the wavenumber and wave angle respectively by solving for the values of Equation (47) and (51) to get:

$$\gamma_0 = A^{II} R_\delta^{*-1/2}, \quad (54)$$

$$\tan\left(\frac{\pi}{2} - \phi\right) = C^{II} + D^{II} R_\delta^{*-1/4}. \quad (55)$$

Where  $A^{II}$ ,  $C^{II}$  and  $D^{II}$  are given as:

$$A^{II} = \bar{\gamma}_0 (\sin \psi)^{1/4}, \quad (56)$$

$$C^{II} = \frac{1.207}{\sin \psi}, \quad (57)$$

$$D^{II} = \bar{\Phi}_1 (\sin \psi)^{-7/8}. \quad (58)$$

The numerical values of these variables for each frequency value are given in Table II (for the fixed Reynolds number value of  $R_\delta^* = 10^7$  and  $\psi = 70^\circ$ ). We see from Figure 5, there are no solutions for  $\omega_0 x^{-1/8} > 0.7288$  which limits the available frequencies for comparison. Notice that there are two branches for the positive frequency values of  $\omega > 0$ . This was also observed in<sup>3,11</sup> for the case of the rotating disk and appears due to the existence of two solutions at this value of  $\omega$  when solving the eigenrelations for the wave angle and the wavenumber simultaneously as seen also in Figure (5). The results of the predicted wavenumber for the frequency values of  $\omega = -5, 0, 4$  and the type II second branch of 4 are shown in Figure 7 and the waveangle for each frequency are given in Figure 8.

TABLE II. Numerical values of  $A^{II}$ ,  $C^{II}$  and  $D^{II}$  for  $R_\delta^* = 10^7$ ,  $\psi = 70^\circ$

$\omega$	$\omega_0^{II} x^{-1/8}$	$C^{II}$	$A^{II}$	$D^{II}$
-5	-0.664174	1.284463	1.516669	1.282383
0	0.000000	1.284463	1.206132	2.441395
4	0.531339	1.284463	0.815349	4.109524
4 (second branch)	0.531339	1.284463	0.071911	17.043524

### C. Asymptotic results for both type I and II modes

We now look at both the type I and type II modes results for the wavenumber for each frequency value in Figures (9-11). And the type I and II modes results for the waveangle in Figures (12-14).

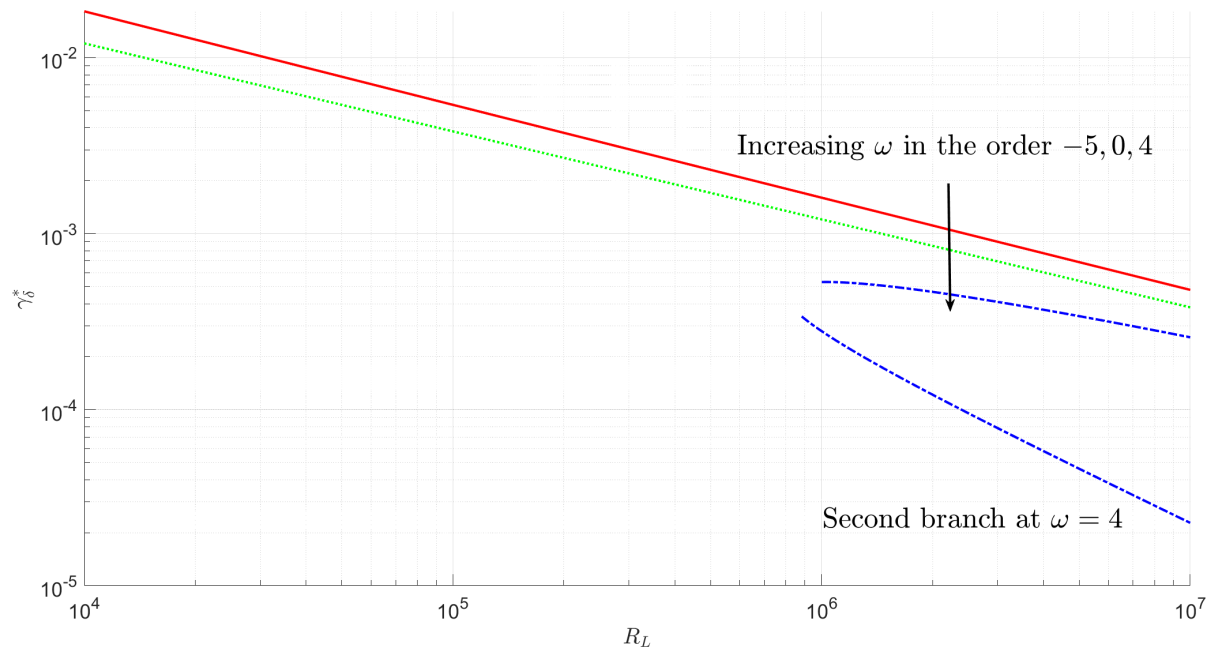


FIG. 7. Plot of the type II wavenumber  $\gamma_\delta^*$  for each value of  $\omega$ . Where  $\omega = -5$  (solid line),  $\omega = 0$  (dashed line) and  $\omega = 4$  (dot-dashed line)

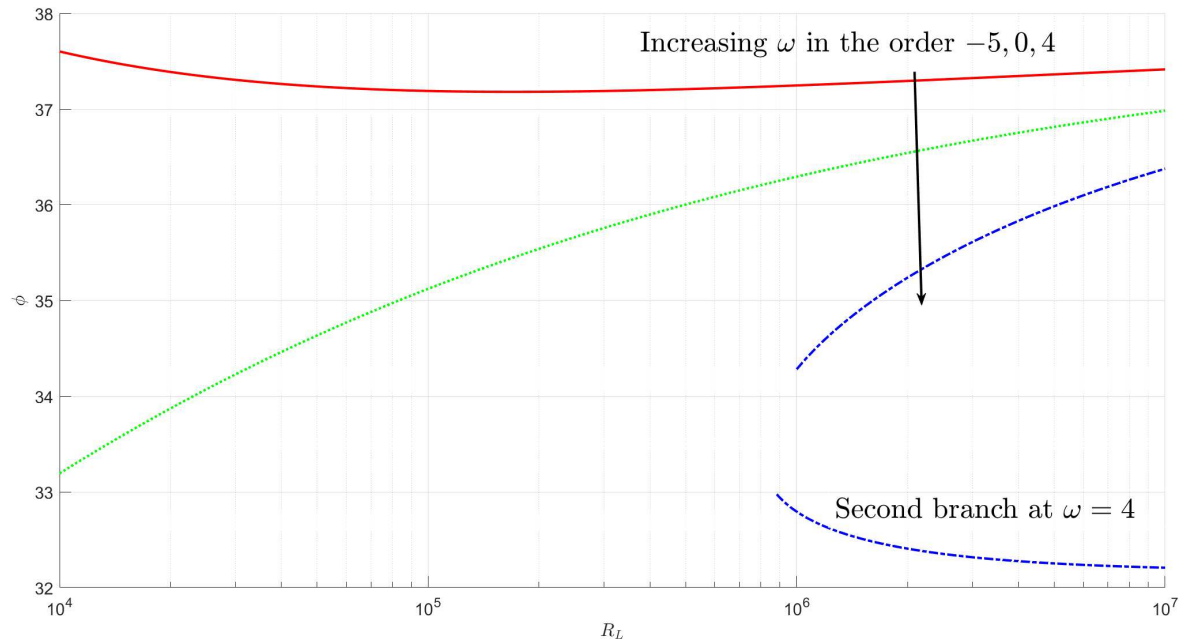


FIG. 8. Plot of the type II waveangle  $\phi$  for each value of  $\omega$ . Where  $\omega = -5$  (solid line),  $\omega = 0$  (dashed line) and  $\omega = 4$  (dot-dashed line)

It is to be noted we have only plotted the frequencies up to  $\omega = 4$  due to there being no solutions for the type II branch for the frequency values 7.9, 10.

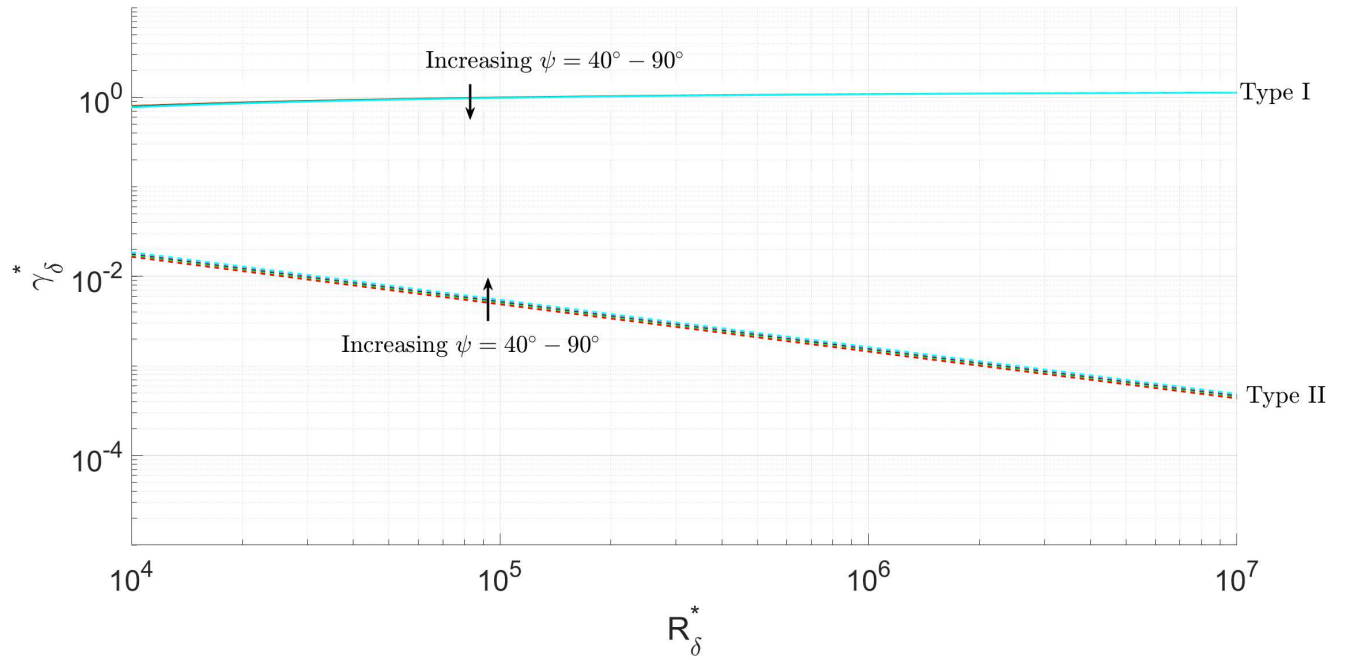


FIG. 9. Plot of the wavenumber  $\bar{\gamma}_0$  for  $\omega = -5$  for half angles  $40^\circ - 90^\circ$ . Where the Type I branch (solid line), Type II branch (dashed line)

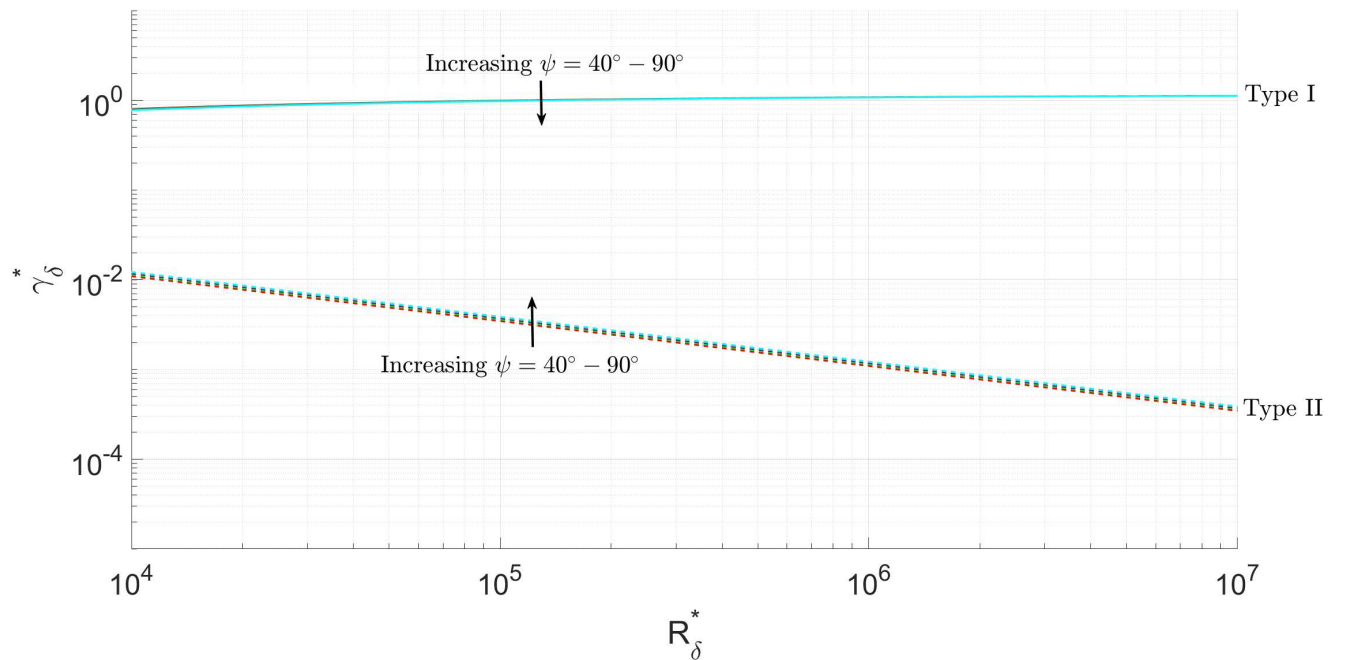


FIG. 10. Plot of the wavenumber  $\bar{\gamma}_0$  for  $\omega = 0$  for half angles  $40^\circ - 90^\circ$ . Where the Type I branch (solid line), Type II branch (dashed line)

The results of the type I study show that the effects of traveling modes on the predicted effective

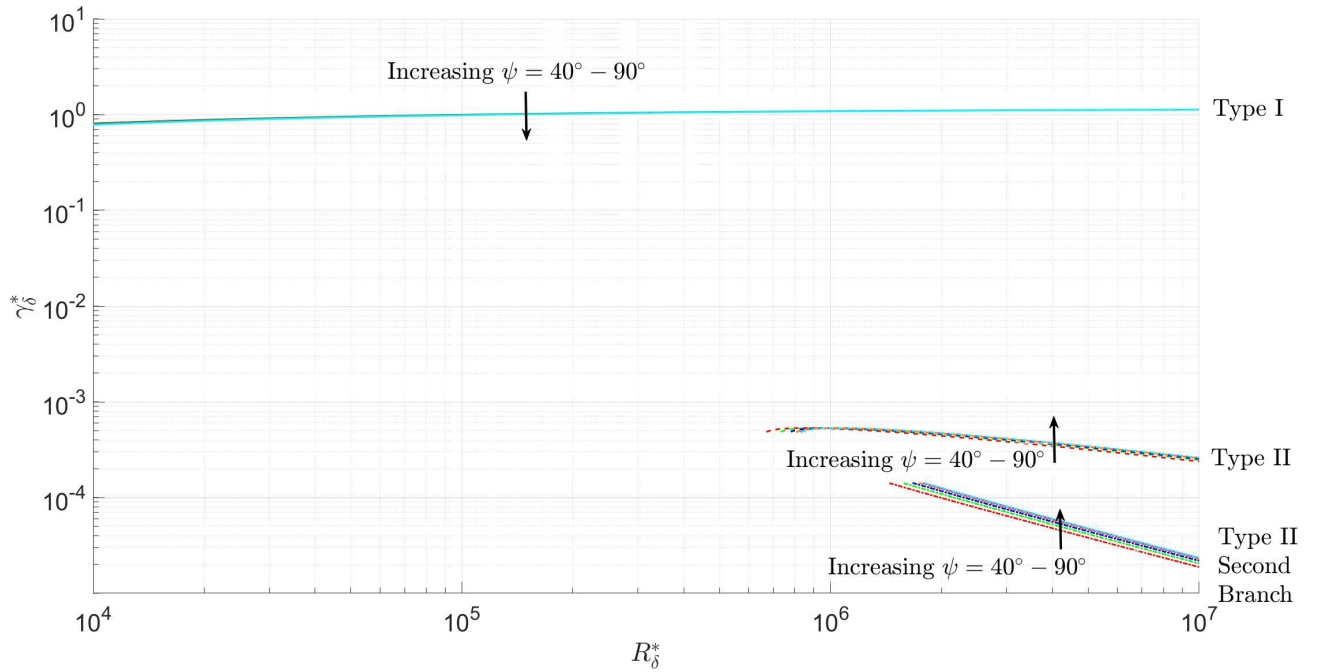


FIG. 11. Plot of the wavenumber  $\bar{\gamma}_0$  for  $\omega = 4$  for half angles  $40^\circ - 90^\circ$ . Where the Type I branch (solid line), Type II branch (dashed line) and Type II Second Branch (SB) is represented by a dot dashed line

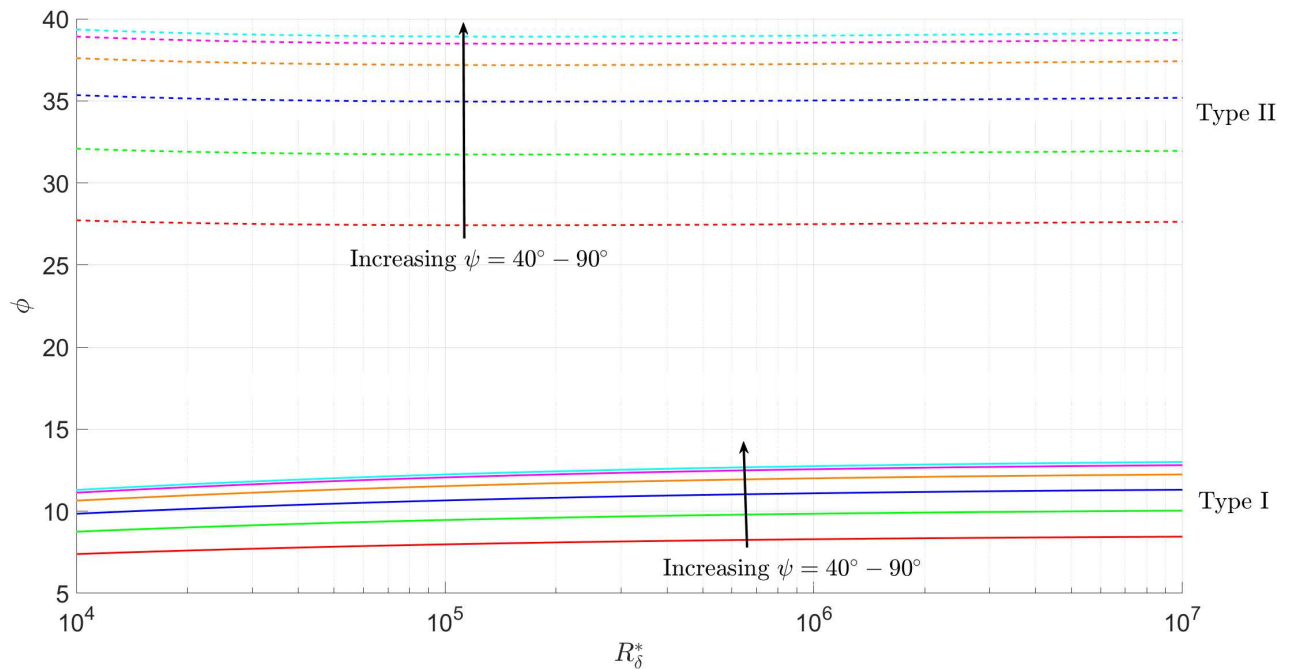


FIG. 12. Plot of the wave angle  $\phi$  for  $\omega = -5$  for half angles  $40^\circ - 90^\circ$ . Where the Type I branch (solid line), Type II branch (dashed line)

wavenumber and waveangle are slight. As the frequency increases from  $\omega = -5$  to  $\omega = 10$  we see

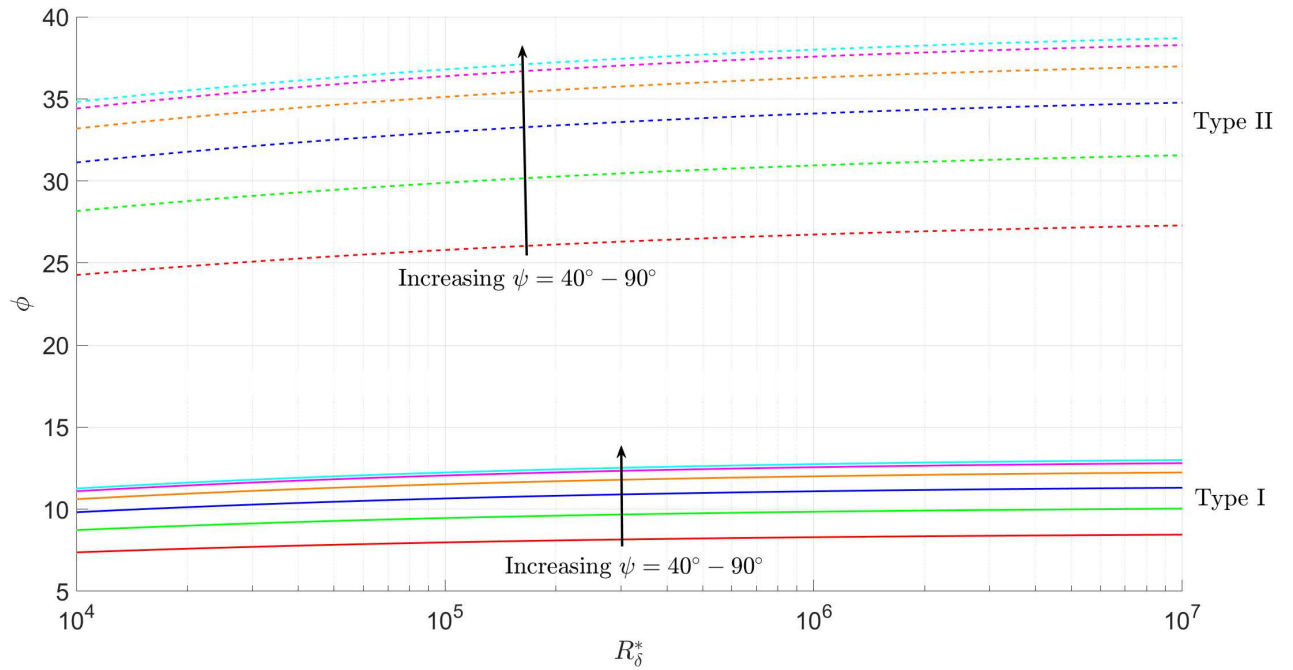


FIG. 13. Plot of the wave angle  $\phi$  for  $\omega = 0$  for half angles  $40^\circ - 90^\circ$ . Where the Type I branch (solid line), Type II branch (dashed line)

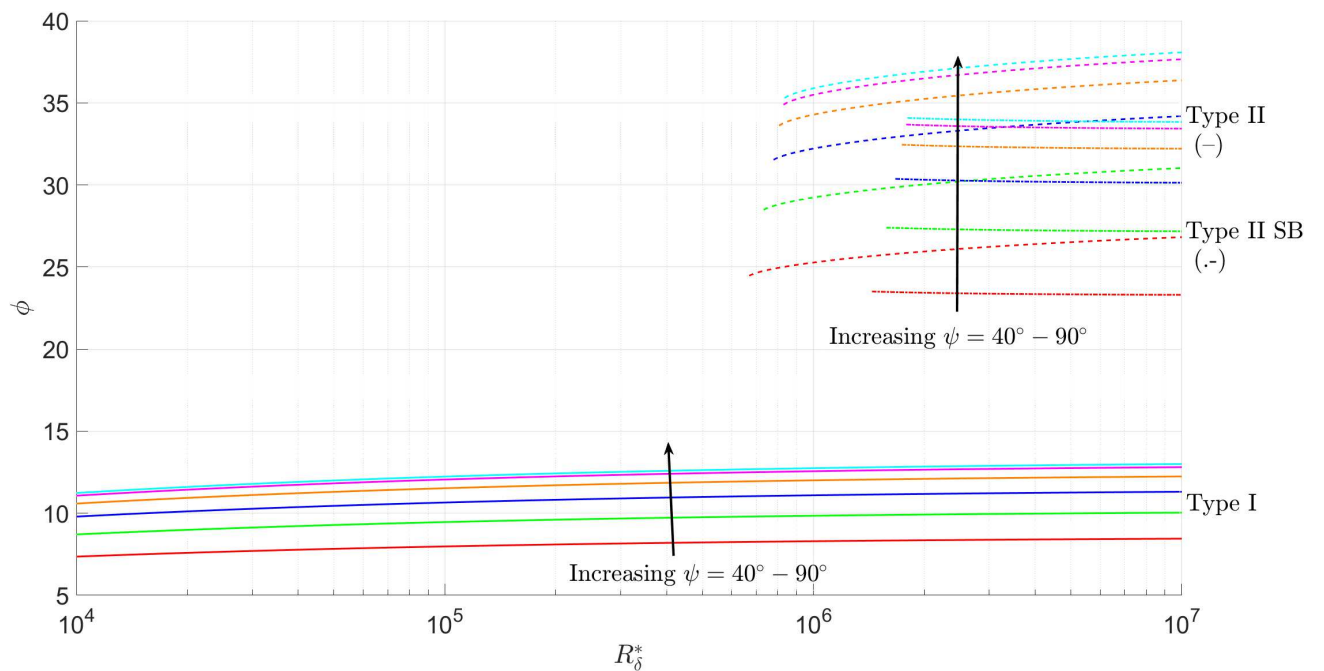


FIG. 14. Plot of the wave angle  $\phi$  for  $\omega = 4$  for half angles  $40^\circ - 90^\circ$ . Where the Type I branch (solid line), Type II branch (dashed line) and Type II Second Branch (SB) is represented by a dot dashed line

that it reduces the effective wavenumber, which in turn decreases the area of the stable region. This

means that as the wave frequency becomes faster than the rotation of the cone, the more unstable the system becomes. It also shows that as we reduce the frequency of the waves in relation to the cone, the more stable the system becomes. However, the asymptotics at negative frequency values around  $\omega = -5$  cause the waveangle around the lower Reynolds numbers ( $R_\delta^* = 10^4$ ) to begin to curve upwards, which may be caused by a change in sign in the higher order terms. Though since it only occurs at the lower end of the Reynolds number domain, it is of little concern as the valid region for our analysis is the high Reynolds numbers ( $R_\delta^* = 10^6$ ). Also notice from Figures 3 and 4 that as the Reynolds number increases towards  $R_\delta^* = 10^7$ , the effect of traveling modes reduces on the wavenumber and waveangle, this is due to the high Reynolds number causing the asymptotic frequency value to become very small in order to allow valid comparison to the numerical frequency value. For type II modes, we see that traveling modes have a much more significant effect on the effective wavenumber and the waveangle. We see similar effects to type I modes in that as the frequency increases, the area of the stable region decreases, which also suggests that as expected that as the frequency increases the more unstable the system becomes. We also notice that there is a presence of a second branch for positive frequency values for the type II modes. This second branch has also been seen in previous traveling mode asymptotic studies for the rotating disks in<sup>3,11</sup>. However, when comparing the plots with those obtained by Turkyilmazoglu, we see that the second branch obtained in our study (see Figure 7) occurs at a much lower wavenumber range. This result could be due to our study not considering non-linear terms. Another feature of the Figure (11) and Figure (14) is the cut off point for the type II branch at around  $R_\delta^* = 10^6$ . This is due to the asymptotic frequency term becoming larger than the limit of  $\omega_0 x^{-1/8} > 0.7288$ . This shows that there is a limit for the results for positive frequency values using this asymptotic method. This limit decreases as the frequency value decreases until it reaches  $\omega = 0$ , at which point this solution limit disappears due to the asymptotic frequency term never exceeding  $\omega_0 x^{-1/8} = 0.7288$  at these positions. We see this limit in Figures 11 and 14 also decreases as the half angle increases for the type II branch due to the  $\sin(\psi)$  in Equation 48.

## V. NUMERICAL ANALYSIS

### A. Numerical problem formulation

We now present a numerical analysis for the rotating cone in still fluid with traveling modes case. In this case we use a slightly different basic flow setup than with the asymptotic method in Section III. The altered basic flow equations are given by:

$$\begin{aligned} U'' &= WU' + (U^2 - V^2) \sin \psi, \\ V'' &= WV' + 2UV \sin \psi, \\ W' &= -2U \sin \psi. \end{aligned} \quad (59)$$

Which are the same as the Equations (2-5) in the paper<sup>17</sup>. Notice these basic flow equations now have dependence on the half angle of the cone and the Coriolis force terms are removed. The numerical stability analysis is conducted at local points along the cone surface  $x^* = x_L^*$ , with the local surface radius given by  $r_L^* = x_L^* \sin \psi$ . We use the same non-dimensionalizing procedure as<sup>2</sup> to get the local Reynolds number given by:

$$R_L = \frac{x_L^* \Omega^* \delta^* \sin \psi}{\nu^*} = x_L \sin \psi = r_L. \quad (60)$$

This differs from the Reynolds number defined in our asymptotic study, but is equivalent to the displacement thickness Reynolds number  $R_\delta^*$  such that  $R_L = R_\delta^*$ , which facilitates comparisons between the asymptotic and numerical solutions. Next we must derive our disturbance equations. First we follow the steps in the paper<sup>2</sup> and define the small perturbation quantities as:

$$\tilde{U}(\eta, x, \theta, t; R_L, \psi) = \frac{r_L}{R_L} U(\eta; \psi) + \hat{u}(\eta, x, \theta, t; R_L, \psi), \quad (61)$$

$$\tilde{V}(\eta, x, \theta, t; R_L, \psi) = \frac{r_L}{R_L} V(\eta; \psi) + \hat{v}(\eta, x, \theta, t; R_L, \psi), \quad (62)$$

$$\tilde{W}(\eta, x, \theta, t; R_L, \psi) = \frac{1}{R_L} W(\eta; \psi) + \hat{w}(\eta, x, \theta, t; R_L, \psi), \quad (63)$$

$$\tilde{P}(\eta, x, \theta, t; R_L, \psi) = \frac{1}{R_L^2} P(\eta; \psi) + \hat{p}(\eta, x, \theta, t; R_L, \psi). \quad (64)$$

Where the hatted quantities represent small unsteady perturbations and the non hatted quantities represent the non-dimensional flow terms which are determined by equation (59). Note also that  $\eta = z^*/\delta^*$ . Then the non-dimensional continuity and Navier-Stokes equations are linearized with

respect to these perturbation quantities and the parallel flow approximation is made. This approximation ignores the variation in  $R_L$  with local surface cross-sectional radius and assumes that  $\eta_n/r_L \ll 1$  and the resulting equations are strictly local. This assumption that  $R_L \gg 1$  prohibits analysis close to the apex at which  $R_L = O(1)$ . The perturbation quantities can then be expressed in normal mode form:

$$(\hat{u}, \hat{v}, \hat{w}, \hat{p}) = ((u(\eta; \psi), v(\eta; \psi), w(\eta; \psi), p(\eta; \psi)) \exp(i(\alpha x \sin \psi + \beta R_L \theta - \omega_A t))). \quad (65)$$

Where the wavenumber in the  $x$ -direction  $\alpha = \alpha_r + i\alpha_i$  is complex as required by the spacial analysis and the circumferential wave number  $\beta$  (of  $O(1)$ ) and the frequency  $\omega_A$  are real quantities. The azimuthal wavenumber  $n = \beta R_L$  is an integer quantity representing the number of vortices present on the cone. Our numerical method differs from the continuation of the method shown in<sup>2</sup> (who uses a Runge-Kutta method to solve a transformed eigenvalue problem) and instead obtain a set of quadratic eigenvalue equations:

$$\alpha^2 \left( \frac{\tilde{u}}{R_L} \right) + \alpha (iU\tilde{u} + i\tilde{p}) + \left( M_x + \frac{U \sin \psi}{R_L} \right) \tilde{u} + \left( \frac{W}{R_L} \right) \tilde{u}' - \frac{\tilde{u}''}{R_L} - \left( \frac{2V+2}{R_L} \right) \tilde{v} \sin \psi + U' \tilde{w} = 0, \quad (66)$$

$$\begin{aligned} \alpha^2 \left( \frac{\tilde{v}}{R_L} \right) + \alpha (iU\tilde{v}) + \left( M_x + \frac{U \sin \psi}{R_L} \right) \tilde{v} + \frac{2V+2}{R_L} \tilde{u} \sin \psi + \frac{W}{R_L} \tilde{v}' - \frac{1}{R_L} \tilde{v}'' \\ + V' \tilde{w} + \frac{2V+2}{R_L} \tilde{w} \cos \psi + \frac{i\beta}{R_L} \tilde{p} = 0, \end{aligned} \quad (67)$$

$$\alpha^2 \left( \frac{\tilde{w}}{R_L} \right) + \alpha (iU\tilde{w}) - \frac{2V+2}{R_L} \tilde{v} \cos \psi + \left( M_x - \frac{2U \sin \psi}{R_L} \right) \tilde{w} + \frac{W}{R_L} \tilde{w}' - \frac{\tilde{w}''}{R_L} + \tilde{p} = 0, \quad (68)$$

$$\alpha (i\tilde{u}) + \frac{1}{R_L} \tilde{u} \sin \psi + \frac{i\beta \tilde{v}}{R_L} + \tilde{w}' + \frac{\tilde{w}}{R_L} \cos \psi = 0. \quad (69)$$

Where  $M_x = i\beta V + \frac{\beta^2}{R_L} - i\omega_A$ . These equations are equivalent to the equations shown in<sup>22</sup> with the temperature dependent terms removed and half angle terms  $\psi$  included.

## B. Numerical results

These eigenvalue equations are then solved using a spectral method using Chebyshev polynomials. Similar to<sup>3</sup> we use the dimensionless frequency term  $\omega = \omega_A R_L$  and calculate the neutral curves using a fixed  $\omega$  which determines the value of  $\omega_A$  at each value of  $R_L$ . Then use this value

of  $\omega_A$  and steps in  $n = \beta R_L$  (where  $\beta$  is obtained from  $\beta/R_L$ ) to calculate the value of  $\alpha$ , which is complex, and then record the result at the point at which the sign of the complex part of alpha changes. This locates where the value of this complex term is approximately 0. We then plot the neutral curves for the half angle of 70 degrees for  $\alpha, \beta, k, \varepsilon$  in Figure 15. As seen in<sup>2</sup>, the quantities

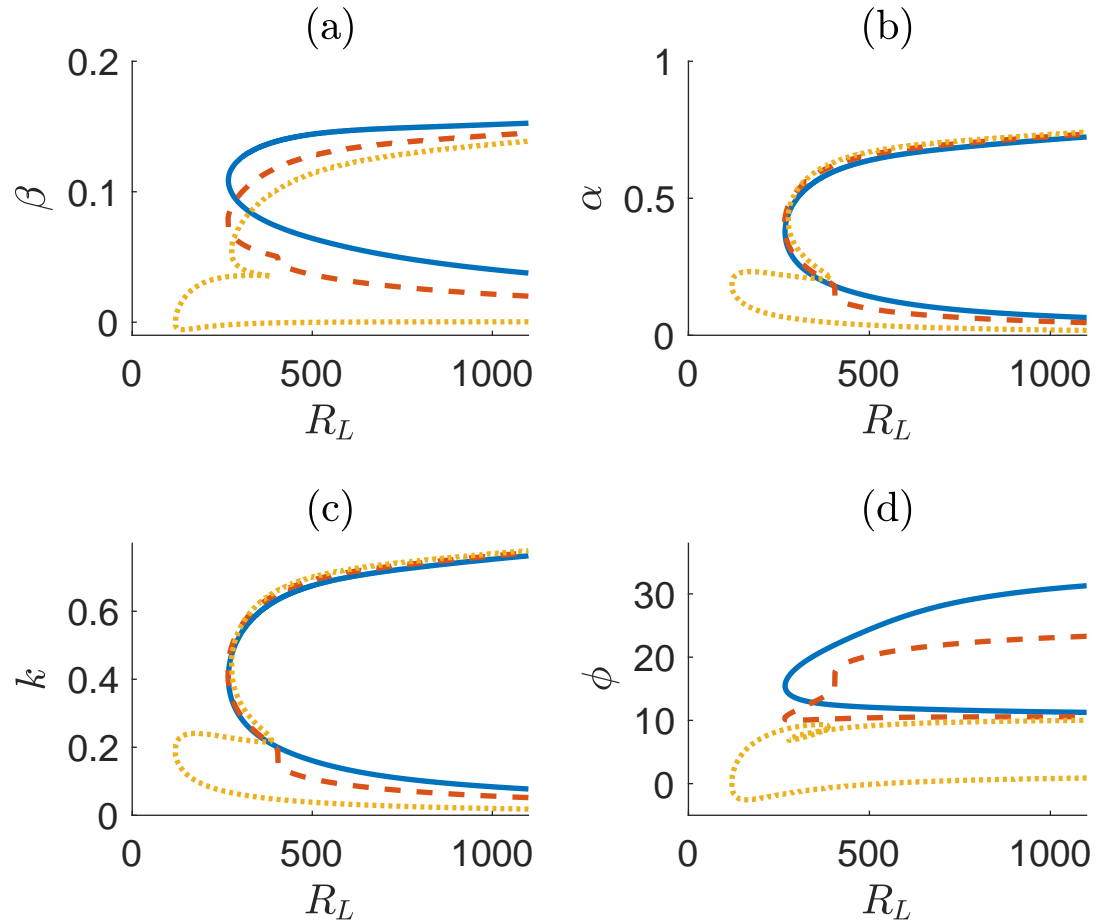


FIG. 15. Neutral stability curves for  $\omega = -5$  (solid),  $\omega = 0$  (dashed) and  $\omega = 4$  (dotted) for the case of  $\psi = 70^\circ$ . (a)  $R_L$  against  $\beta$  wavenumber, (b)  $R_L$  against  $\alpha_r$  wavenumber, (c)  $R_L$  against  $k$  wavenumber and (d)  $R_L$  against  $\phi$  waveangle

$\alpha$  and  $\beta$  are related by  $\alpha = \alpha_A (\sin \psi)^{1/2}$  and  $\beta = \beta_A / x (\sin \psi)^{1/2}$ , where  $\alpha_A, \beta_A$  are the asymptotic parameters as seen in Section III. This ensures the quantities  $k, \phi$  correspond to the asymptotic wavenumber ( $\gamma_\delta^*$ ) and waveangle ( $\phi$ ) respectively and are calculated using the Equations (70 and

71) respectively (which are the same as the Equations (5.1-5.2) in<sup>2</sup>):

$$k = \frac{(\alpha^2 + \beta^2)^{1/2}}{(\sin^2 \psi)^{1/2}}, \quad (70)$$

$$\phi = \arctan \left( \frac{\beta \sin \psi}{\alpha} \right). \quad (71)$$

We see from Figure 15 the negative and stationary frequency show similar behavior to the neutral curves shown in Figure 9 in<sup>3</sup> and Figure 5 in<sup>7</sup> (with a difference due to these studies being conducted on the case of  $\psi = 90$ ). However we see a difference in behavior for the frequency value of  $\omega = 4$  in both of the figures mentioned previously (though it is to be noted that the type II branch of both of these plots at these frequencies also have a slight difference in behavior). This difference is potentially due to the difference in solving algorithm used, and the way each algorithm calculates and orders the points around this low Reynolds number range. Though it is to be noted that this type II waveangle switching behavior is only present for high positive values (see Figure 19 for example of lower positive frequency values) both of these papers also observed this switching effect at frequency values of 4 and higher.

## VI. COMPARISON BETWEEN ASYMPTOTIC AND NUMERICAL SOLUTIONS

Care must be taken when comparing the results for the asymptotic and numerical methods in order to create consistent comparisons. First we must define the frequency  $\omega$  in terms of each normal mode expansions for the asymptotic method. This is why the frequency values for type I and type II are defined as shown in equations (46 and 48) respectively. Such definitions also limit the value of positive frequency that we can effectively study for type II due to the limit of asymptotic frequency shown in Figure 5. We also recall that the local Reynolds number defined in Section V A is equivalent to the boundary layer thickness scaled Reynolds number we use in the IV such that  $R_L = R_\delta^*$ . Also we are unable to compare the values of  $\alpha, \beta$  and  $n = \beta R_L$ , as for the asymptotic method, we cannot separate the wavenumber ( $\gamma_\delta^*$ ) and waveangle ( $\phi$ ) terms. So we can only compare the neutral curve results for the wavenumber and waveangle. Such comparisons are shown in Figures 16 and 17 respectively for the wavenumber and waveangle respectively. For these plots, the numerical result is halted at  $R_L = 10^5$  for the type I branch and at the point before destabilization for the type II branch. The type I branch was halted at  $R_L = 10^5$  due to destabilization occurring after this point, which has also been seen in the previous

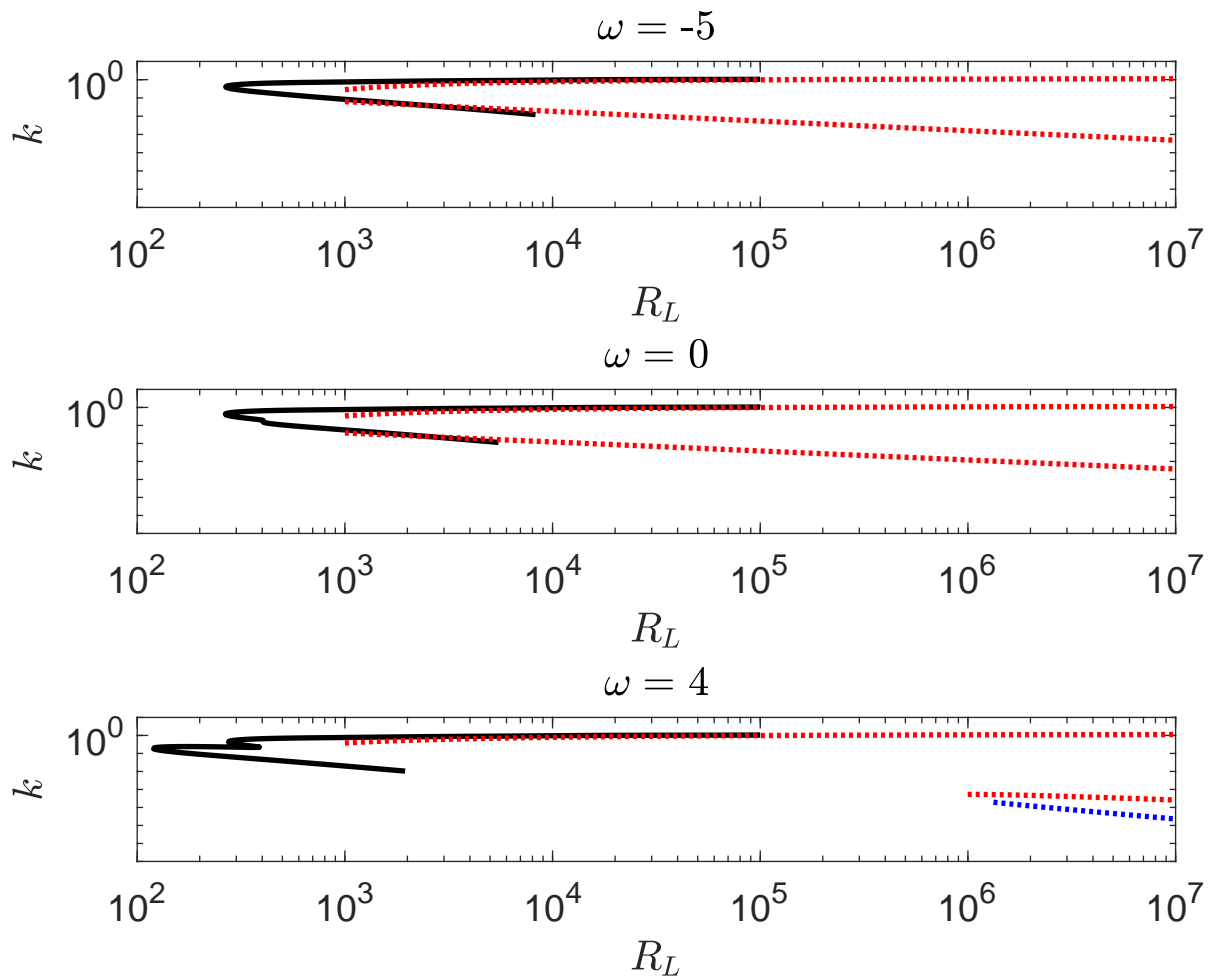


FIG. 16. Neutral stability curves for the wavenumber for  $\psi = 70^\circ$  with numerical solutions (solid line) and asymptotic solutions (dotted, red represents primary type I and type II solutions and blue represents the type II second branch solutions)

studies<sup>2,3</sup>. We see from Figure 16 that the numerical result for the type I wavenumber agrees well with the asymptotic solution as the Reynolds number values reach  $R_L = 10^5$ , whereas type II the results for  $\omega = -5$  and  $\omega = 0$  are reasonably close together from  $R_L = 10^3$  until the  $R_L$  value hits a few thousand, after which it crosses the asymptote and remains below it as it becomes close to the where the numerical result is halted. Unfortunately, due to the numerical code for type II destabilizing at this point, it is not clear whether this agreement will continue for the higher  $R_L$  values. Meanwhile for  $\omega = 4$  due to the asymptotic solution only existing from  $R_L =$

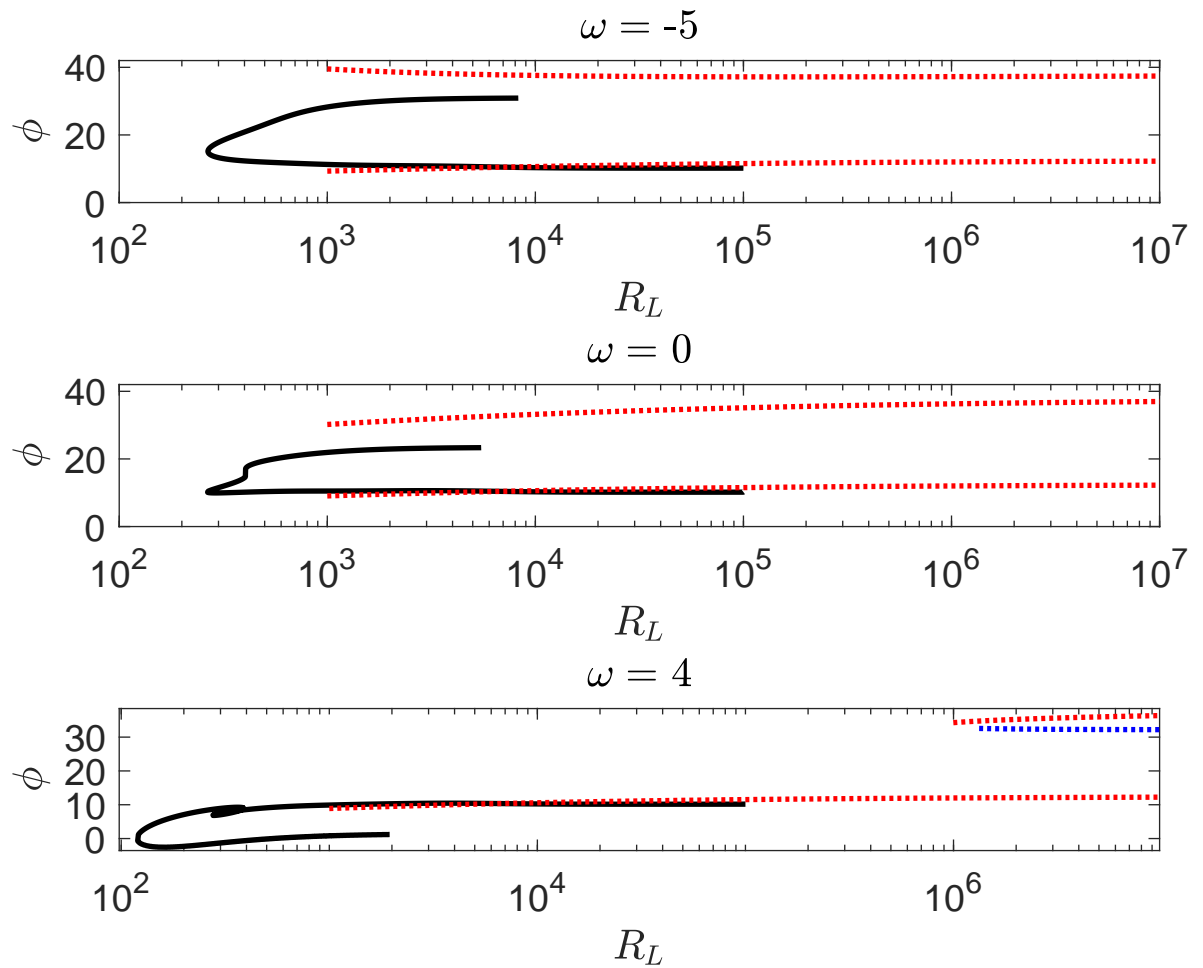


FIG. 17. Neutral stability curves for the waveangle for  $\psi = 70^\circ$  with numerical solutions (solid line) and asymptotic solutions (dotted, red represents primary type I and type II solutions and blue represents the type II second branch solutions)

$10^6$  on-wards, comparison is very difficult with the effect of the numerical destabilization for the type II branch occurring at approximately  $R_L = 1950$ . For Figure 17, however, we see that the numerical type I results for each frequency value agree well with the asymptotic solutions, with the agreement improving as the numerical solution approaches  $R_L = 10^4$ . But then from  $R_L = 10^4 - 10^5$ , the numerical solution, although remaining close, crosses the asymptote slightly. However, for the numerical type II modes, although for the frequency values  $\omega = -5$  and  $0$  the values are reasonably agreeable to the asymptotic solutions, we see that for  $\omega = 4$  that the asymptotic solution fails to replicate the effect of the numerical type II branch. The numerical type II waveangle

branch has now appeared at lower values than the type I branch, dropping to negative waveangle values between  $R_L = 10^2 - 10^3$ . This suggests that comparisons at such high frequency values, physically meaning that the waves are traveling much faster than the rotation speed of the surface of the cone, are not possible using this method(s). Because of this observation, we tested a further three positive frequency values of  $\omega = 0.5, 1.2$  and  $2$ . The neutral curves of the wavenumber and waveangle are shown in Figures 18 and 19 respectively. We see from Figure 18 that for the

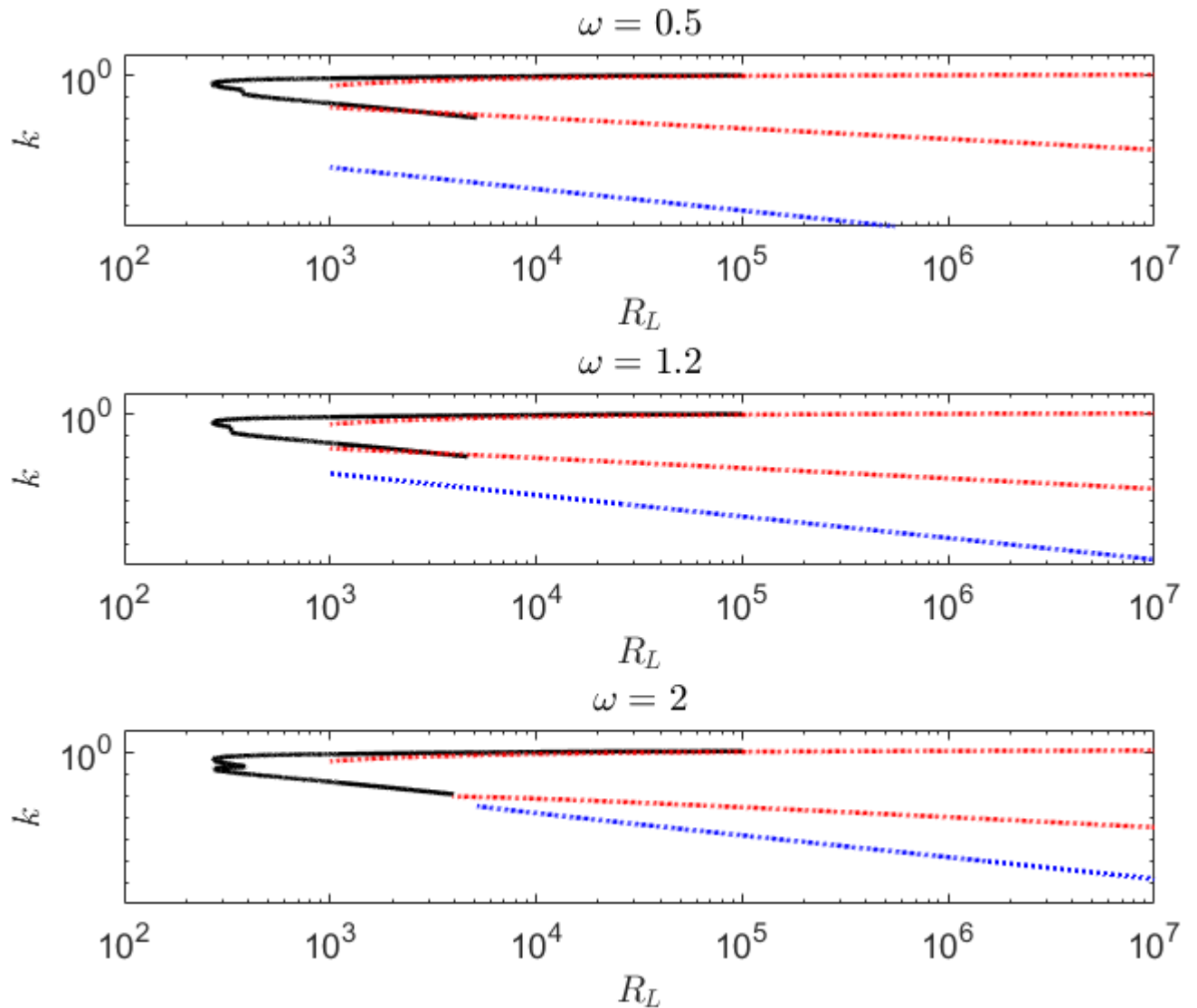


FIG. 18. Neutral stability curves for the wavenumber for  $\psi = 70^\circ$  with numerical solutions (solid line) and asymptotic solutions (dotted, red represents primary type I and type II solutions and blue represents the type II second solutions)

frequency value of  $\omega = 0.5$ , the agreement between the primary results is similar to that seen in

This is the author's peer reviewed, accepted manuscript. However, the online version of record will be different from this version once it has been copyedited and typeset.  
PLEASE CITE THIS ARTICLE AS DOI:10.1063/1.50033202

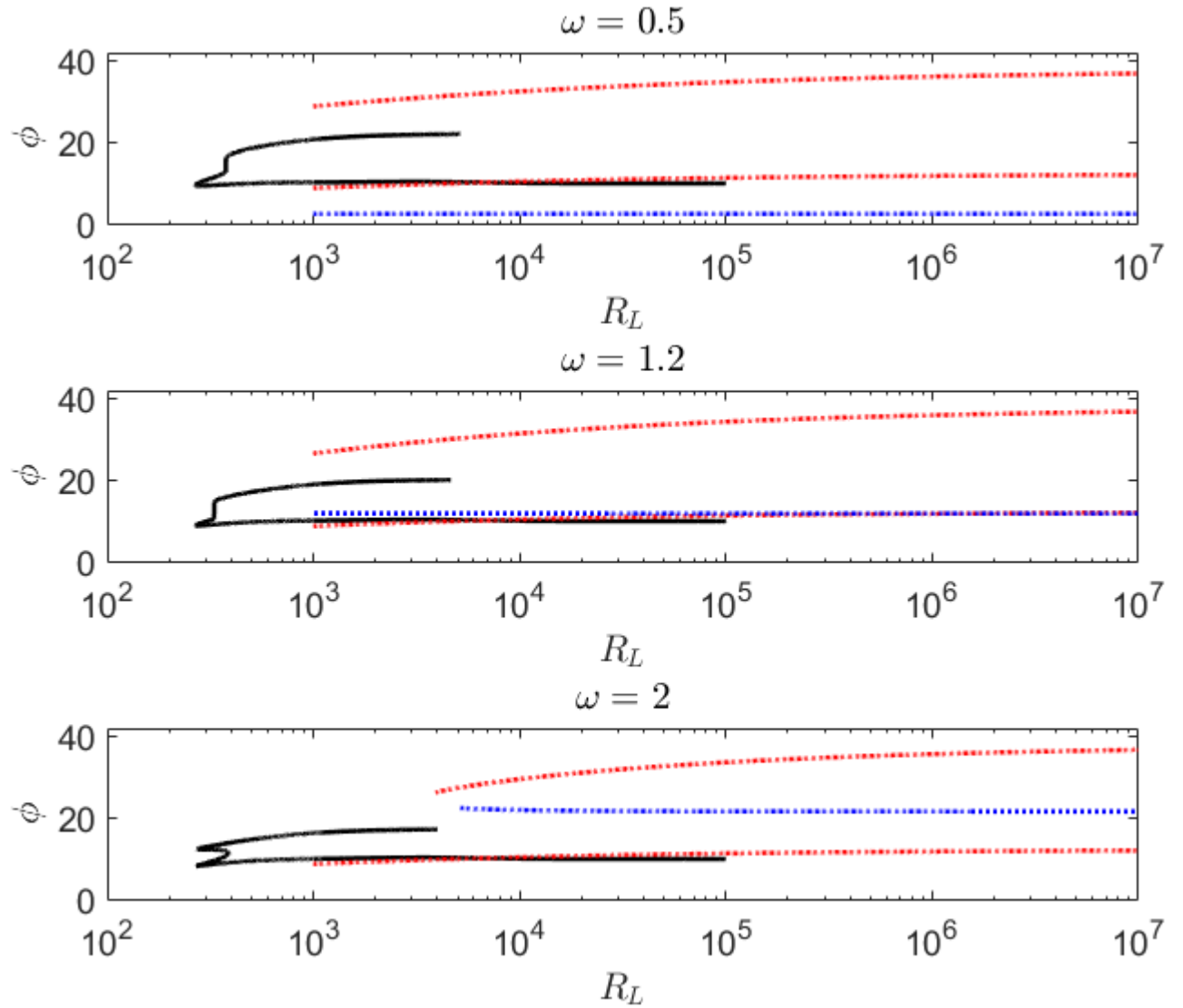


FIG. 19. Neutral stability curves for the waveangle for  $\psi = 70^\circ$  with numerical solutions (solid line) and asymptotic solutions (dotted, red represents primary type I and type II solutions and blue represents the type II second solutions)

Figure 16 for the frequency value of  $\omega = 0$ . For the frequency value of  $\omega = 1.2$ , we see that there is good agreement between the primary asymptotic and numerical solutions. However, in Figure 19, we see that the second asymptotic solution is almost completely aligned with the type I branch for the entire domain. We also see that for the frequency value of  $\omega = 2$ , the type I branch for both primary asymptotic and numerical agree well, whereas for the type II numerical and asymptotic solution, the numerical solution appears to agree more with the secondary asymptotic solution. Though this is inferred after the stopping point for  $\omega = 2$ , where the numerical solution beyond

this point destabilizes.

## VII. CRITICAL REYNOLDS NUMBER STUDY

We then performed a study on the effect of the frequency and half angle on the location of the type I critical Reynolds number. The critical Reynolds number is the location at which the type I mode is most dangerous, and the smallest Reynolds number in the type I branch that yields a neutral curve value (i.e it is the smallest Reynolds number value that has a sign change in the complex value of  $\alpha$ ). To study the effects of traveling modes and the half angle on the critical Reynolds number, we plot the critical Reynolds number for each half angle  $40^\circ - 90^\circ$  as the frequency varies in the range  $\omega = -5$  to  $4$ . The results of this are shown in Figure 20.

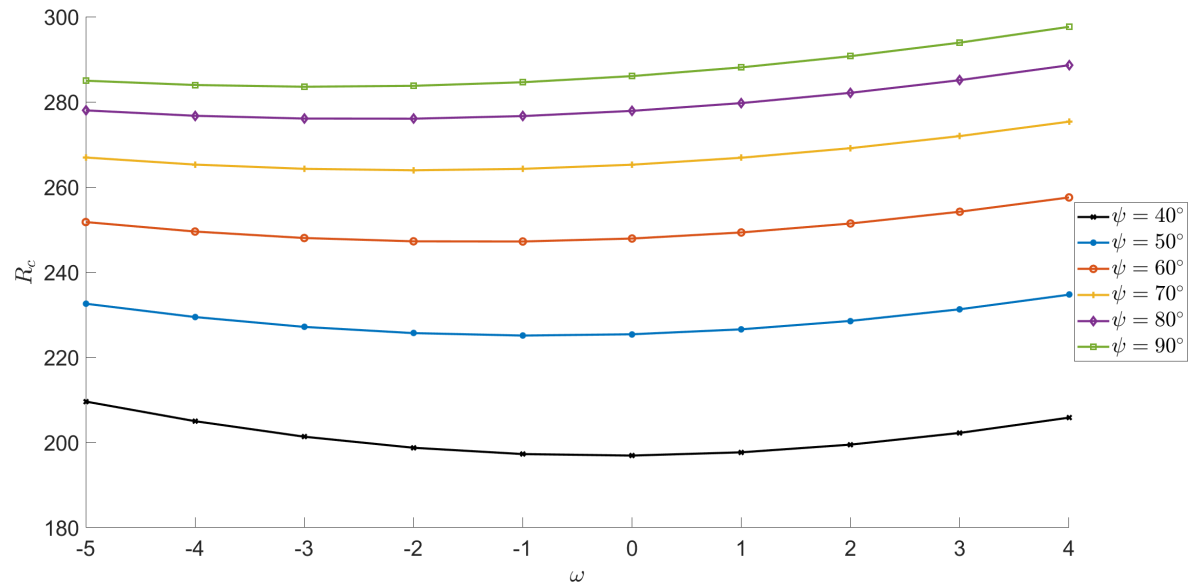


FIG. 20. Plot of the critical Reynolds number ( $R_c$ ) for each frequency ( $\omega$ ) for rotating cones with half angles between  $\psi = 40^\circ - 90^\circ$

We see from Figure 20 that the critical Reynolds number reduces as the half angle reduces for each frequency value. However, we see that for each half angle, there is a minima for the critical Reynolds number occurring for the negative frequency values. We will define the value of frequency at which the critical Reynolds number is the lowest for a particular value of the half angle ( $\psi$ ), as the critical frequency which we will represent as  $\omega_c$ . We now plot this critical frequency value for each half angle in Figure 21. We also show the values of the critical frequency for each half angle and the corresponding critical Reynolds number in Table III.

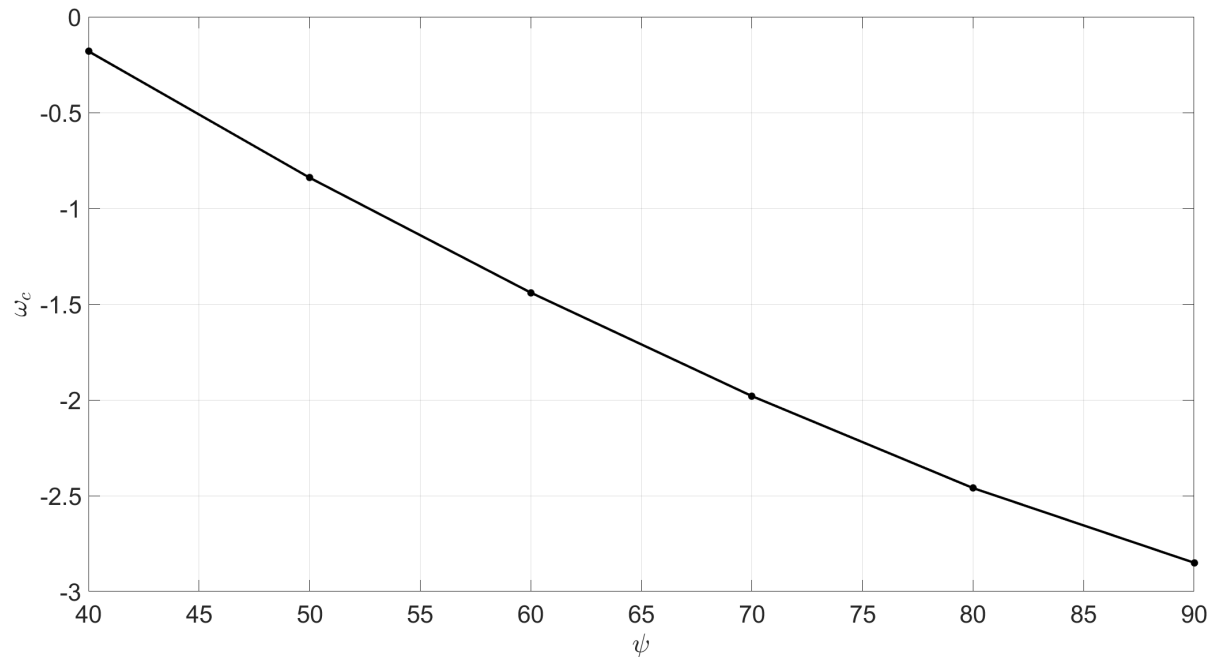


FIG. 21. Plot of the critical frequency values ( $\omega_c$ ) for each half angle  $\psi$  between  $40^\circ - 90^\circ$

$\psi$	$\omega_c$	$R_c$
$40^\circ$	-0.18	196.8924
$50^\circ$	-0.84	225.0902
$60^\circ$	-1.44	247.1184
$70^\circ$	-1.98	263.9246
$80^\circ$	-2.46	275.9818
$90^\circ$	-2.85	283.5423

TABLE III. Table showing the values of the critical frequency ( $\omega_c$ ) and the critical Reynolds number value ( $R_c$ ) at this frequency for each half ( $\psi$ ) angle in the cross-flow analysis regime

We see from both Figure 21 and Table III that as the half angle decreases, the critical frequency value increases. This shows that the most dangerous mode occurs at a faster frequency, as the half angle of the cone is decreased up to the boundary before the regime changes to the centrifugal mode. It is also seen that for the half angle of  $90^\circ$  (i.e the rotating disk case) the results agree well with the results obtained by Balakumar and Malik<sup>10</sup> who obtained the critical omega value of  $\omega_c = -2.9$  at the Reynolds number  $R_c = 283.6$  (referred to in that paper as the upper branch minimum). Though it is to be noted that this critical value always occurs for modes traveling

modes traveling slower than the speed of rotation of the cone for all half angles tested. Care should be taken to extend this range to the half angles  $0^\circ - 39^\circ$ , an interested reader is encouraged to read the following papers<sup>24-26</sup> to fully explore the justification of not including those half angles in this cross-flow analysis.

### VIII. ENERGY ANALYSIS

In order to further understand the mechanics at work in the system for changing the traveling mode frequency and half angle, we now perform an energy balance analysis. This method is similar to the energy analysis conducted by<sup>20,22</sup>, however, we will include the effects of the half angle. We conducted the analysis using the type I eigenfunctions at the position  $R_c + 200$ , which was chosen as it is a suitable distance in the unstable regime. Also this position facilitates clearer comparison between the results obtained for the rotating disk case<sup>22</sup>, however, with temperature dependent viscosity removed. We use the value of  $\alpha$  at this position, where the disturbance is most amplified such that the value of  $-\alpha_i$  is the maximum within the neutral curve. To perform the energy balance analysis, we follow Cooper and Carpenter<sup>20</sup> as well as Miller et al<sup>22</sup> by multiplying the momentum stability equations by their corresponding velocity component (the first momentum stability equation is multiplied by  $\hat{u}$ , the second equation  $\hat{v}$ , and the third equation  $\hat{w}$ ) and then they are summed together (whilst removing terms of  $R_L^{-2}$  and  $R_L^{-3}$  as these contributions are extremely small relative to the other terms) to get Equation 72.

$$\begin{aligned}
 & \hat{u} \frac{\partial \hat{u}}{\partial t} + \hat{v} \frac{\partial \hat{v}}{\partial t} + \hat{w} \frac{\partial \hat{w}}{\partial t} + U \left( \hat{u} \frac{\partial \hat{u}}{\partial x} + \hat{v} \frac{\partial \hat{v}}{\partial x} + \hat{w} \frac{\partial \hat{w}}{\partial x} \right) + \frac{V}{R_L} \left( \hat{u} \frac{\partial \hat{u}}{\partial \theta} + \hat{v} \frac{\partial \hat{v}}{\partial \theta} + \hat{w} \frac{\partial \hat{w}}{\partial \theta} \right) + \frac{W}{R_L} \left( \hat{u} \frac{\partial \hat{u}}{\partial \eta} + \hat{v} \frac{\partial \hat{v}}{\partial \eta} + \hat{w} \frac{\partial \hat{w}}{\partial \eta} \right) \\
 & + \hat{w} \hat{u} U' + \hat{w} \hat{v} V' + \frac{\hat{w}^2}{R_L} W' + \frac{\hat{u}^2 U \sin \psi}{R_L} - \frac{2\hat{v} \hat{u} V \sin \psi}{R_L} + \frac{\hat{v}^2 U \sin \psi}{R_L} + \frac{2\hat{v} \hat{u} V \sin \psi}{R_L} + \frac{2\hat{v} \hat{w} V \cos \psi}{R_L} - \frac{2\hat{v} \hat{w} V \cos \psi}{R_L} \\
 & = -\hat{u} \frac{\partial \hat{p}}{\partial x} - \frac{1}{R_L} \hat{v} \frac{\partial \hat{p}}{\partial \theta} - \hat{w} \frac{\partial \hat{p}}{\partial \eta} + \frac{1}{R_L} \left( \hat{u}_j \frac{\partial \sigma_{ij}}{\partial x_i} \right). \tag{72}
 \end{aligned}$$

Where  $\hat{u}_j = \hat{u}, \hat{v}, \hat{w}$  and  $\sigma_{ij}$  represents the viscous stress terms given as:

$$\begin{aligned}
 \sigma_{11} &= \frac{\partial \hat{u}}{\partial x}, & \sigma_{12} &= \frac{1}{R} \frac{\partial \hat{u}}{\partial \theta}, & \sigma_{13} &= \frac{\partial \hat{u}}{\partial z}, \\
 \sigma_{21} &= \frac{\partial \hat{v}}{\partial x}, & \sigma_{22} &= \frac{1}{R} \frac{\partial \hat{v}}{\partial \theta}, & \sigma_{23} &= \frac{\partial \hat{v}}{\partial z}, \\
 \sigma_{31} &= \frac{\partial \hat{w}}{\partial x}, & \sigma_{32} &= \frac{1}{R} \frac{\partial \hat{w}}{\partial \theta}, & \sigma_{33} &= \frac{\partial \hat{w}}{\partial z}. \tag{73}
 \end{aligned}$$

If we introduce a new variable  $\hat{e} = 1/2 (\hat{u}^2 + \hat{v}^2 + \hat{w}^2)$  and average the equation over a single time period and azimuthal mode, which removes all derivative terms of  $\theta$  and  $t$ , whilst rearranging to

get the  $x$  derivative terms on the left hand side. This leads to the energy contribution equation as:

$$\frac{\partial E}{\partial x} = \left\{ \int_0^\infty -\langle \hat{w}\hat{u} \rangle U' - \langle \hat{w}\hat{v} \rangle V' - \frac{\langle \hat{w}^2 \rangle}{R_L} W' d\eta \right\}^{EPRS} - \frac{1}{R_L} \left\{ \int_0^\infty \left\langle \sigma_{ij} \frac{\partial \hat{u}_j}{\partial x_i} \right\rangle d\eta \right\}^{EDV} - \frac{1}{R_L} \left\{ \int_0^\infty \langle \hat{p} (\hat{u} \sin \psi + \hat{w} \cos \psi) \rangle d\eta \right\}^{PW} - \frac{1}{R_L} \left\{ \int_0^\infty (\langle \hat{u}^2 \rangle + \langle \hat{v}^2 \rangle) U \sin \psi - \langle \hat{e} \rangle W' d\eta \right\}^{SC}. \quad (74)$$

Where the value of  $E$  is given by:

$$E = \int_0^\infty \langle U\hat{e} \rangle + \langle \hat{u}\hat{p} \rangle - \frac{1}{R_L} (\langle \hat{u}\sigma_{11} \rangle + \langle \hat{v}\sigma_{12} \rangle + \langle \hat{w}\sigma_{13} \rangle) d\eta. \quad (75)$$

The terms in equation (75) are: Energy Production due to Reynolds Stresses (EPRS), Energy Dissipation due to Viscosity (EDV), Pressure Work (PW) and Streamline Curvature (SC), and are consistent with the terms obtained by<sup>20,22</sup> when  $\psi = 90^\circ$ . The time averaged quantities have the form  $\langle xy \rangle = x^*y + xy^*$ , where the  $x^*$  represents the complex conjugate of  $x$ . The perturbations retain normal form so we can express the derivatives as  $\frac{\partial \hat{u}}{\partial x} = -2\alpha i \hat{u} \sin \psi$ ,  $\frac{\partial \hat{u}}{\partial z} = \hat{u}'$ .

### A. Energy Analysis Results

We then solve equation 74 using numerical integration using the values obtained by the solution of the eigenfunctions. For this energy analysis, we must study two separate cases. The first case studies the effects of the changing half angle on the energy balance terms. And the second case studies the effect of changing the traveling mode frequency for a fixed half angle for the cone. Due to the difference in normalization of the eigenfunctions for these two distinct cases, it is not possible to compare the effects of these two cases. We initiate the first case by solving equation (74), setting the frequency value to  $\omega = 0$ . This to observe the effects of the half angle on the energy contribution. The results of this analysis are presented as the contribution of the combined terms which are shown in Figure 22.

We see from Figure 22 that we can simplify the energy balance equation to remove the negligible contribution terms (PW and SC), and then normalize with respect to the factor E to get:

$$\{ -2\alpha_i \sin \psi \}^{TME} \approx \left\{ \int_0^\infty V' \langle \hat{w}\hat{v} \rangle \right\}^{EPRS} - \left\{ \frac{1}{R_L} \int_0^\infty \left\langle \sigma_{ij} \frac{\partial \hat{u}_j}{\partial x_j} \right\rangle \right\}^{EDV}. \quad (76)$$

This is the same simplification as made by<sup>22</sup> for the rotating disk (i.e when  $\psi = 90^\circ$ ). This shows that for the half angle range of  $\psi = 40^\circ - 90^\circ$ , this simplification is valid. We see from Figure 22,

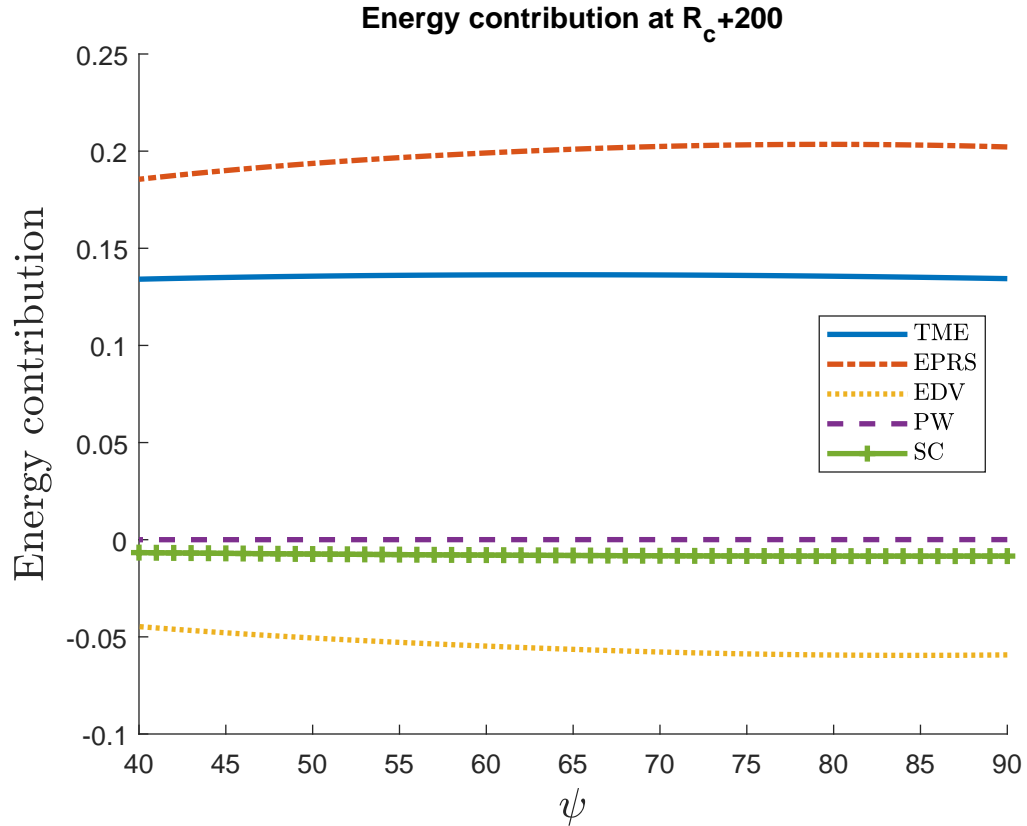


FIG. 22. Plot of the energy contribution of the energy terms: TME (Total Mechanical Energy), EPRS (Energy Production due to Reynolds Stresses), EDV (Energy Dissipation due to Viscosity), PW (Pressure Work) and SC (Streamline Curvature) for each half angle  $\psi = 40^\circ - 90^\circ$  with travelling mode frequency of  $\omega = 0$  (i.e the stationary mode case)

that the trend of EPRS and EDV is that as the half angle reduces, the energy contributed by these terms reduces in magnitude. Though it is to be noted that for EPRS and TME, the contribution slightly increase as the half angle reduces in the range of  $90^\circ - 70^\circ$ . Suggesting that the maximum values of EPRS and TME occur around  $70^\circ$ . Next we look at the second case, where we study the effect of changing the frequency for a particular half angle on the energy balance equation. In this case we have chosen to fix  $\psi = 70^\circ$ . The results of this analysis are shown in Figure 23

This plot shows once again, that the simplification of removing PW and SC, shown in equation 76 is once again true for all of the frequency values between  $\omega = -5$  and  $\omega = 4$ . We see that as the frequency increases, the total mechanical energy of the system reduces. This is caused by the EPRS term reducing at a stronger magnitude than the increase of the EDV term as the frequency value increases. We theorise that the reduction in the total mechanical energy of the disturbance as

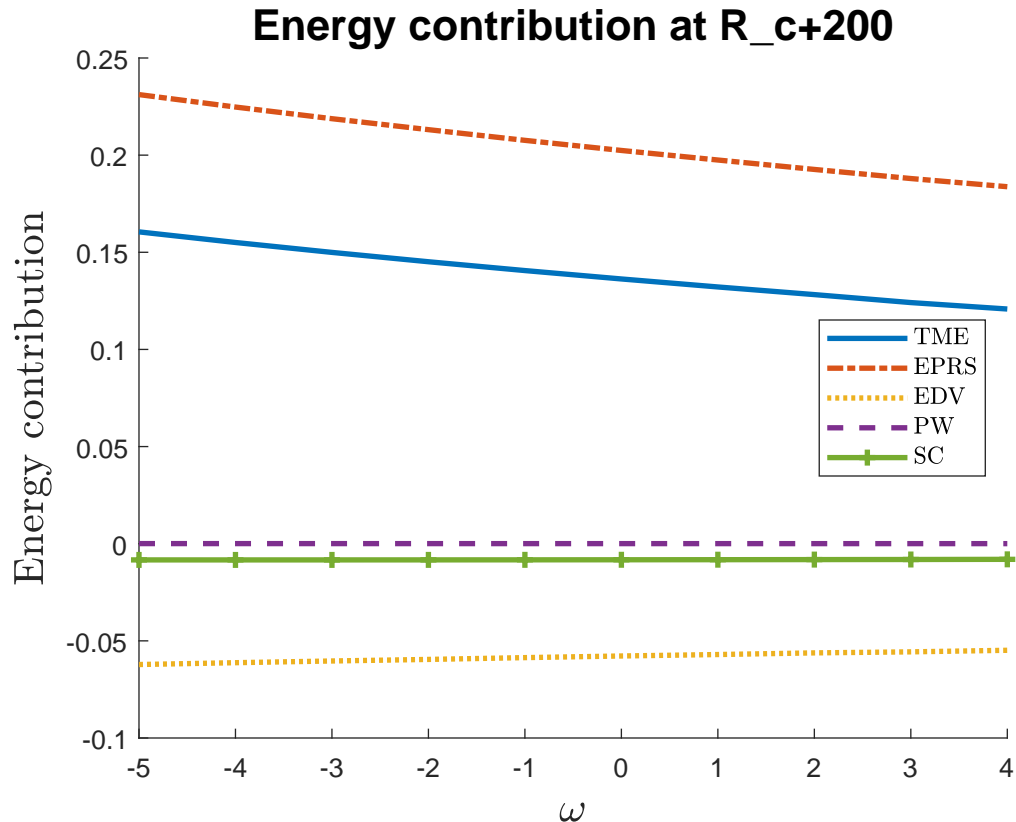


FIG. 23. Plot of the energy contribution of the energy terms: TME (Total Mechanical Energy), EPRS (Energy Production due to Reynolds Stresses), EDV (Energy Dissipation due to Viscosity), PW (Pressure Work) and SC (Streamline Curvature) for each frequency between  $\omega = -5$  and  $\omega = 4$  for a rotating cone with half angle  $70^\circ$

the frequency increases, shows that the energy in the system is being used to accelerate the speed of the waves relative to the speed of the rotation of the surface of the cone.

## IX. CONCLUSIONS

In this paper, we have first covered using an asymptotic and numerical method to evaluate the type I and type II modes for a rotating broad cone in still fluid, with traveling modes as well as the comparisons between the results of each method. The conclusion of this study is that although increasing the traveling wave frequency destabilizes the flow around a rotating cone, the stabilizing effect of increasing the half angle of said cone dominates the system for the type I modes. However, for type II modes, the effect of the traveling mode frequency dominates the

system. We also saw that for our numerical study, the results for the type II branch destabilized much sooner than the numerical results for the type I branch. This made it very difficult to obtain comparisons for the type II branch between the asymptotic and numerical methods. Further work is recommended to look at resolving this issue with the current formulation presented, and we are looking at applying navier-slip boundary conditions to the type II branch in future studies, which may lead to a resolution to this issue. In practical applications, for larger half angles and for when the waves are traveling slower than the rotating cone would render the flow over a spinning nose rotor more stable. This would result in a smoother intake of airflow into the turbofan core by delaying the onset of turbulence. This confirms the observation made in<sup>19</sup> which recommended that slower traveling vortices should be selected for when the type I instability dominates. For the presence of the second branch for the type II analysis, it is unknown whether this second branch solution is a physically valid new mode or whether it is an extra (non-physical) solution caused by the scalings used in the triple deck analysis to obtain the type II solution. Though it is noted that current experimental studies on the boundary layer of a rotating cone have rarely seen the effects of the type II modes physically due to the dominant effect of the type I modes as well as the type II mode occurring very close to the wall of the cone in a small area. Further work should be done to find an experimental method that can capture the type II modes for the cone to see if this second branch appears physically. Though the behavior of this second type II branch when compared to the numerical type II solution for various positive frequencies suggest that it is more likely to be a non-physical solution but this observation still needs to be validated with results experimentally.

We have also studied the effect of both the frequency and the half angle on the type I critical Reynolds number. We saw that for each half angle, there was a minima in the critical Reynolds number, which we defined as the critical frequency. This critical frequency value can be interpreted as the point of most interest where the most dangerous mode exists for each half angle. These critical frequency values are recommended to be used for the purpose of a guide for which experiments should be conducted to locate the most dangerous modes when looking at broad rotating cones in still fluid. It is to be noted that the critical frequency values are always negative (meaning that the modes are traveling slower than the rotation of the cone) in our current range of broad cone half angles.

For the energy analysis part, we studied the contribution of the energy balance terms for two distinct cases. It is important to note that a direct comparison between the changing of the half angle case and the effect of changing the traveling mode frequency case is not possible, as the

eigenfunctions for these distinct cases are normalized independently. For the stationary mode energy analysis, of which we studied the effect of changing the half angle on the energy budget, we observe that the Total Mechanical Energy (TME) exchanged between the base flow and the perturbation quantities as the half angle changes remains mostly stable (where the TME slightly increases between  $90^\circ - 70^\circ$  and reduces slightly between  $70^\circ - 40^\circ$ ). This shows that the energy exchange is only slightly affected by the change in half angle for the broad cone half angle values. We analyzed the effects of the changing frequency on a cone with a fixed half angle of  $70^\circ$ . We saw that as expected the total mechanical energy exchanged between the base flow and the perturbation quantities reduces as the frequency increases i.e as the traveling modes speed up in relation to the rotation speed of the cone, the energy exchanged reduces. This implies that the energy is being used to accelerate the traveling modes relative to the speed of the cone, which results in less total energy exchange as the frequency increases. It is recommended that further work should be done on increasing the accuracy of this model by considering adding axial flow to the system, which would model the effects of the speed of the airflow on the stability of the flow around the rotating cone with traveling modes. This will provide a more physically accurate model of a turbofan engine with an oncoming flow, and determine its effects on the critical Reynolds number, critical frequency and the energy balance equations. As well as this, our model only considers the effects for a broad cone, so the effect of traveling modes on the centrifugal mode present for a slender cone should also be investigated. As these models of the slender cone can be used to model the effects of traveling modes being present on a spinning projectile. After which comparisons could be made between the neutral curves, critical Reynolds and frequency values as well as the energy balance terms for both cross flow and centrifugal schemes for the half angles where both centrifugal and cross flow modes are theorized to exist  $50^\circ - 40^\circ$  which was mentioned in the paper<sup>25</sup>.

#### DATA AVAILABILITY STATEMENT

The data that support the findings of this study are available from the corresponding author upon reasonable request.

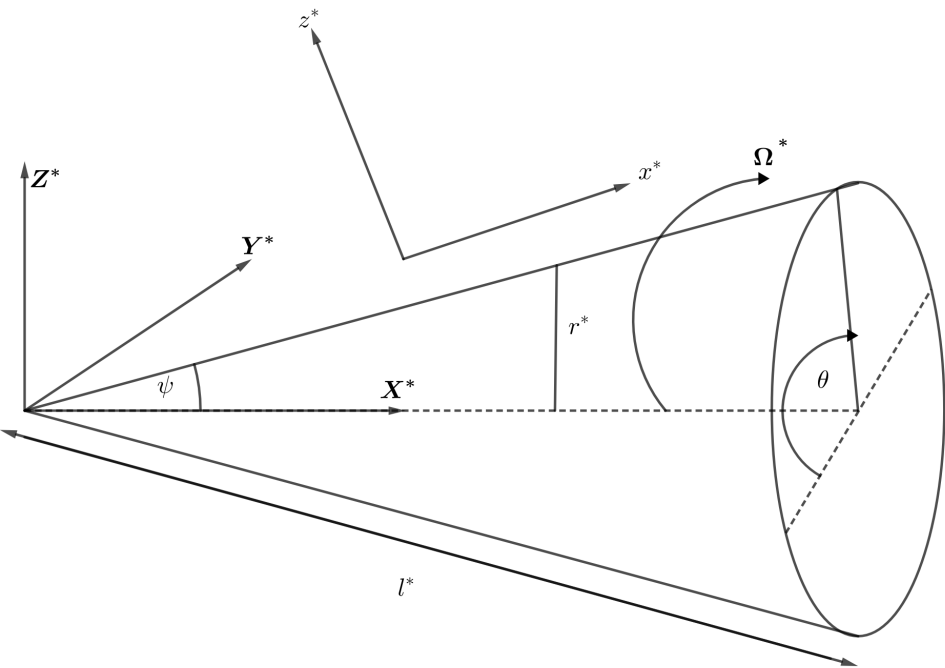
#### ACKNOWLEDGMENTS

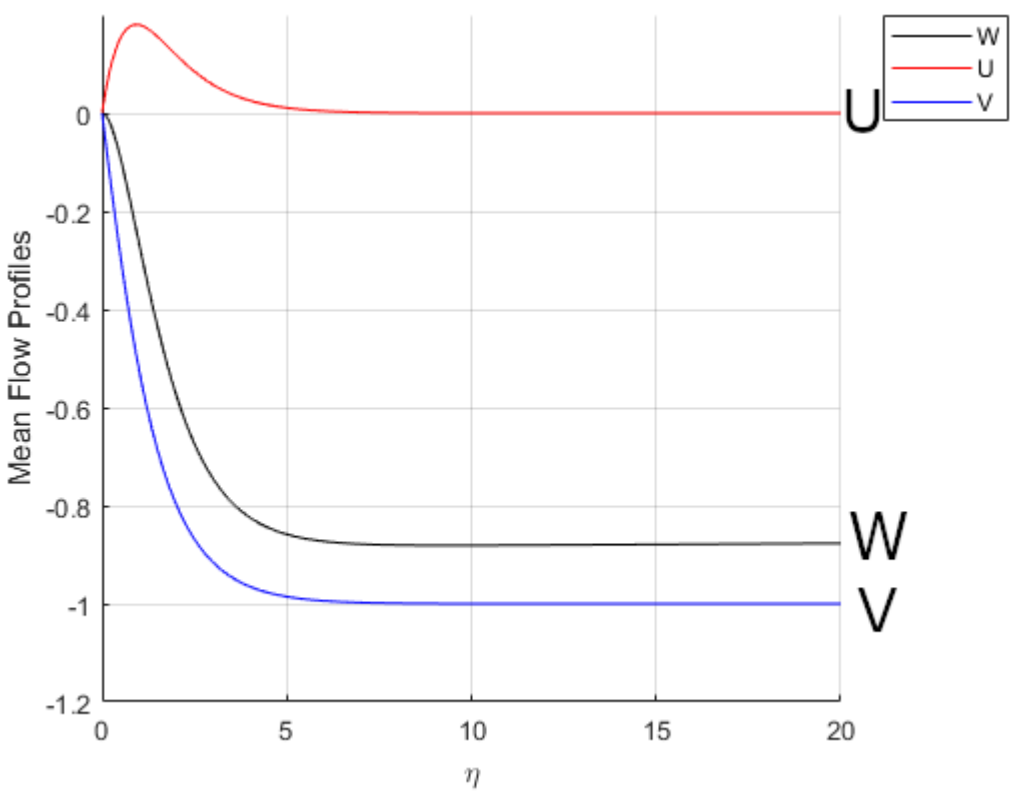
The authors wish to acknowledge support from the UKRI EPSRC grant (EP/R028699/1).

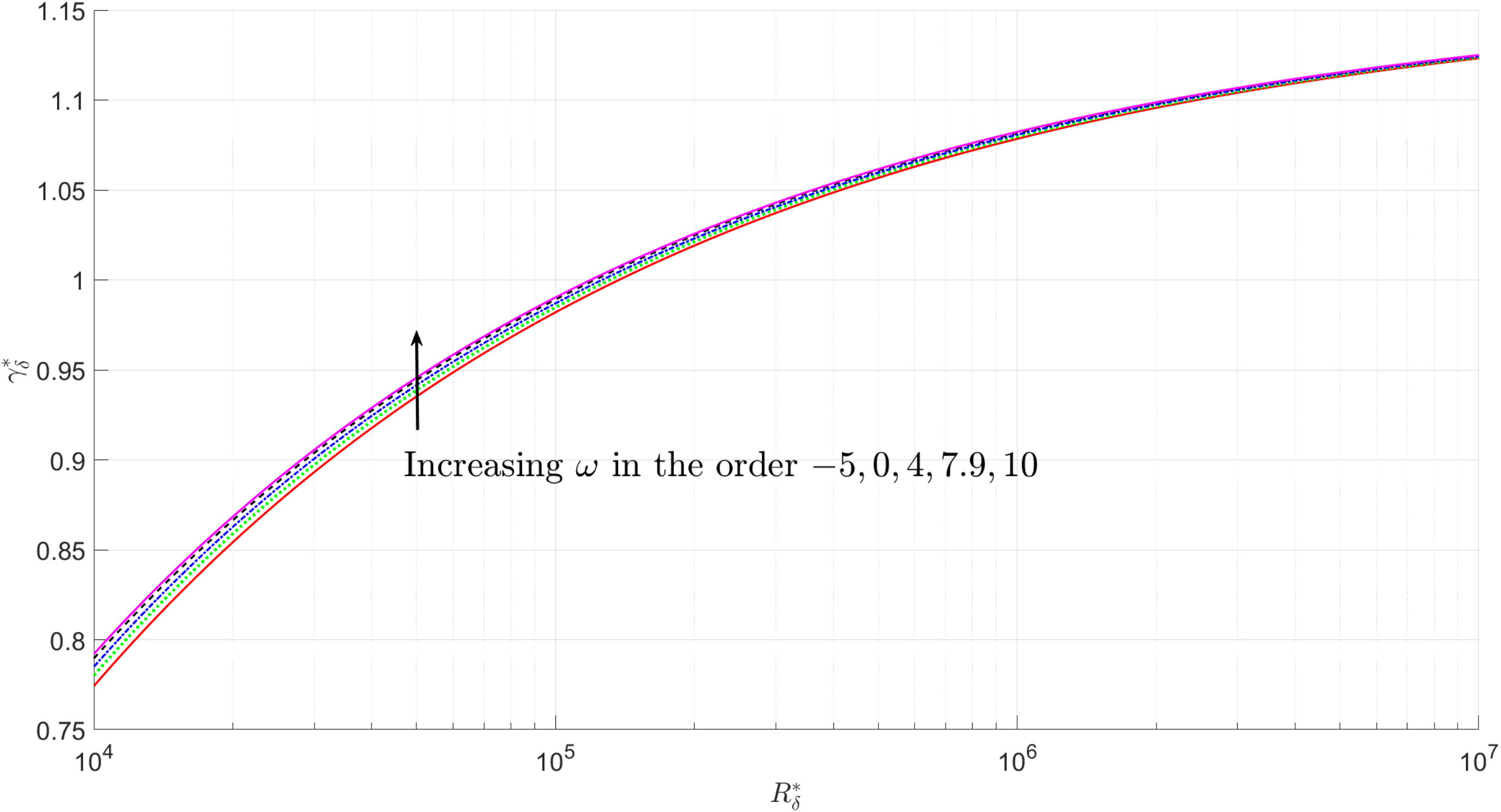
## REFERENCES

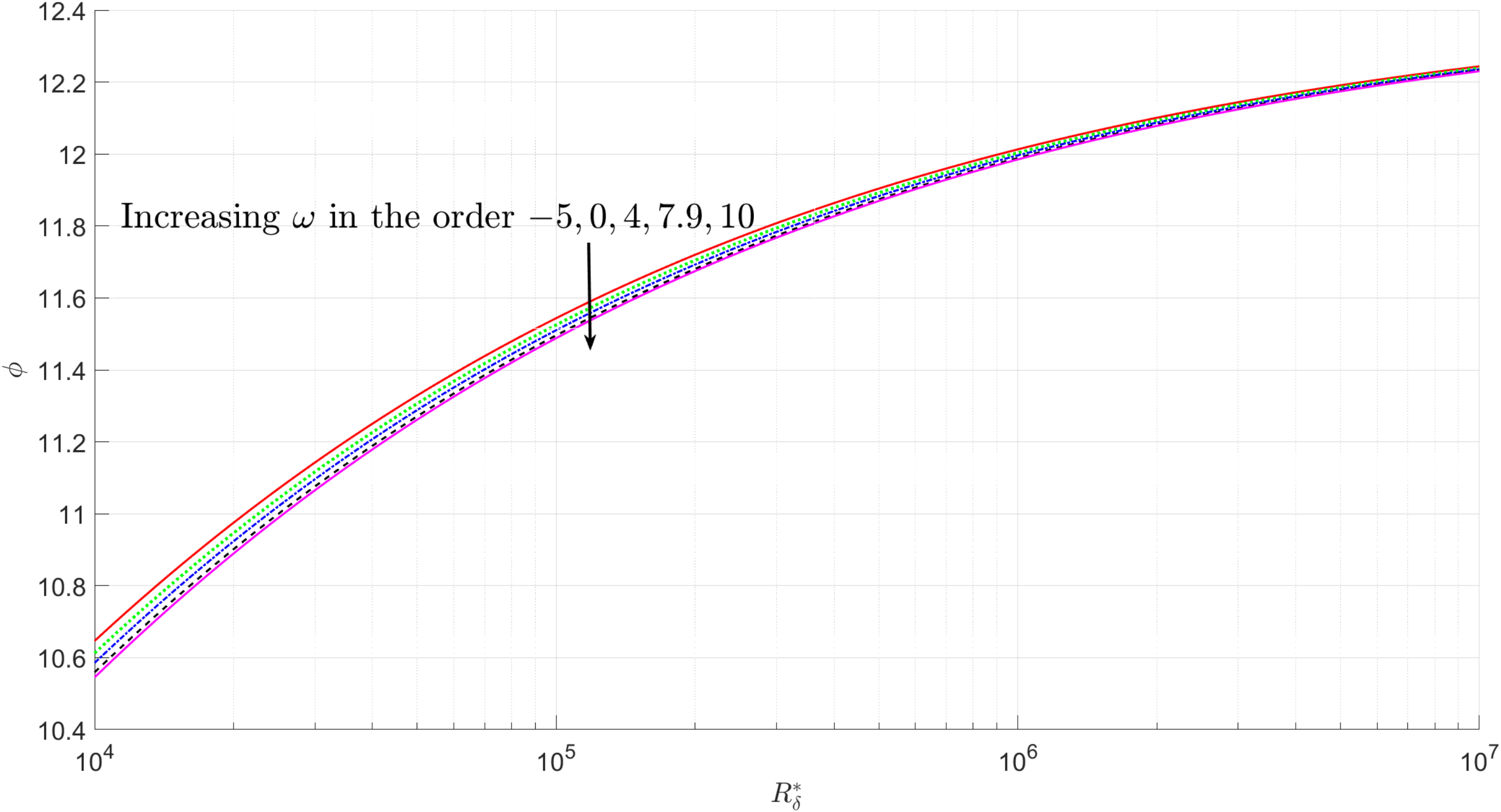
- <sup>1</sup>M. Turkyilmazoglu, “Convective and absolute instabilities in the incompressible boundary layer on a rotating disk,” *Hacettepe Journal of Mathematics and Statistics* **35**, 117–146 (2006).
- <sup>2</sup>S. J. Garrett, Z. Hussain, and S. Stephen, “The cross-flow instability of the boundary layer on a rotating cone,” *Journal of Fluid Mechanics* **622**, 209–232 (2009).
- <sup>3</sup>Z. Hussain, S. J. Garrett, and S. Stephen, “The instability of the boundary layer over a disk rotating in an enforced axial flow,” *Physics of Fluids* **23**, 114–108 (2011).
- <sup>4</sup>L. Mack, “The wave pattern produced by a point source on a rotating disk,” in *23rd Aerospace Sciences Meeting* (1985) p. 490.
- <sup>5</sup>R. Lingwood, “An experimental study of absolute instability of the rotating-disk boundary-layer flow,” *Journal of Fluid Mechanics* **314**, 373–405 (1996).
- <sup>6</sup>B. Fedorov, G. Plavnik, I. Prokhorov, and L. Zhukhovitskii, “Transitional flow conditions on a rotating disk,” *Journal of Engineering Physics and Thermophysics* **31**, 1448–1453 (1976).
- <sup>7</sup>M. Turkyilmazoglu and J. Gajjar, “Absolute and convective instability in the incompressible boundary layer on a rotating disk report no,” CLSCM (University of Manchester) (1998).
- <sup>8</sup>M. R. Malik, “The neutral curve for stationary disturbances in rotating-disk flow,” *Journal of Fluid Mechanics* **164**, 275–287 (1986).
- <sup>9</sup>P. Hall, “An asymptotic investigation of the stationary modes of instability of the boundary layer on a rotating disc,” *Proceedings of the Royal Society of London. A. Mathematical and Physical Sciences* **406**, 93–106 (1986).
- <sup>10</sup>P. Balakumar and M. Malik, “Traveling disturbances in rotating-disk flow,” *Theoretical and Computational Fluid Dynamics* **2**, 125–137 (1990).
- <sup>11</sup>M. Turkyilmazoglu, “Non-linear and non-stationary modes of the lower branch of the incompressible boundary layer flow due to a rotating disk,” *Quarterly of applied mathematics* **65**, 43–68 (2007).
- <sup>12</sup>Z. Hussain, *Stability and transition of three-dimensional rotating boundary layers*, Ph.D. thesis, University of Birmingham (2010).
- <sup>13</sup>R. Kobayashi and H. Izumi, “Boundary-layer transition on a rotating cone in still fluid,” *Journal of Fluid Mechanics* **127**, 353–364 (1983).
- <sup>14</sup>K. Kato, P. H. Alfredsson, and R. Lingwood, “Boundary-layer transition over a rotating broad cone,” *Physical Review Fluids* **4**, 071902 (2019).

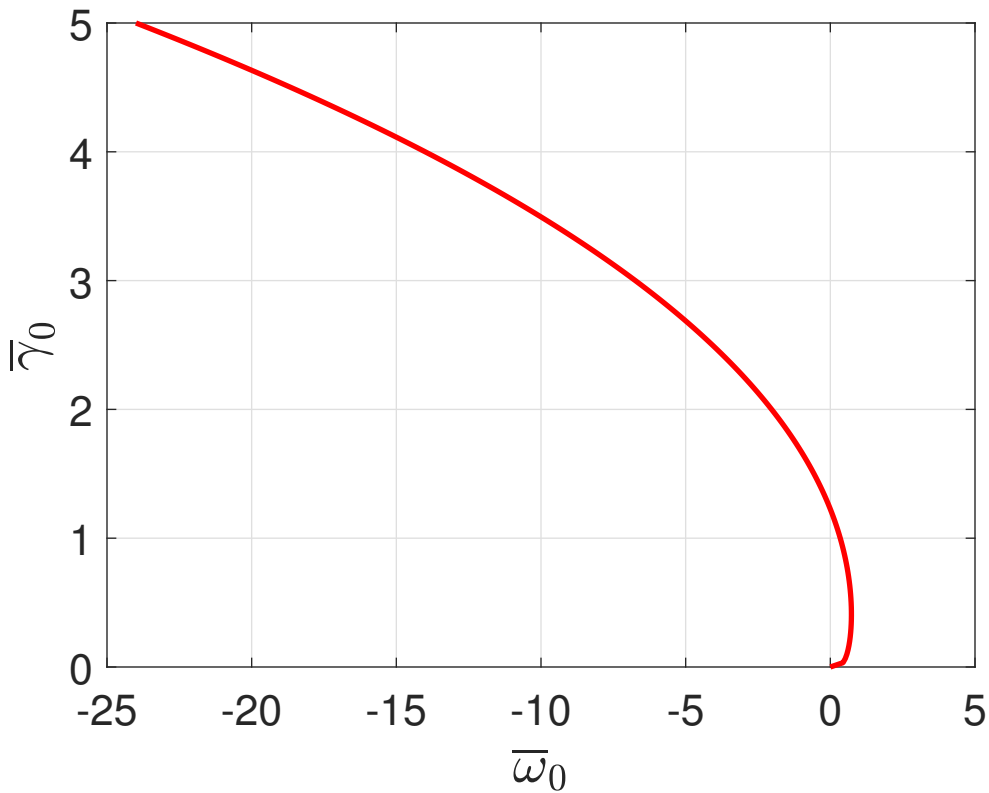
- <sup>15</sup>S. Tambe, F. Schrijer, A. G. Rao, and L. Veldhuis, “Coherent vortex structures over a rotating spinner under non-axial inflows at low Reynolds number,” in *54th 3AF International Conference on Applied Aerodynamics* (2019).
- <sup>16</sup>S. Tambe, F. Schrijer, A. G. Rao, and L. Veldhuis, “An experimental method to investigate coherent spiral vortices in the boundary layer over rotating bodies of revolution,” *Experiments in Fluids* **60**, 115 (2019).
- <sup>17</sup>S. Garrett and N. Peake, “The absolute instability of the boundary layer on a rotating cone,” *European Journal of Mechanics-B/Fluids* **26**, 344–353 (2007).
- <sup>18</sup>C. Thomas and C. Davies, “Global linear instability of rotating-cone boundary layers in a quiescent medium,” *Physical Review Fluids* **4**, 043902 (2019).
- <sup>19</sup>S. Garrett, “Linear growth rates of types 1 and 2 convective modes within the rotating-cone boundary layer,” *Fluid dynamics research* **42**, 025504 (2009).
- <sup>20</sup>A. Cooper and P. W. Carpenter, “The stability of rotating-disc boundary-layer flow over a compliant wall. part 1. type 1 and 2 instabilities,” *Journal of Fluid Mechanics* **350**, 231–259 (1997).
- <sup>21</sup>A. Cooper, J. Harris, S. J. Garrett, M. Özkan, and P. Thomas, “The effect of anisotropic and isotropic roughness on the convective stability of the rotating disk boundary layer,” *Physics of Fluids* **27**, 014107 (2015).
- <sup>22</sup>R. Miller, P. Griffiths, Z. Hussain, and S. Garrett, “On the stability of a heated rotating-disk boundary layer in a temperature-dependent viscosity fluid,” *Physics of Fluids* **32**, 024105 (2020).
- <sup>23</sup>M. Abramowitz and I. A. Stegun, *Handbook of mathematical functions: with formulas, graphs, and mathematical tables*, Vol. 55 (Courier Corporation, 1965).
- <sup>24</sup>Z. Hussain, S. Stephen, and S. J. Garrett, “The centrifugal instability of a slender rotating cone,” *Journal of Algorithms & Computational Technology* **6**, 113–128 (2012).
- <sup>25</sup>Z. Hussain, S. J. Garrett, and S. Stephen, “The centrifugal instability of the boundary-layer flow over slender rotating cones,” *Journal of Fluid Mechanics* **755**, 274–293 (2014).
- <sup>26</sup>Z. Hussain, S. J. Garrett, S. Stephen, and P. T. Griffiths, “The centrifugal instability of the boundary-layer flow over a slender rotating cone in an enforced axial free stream,” *Journal of Fluid Mechanics* **788**, 70–94 (2016).

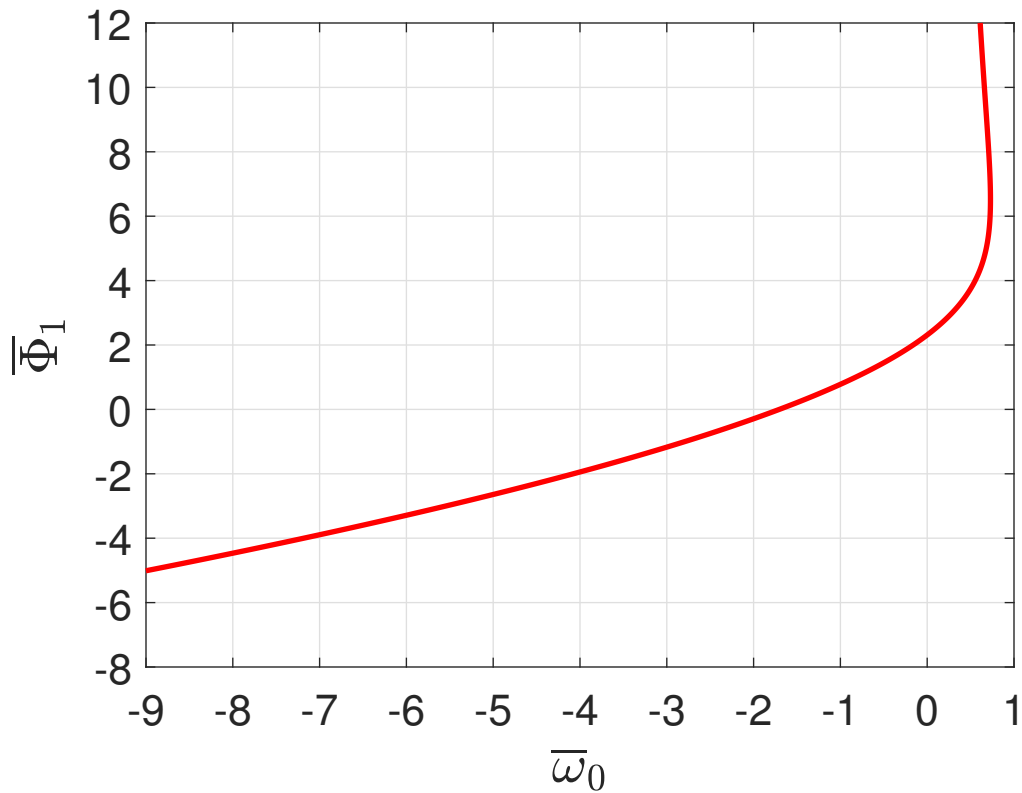


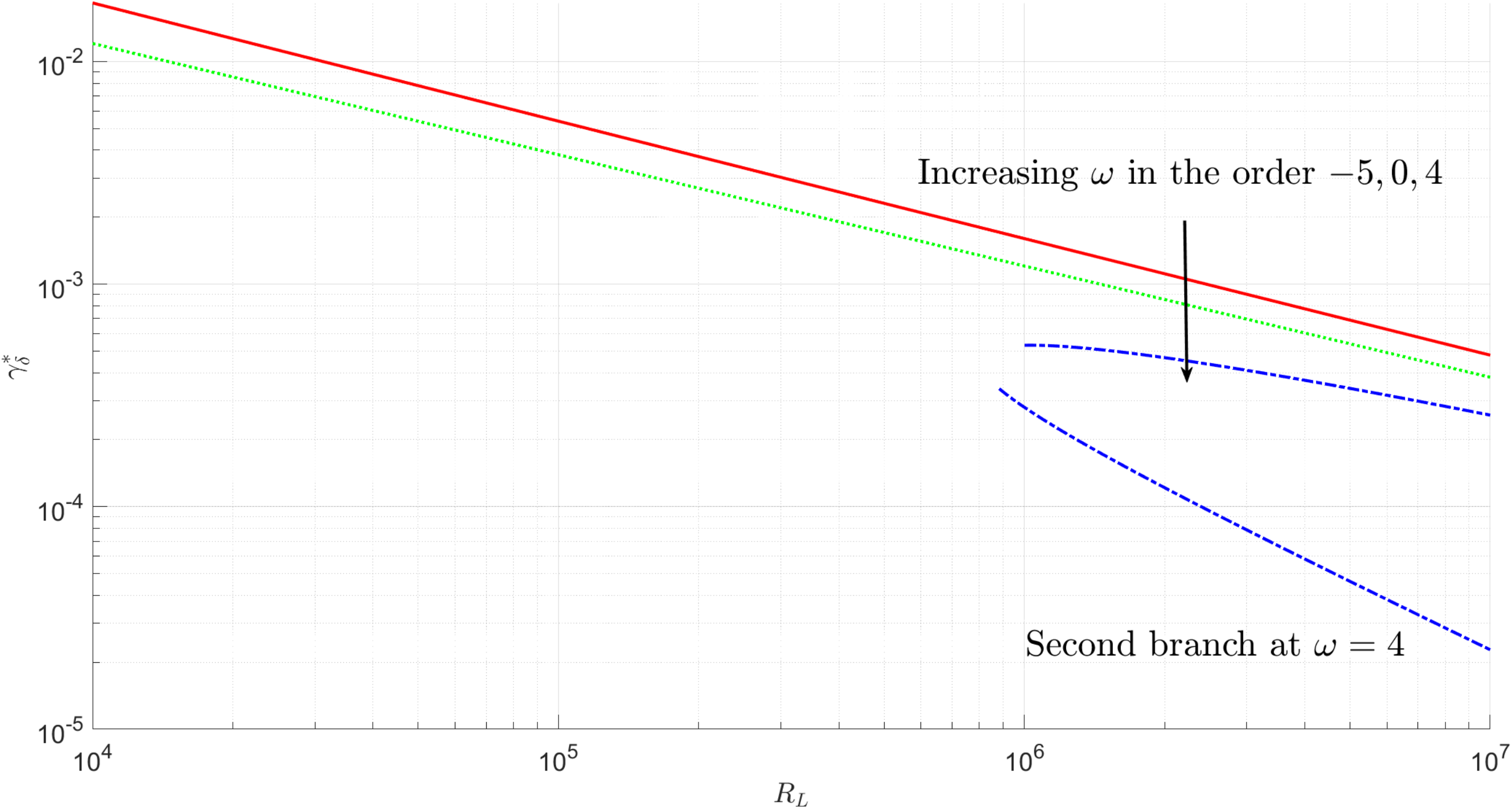


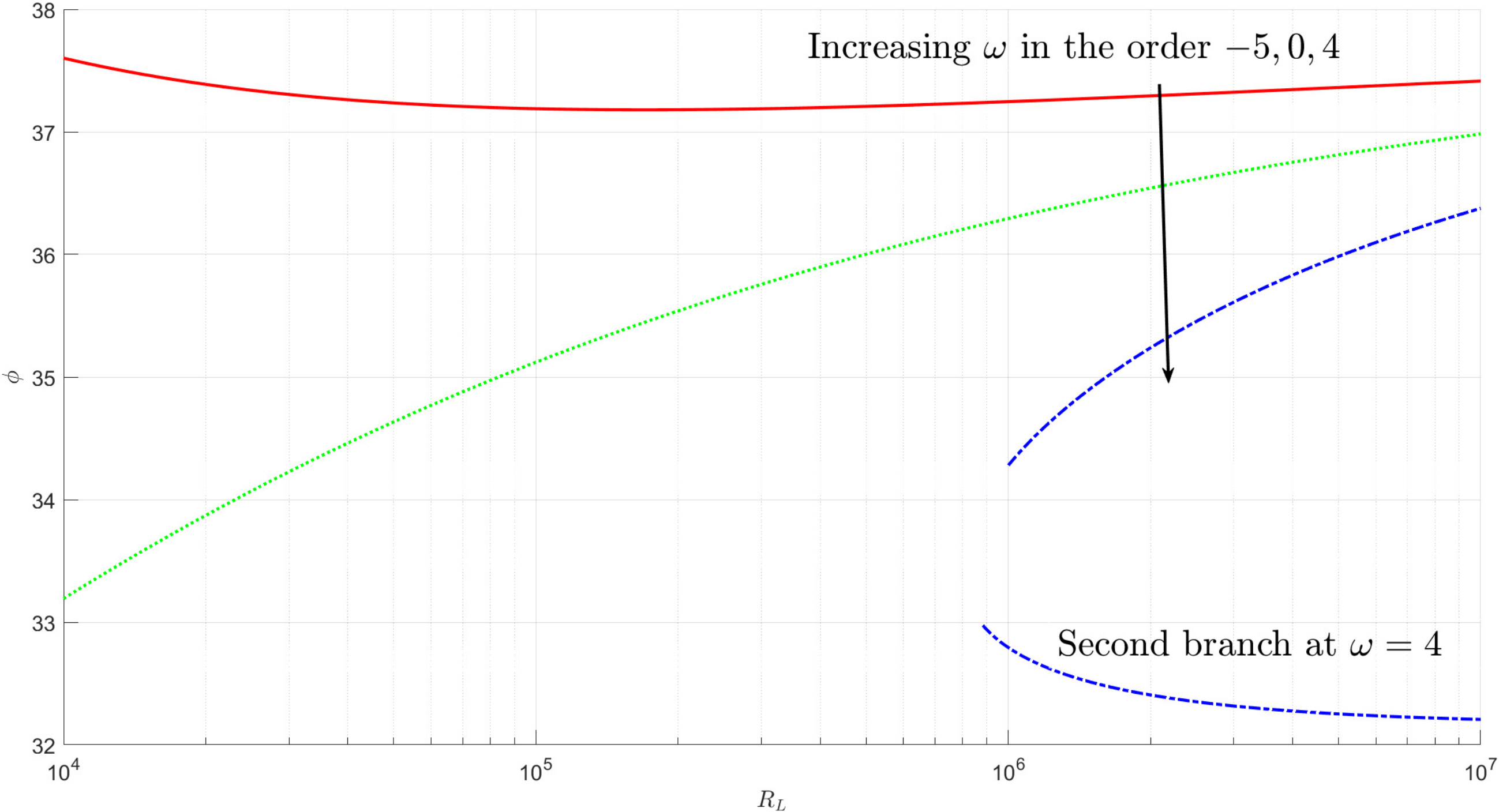


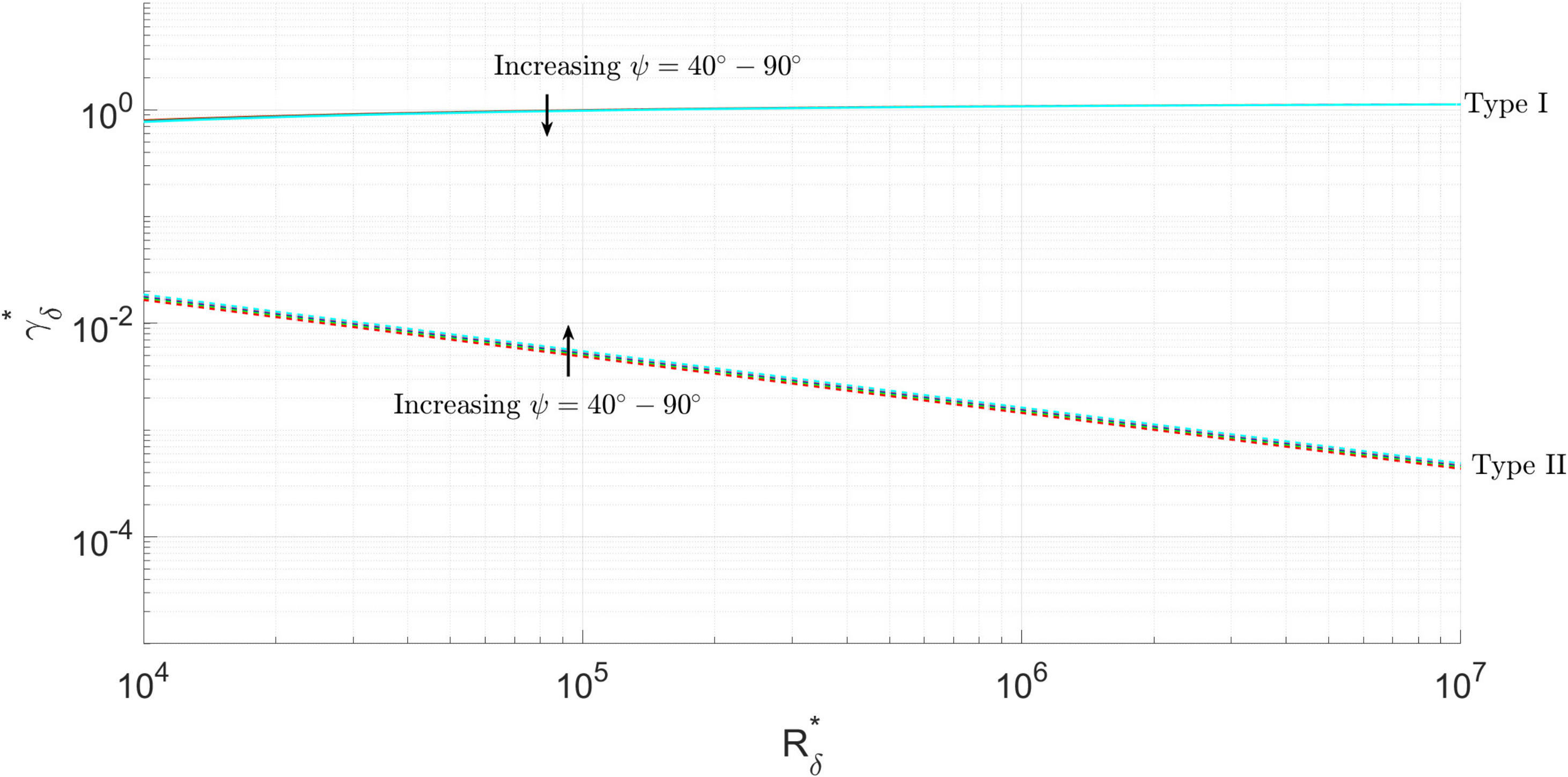


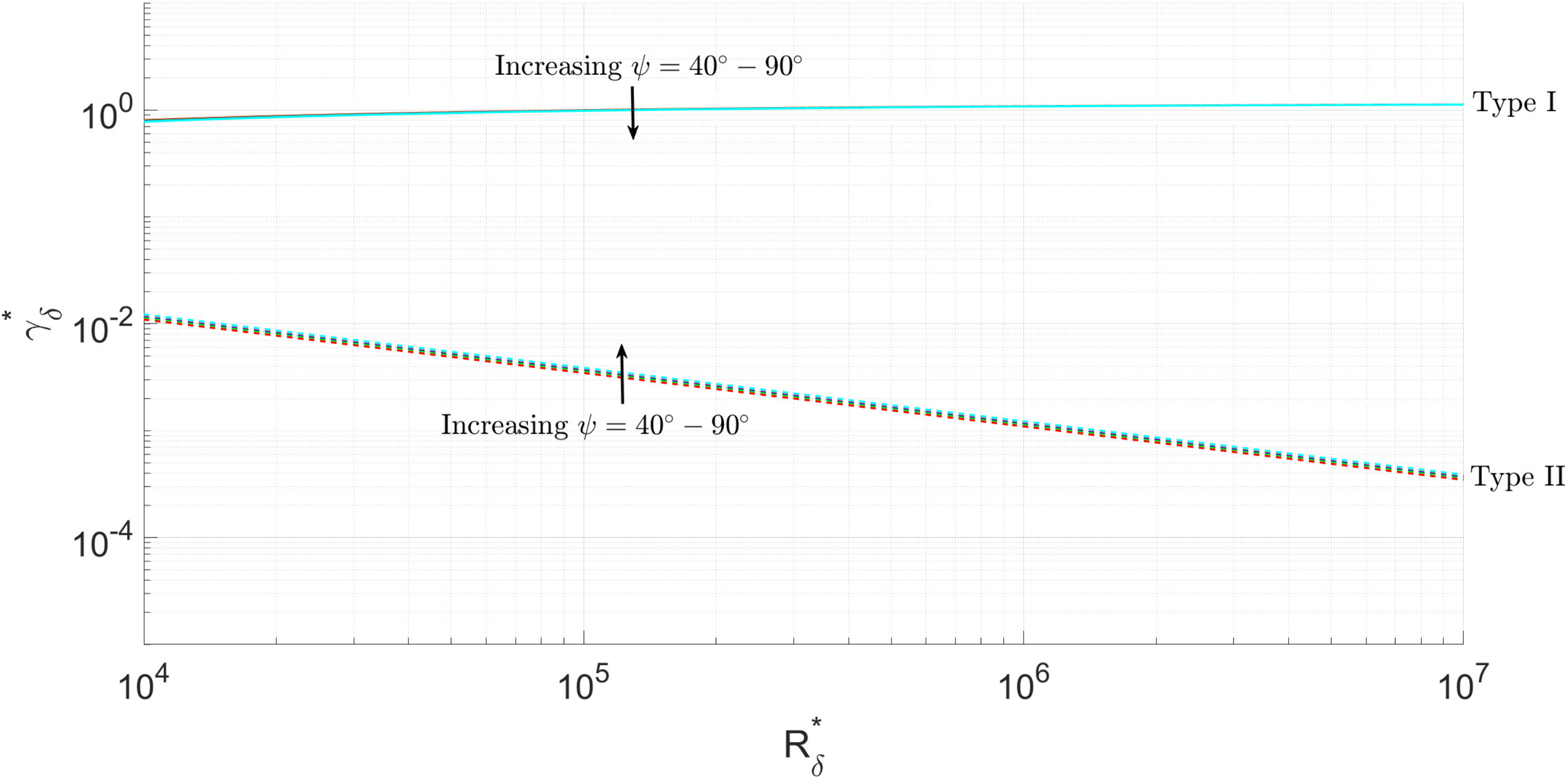


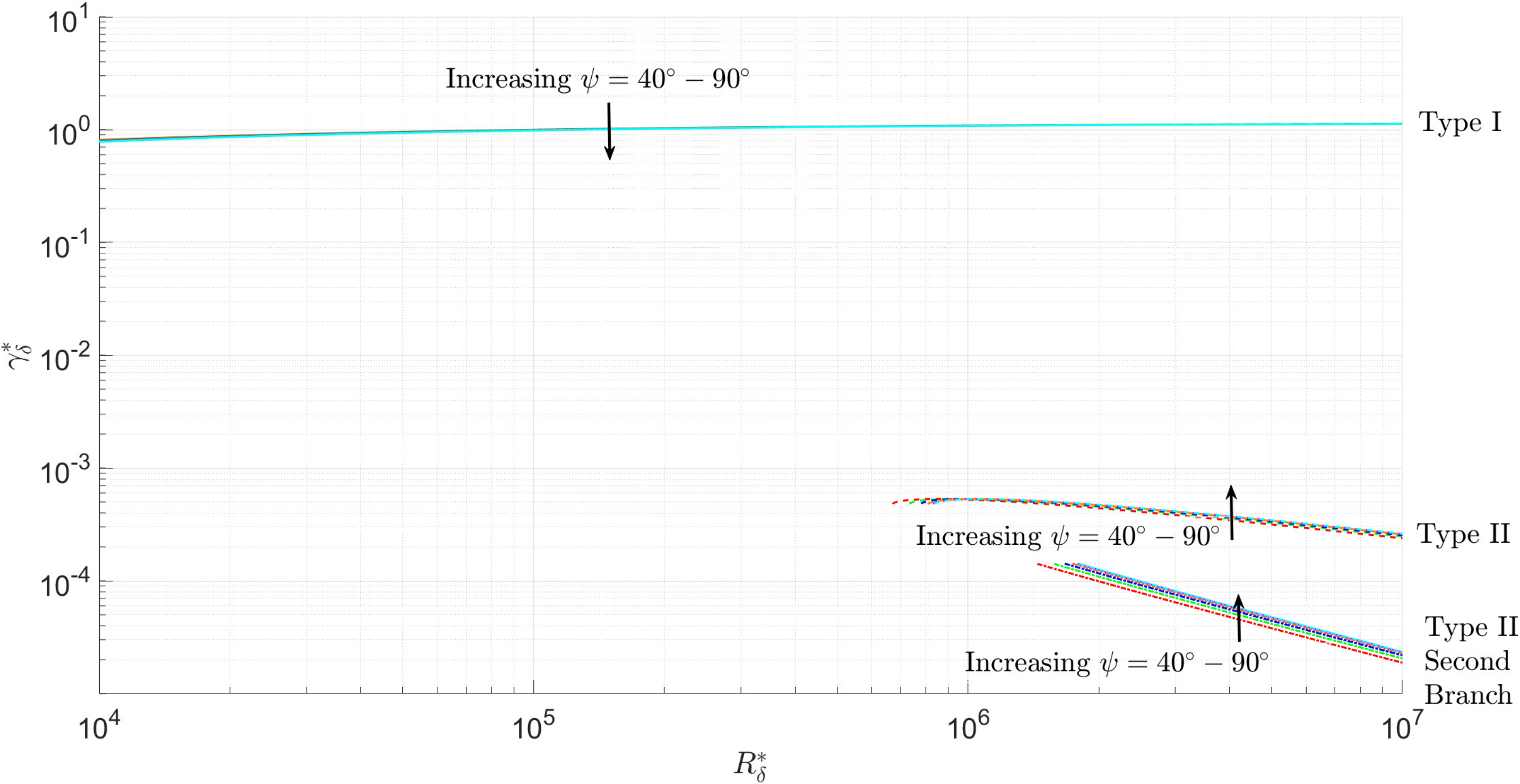


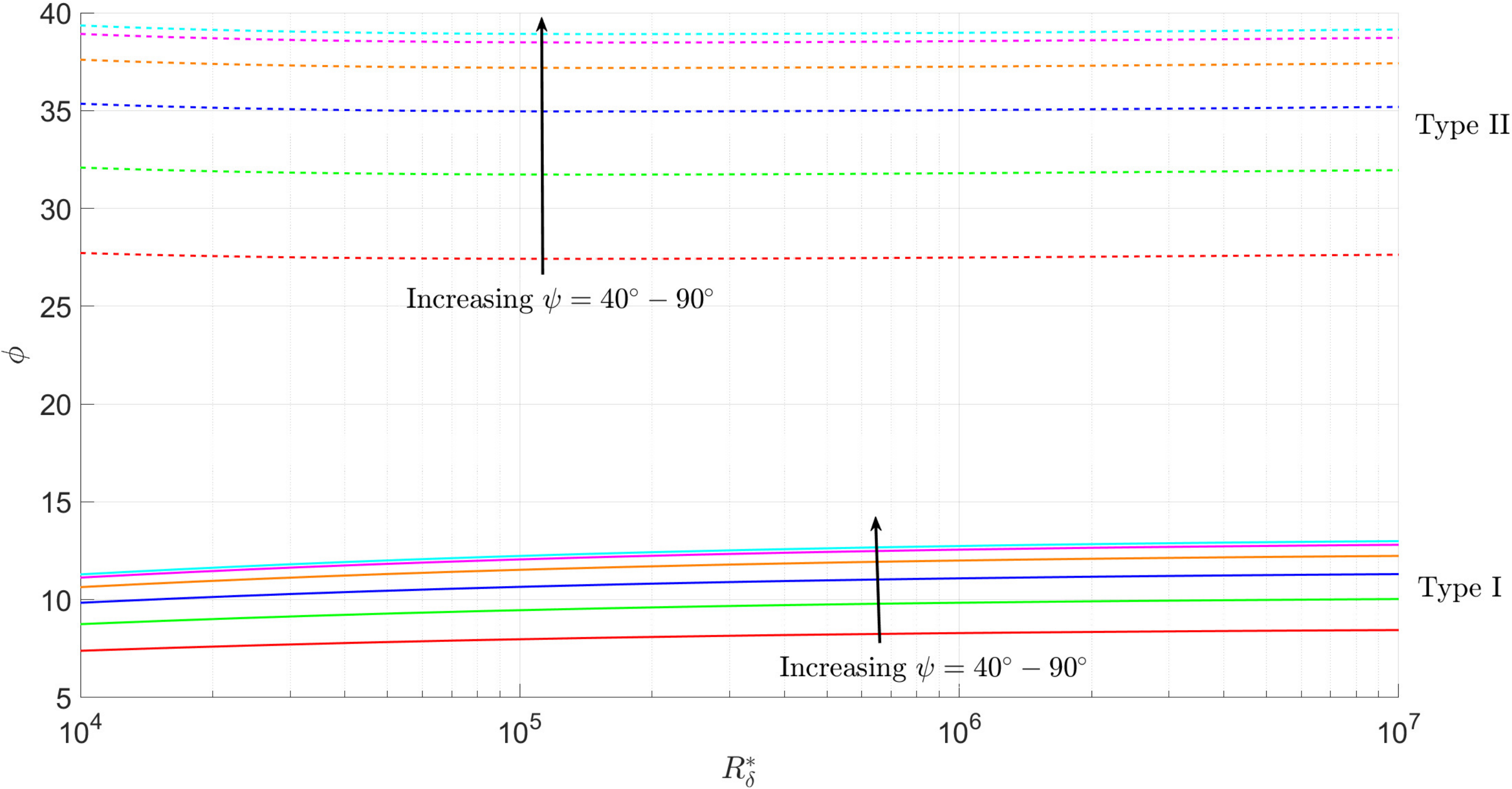


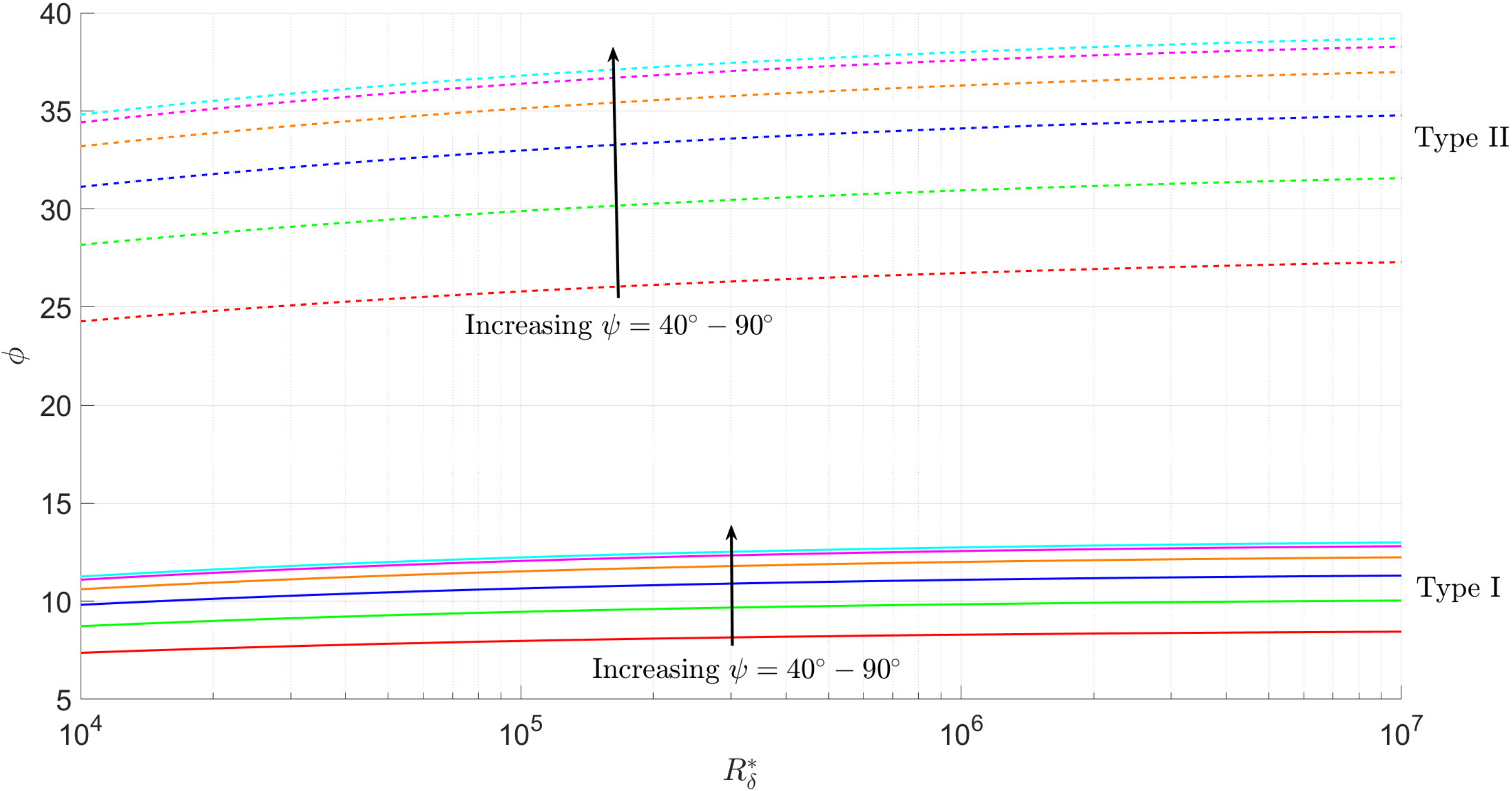


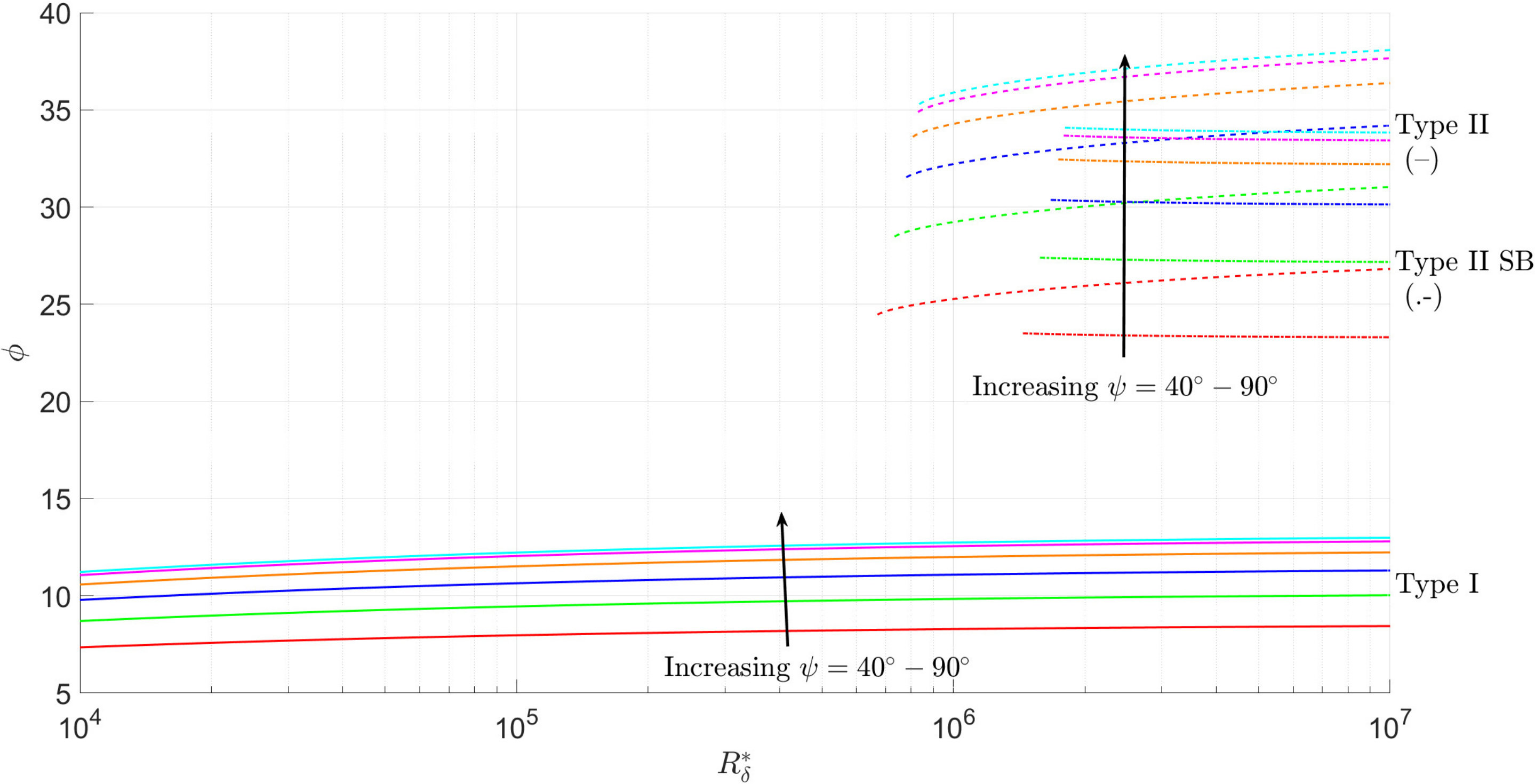


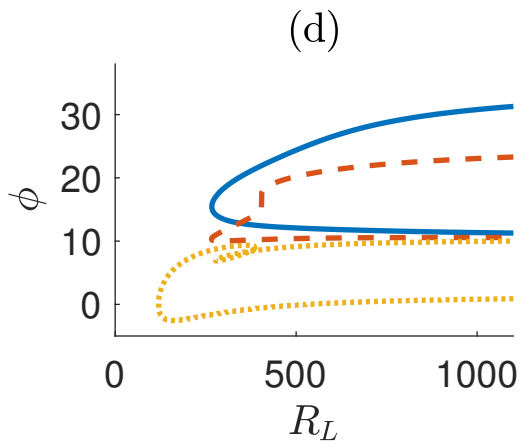
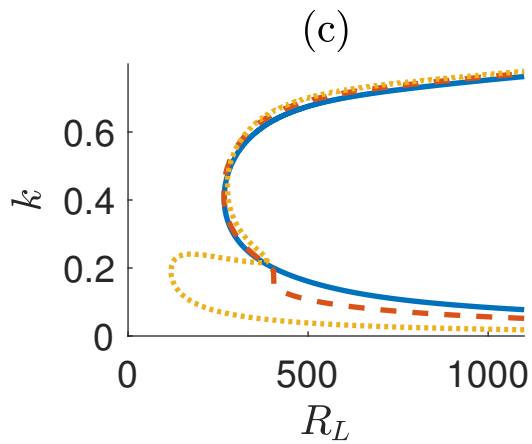
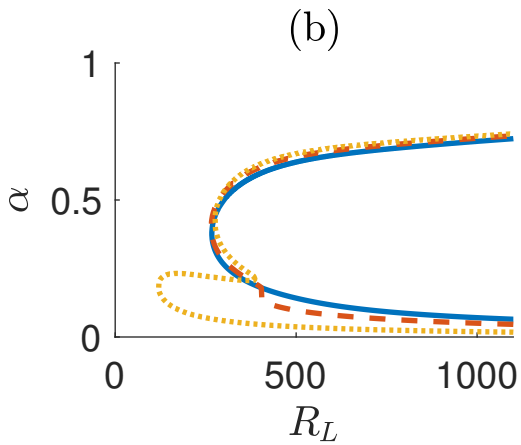
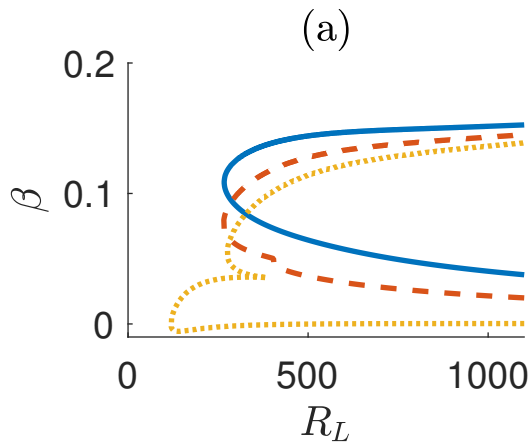


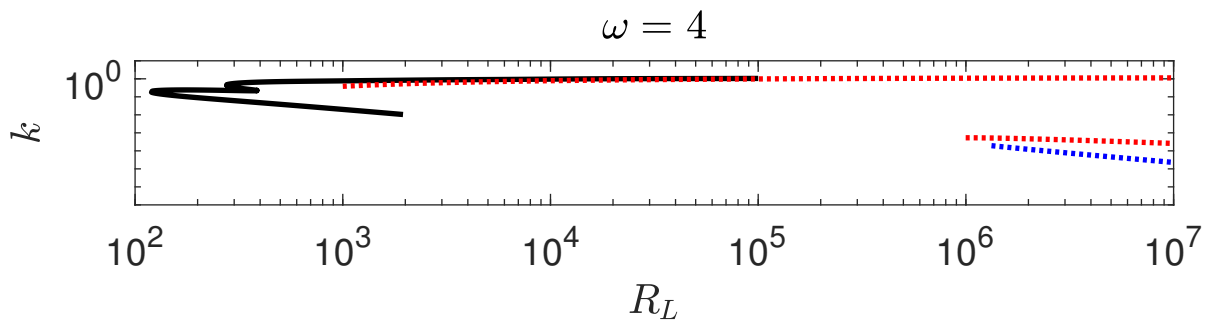
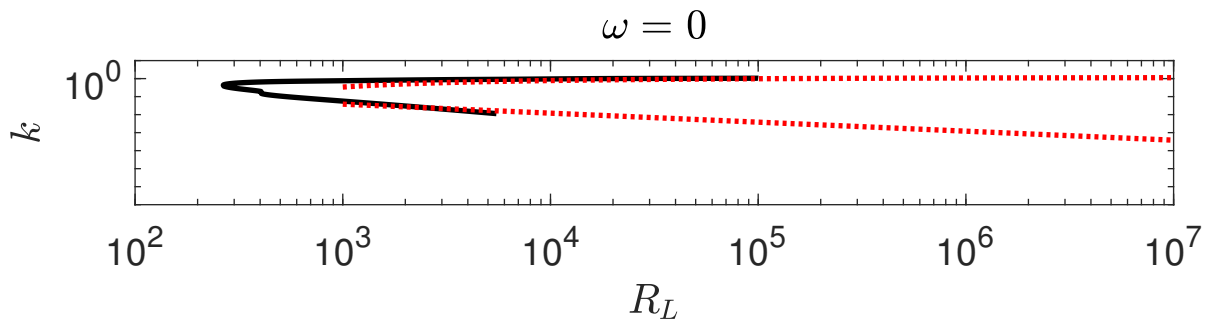
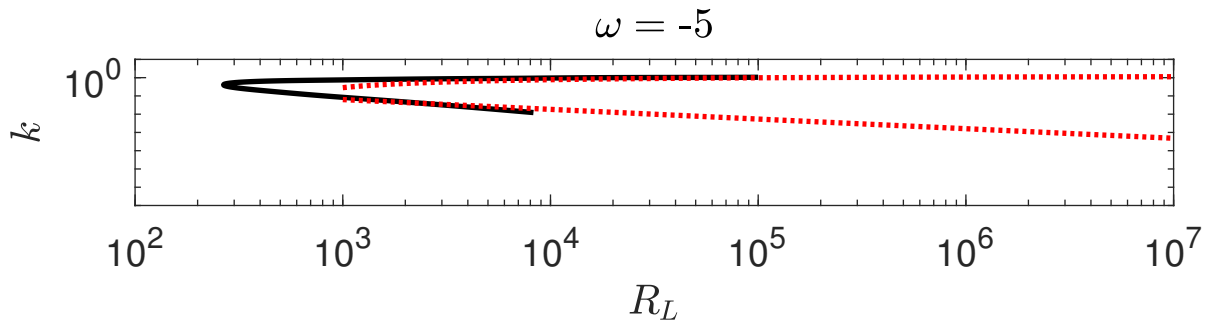




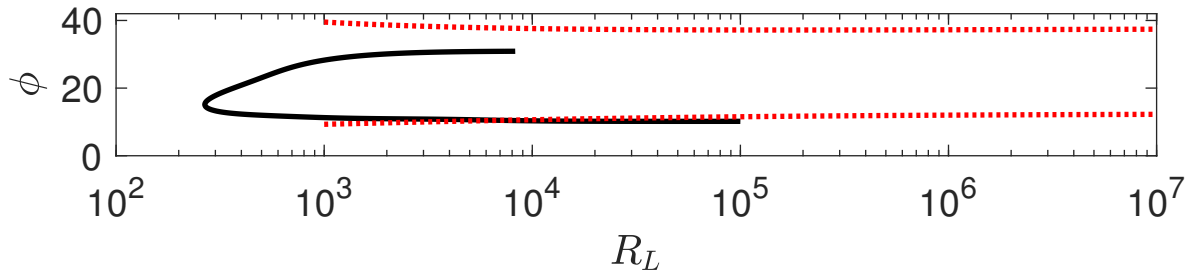




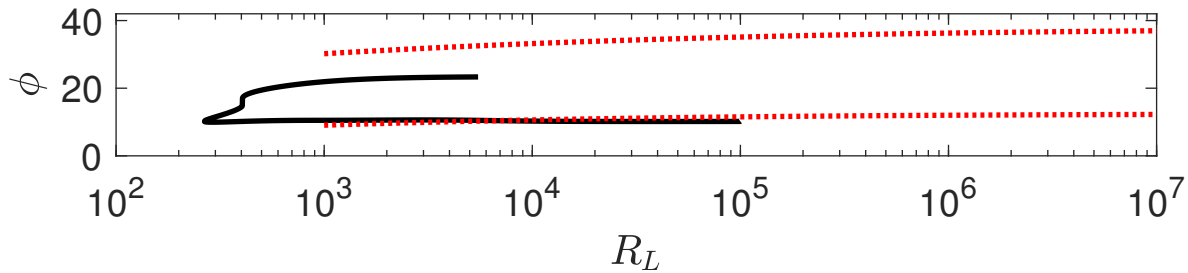




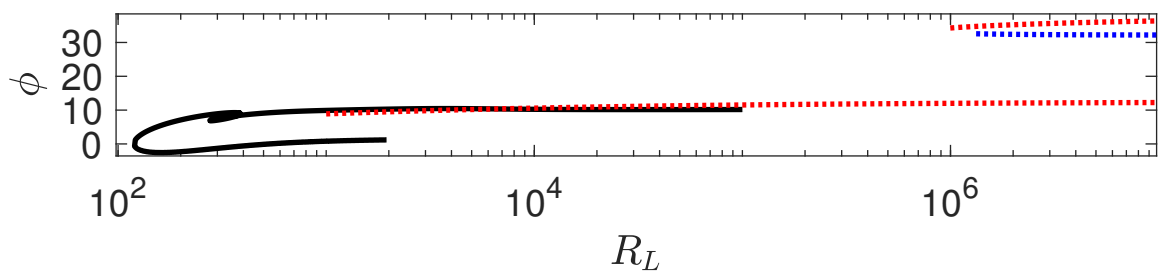
$\omega = -5$



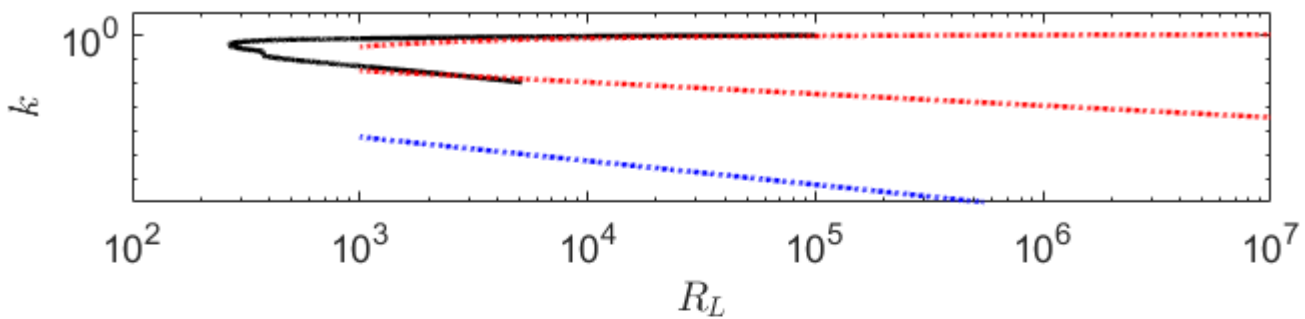
$\omega = 0$



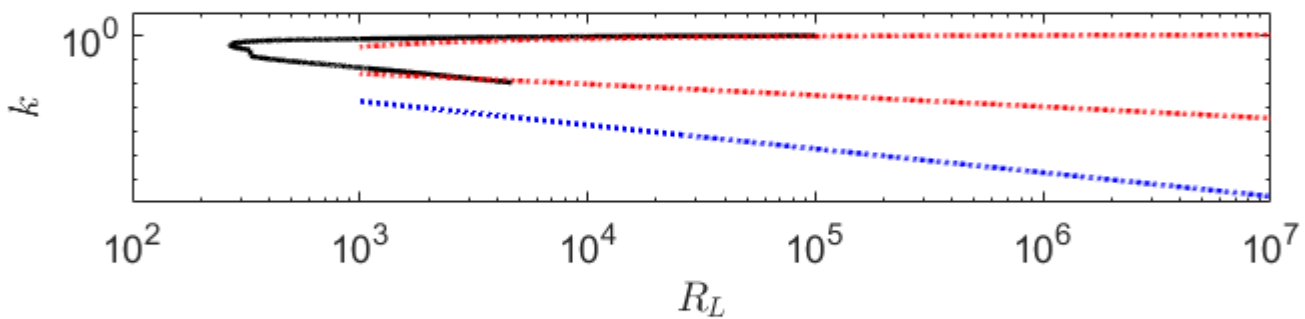
$\omega = 4$



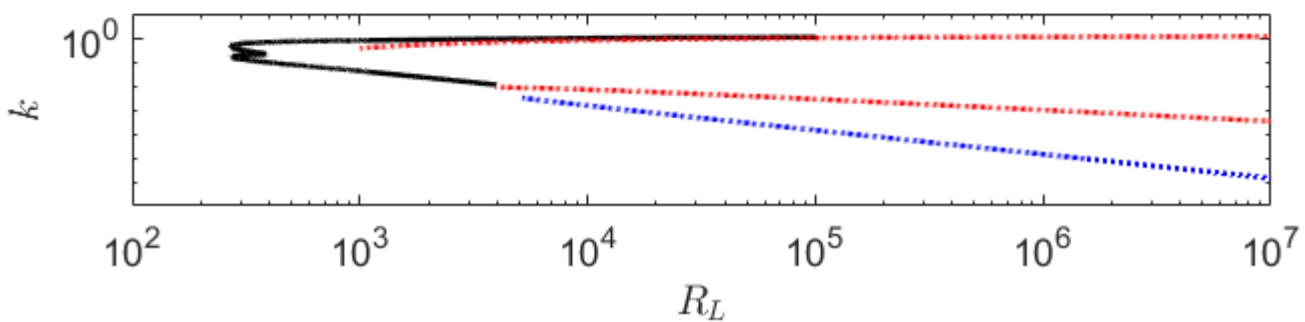
$$\omega = 0.5$$

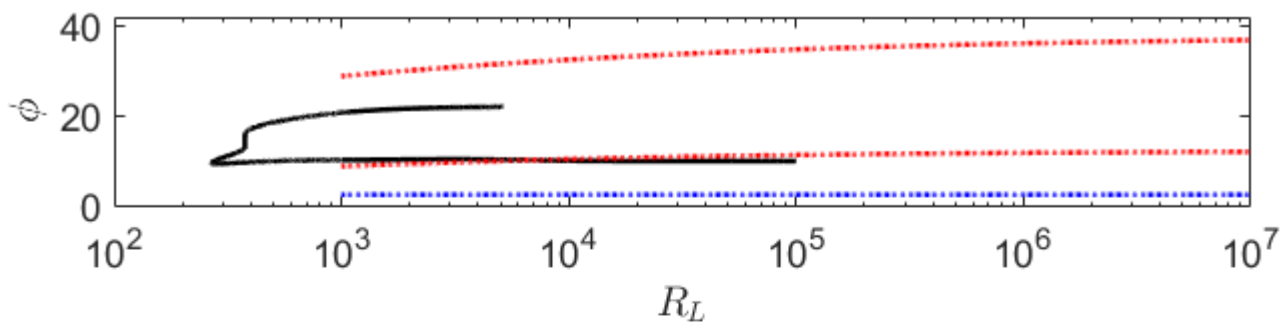
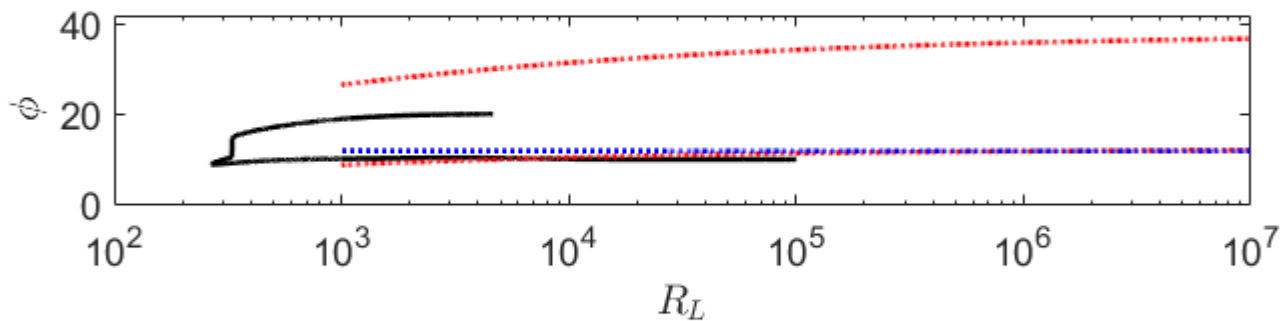
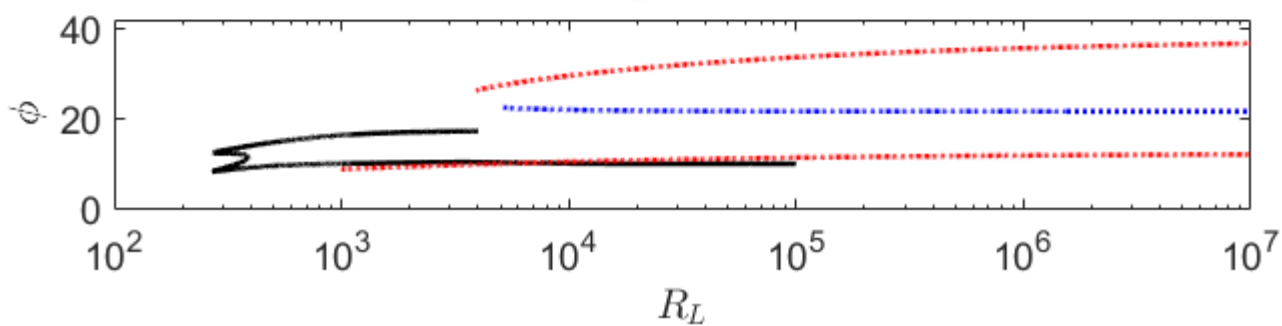


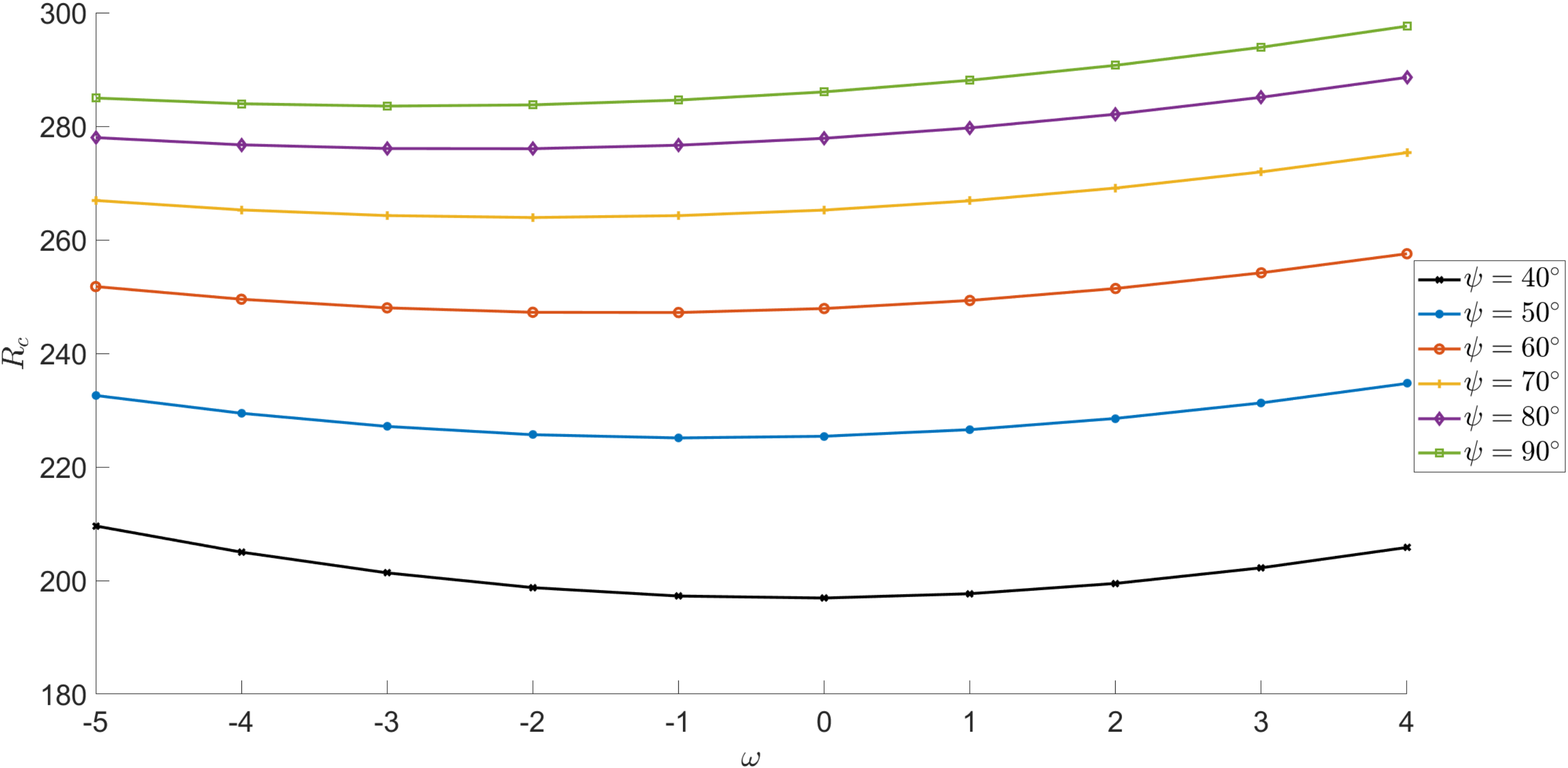
$$\omega = 1.2$$

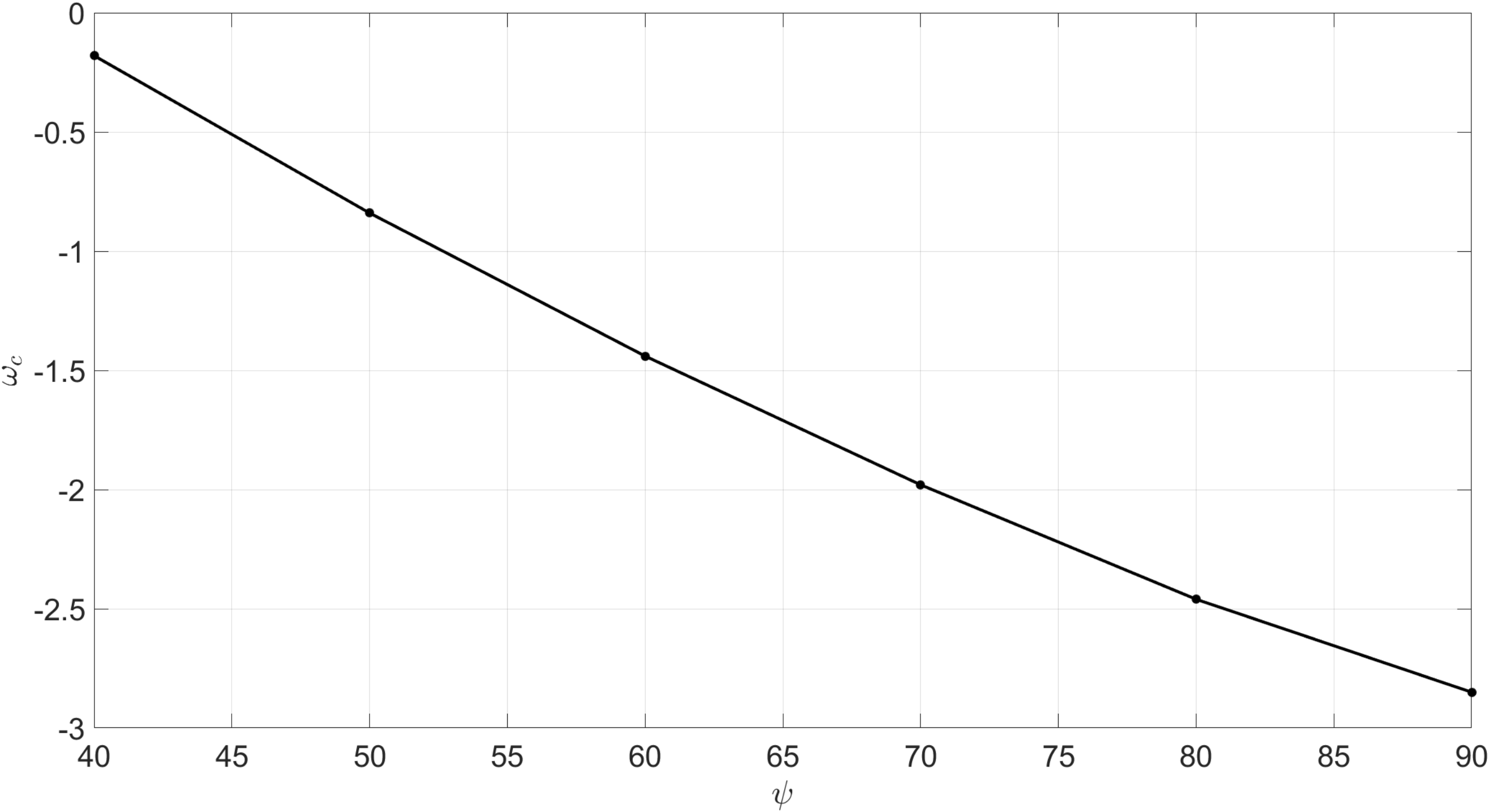


$$\omega = 2$$

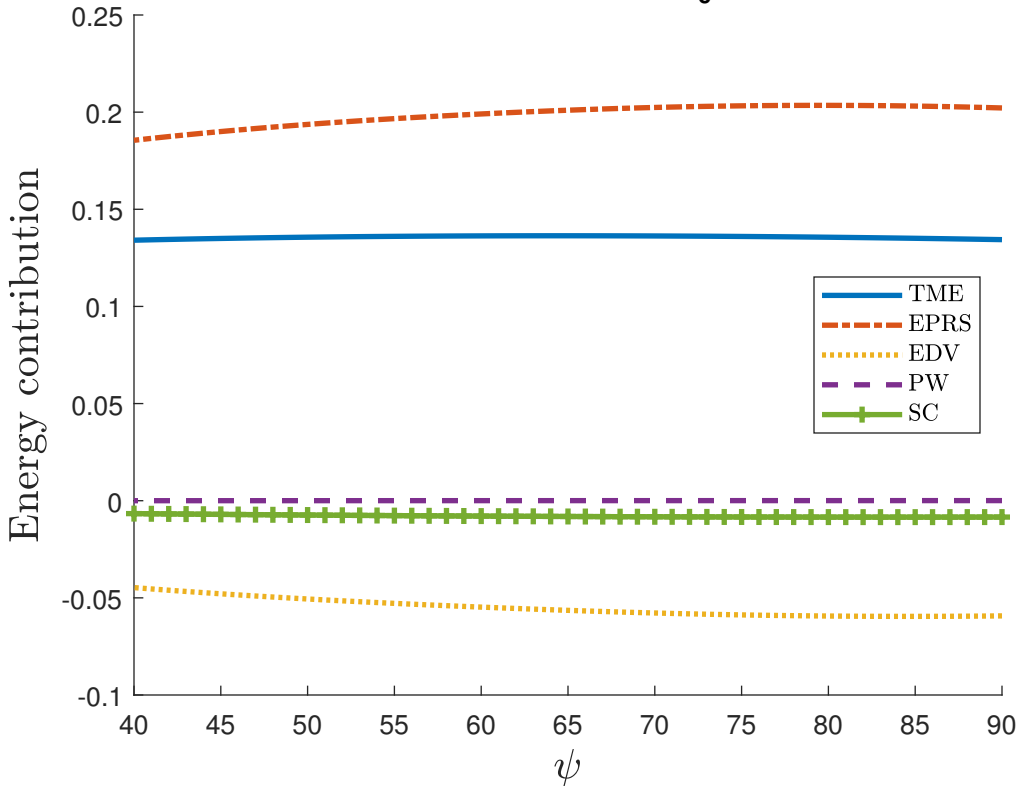


$\omega = 0.5$  $\omega = 1.2$  $\omega = 2$ 





# Energy contribution at $R_c+200$



# Energy contribution at R\_c+200

